1986

Vacuum ultraviolet photochemistry: I. Unimolecular decomposition studies of small hydrocarbon clusters by molecular beam photoionization mass spectrometry; II. Photofragment dynamics study of carbon disulfide by high resolution molecular beam laser photofragment time-of-flight mass spectrometry

Wen-Bih Tzeng
Iowa State University

INFORMATION TO USERS

This reproduction was made from a copy of a manuscript sent to us for publication and microfilming. While the most advanced technology has been used to photograph and reproduce this manuscript, the quality of the reproduction is heavily dependent upon the quality of the material submitted. Pages in any manuscript may have indistinct print. In all cases the best available copy has been filmed.

The following explanation of techniques is provided to help clarify notations which may appear on this reproduction.

1. Manuscripts may not always be complete. When it is not possible to obtain missing pages, a note appears to indicate this.

2. When copyrighted materials are removed from the manuscript, a note appears to indicate this.

3. Oversize materials (maps, drawings, and charts) are photographed by sectioning the original, beginning at the upper left hand corner and continuing from left to right in equal sections with small overlaps. Each oversize page is also filmed as one exposure and is available, for an additional charge, as a standard 35mm slide or in black and white paper format.*

4. Most photographs reproduce acceptably on positive microfilm or microfiche but lack clarity on xerographic copies made from the microfilm. For an additional charge, all photographs are available in black and white standard 35mm slide format.*

***For more information about black and white slides or enlarged paper reproductions, please contact the Dissertations Customer Services Department.**

UMI Dissertation Information Service

University Microfilms International
A Bell & Howell Information Company
300 N. Zeeb Road, Ann Arbor, Michigan 48106

Tzeng, Wen-Bih

VACUUM ULTRAVIOLET PHOTOCHEMISTRY. I. UNIMOLECULAR DECOMPOSITION STUDIES OF SMALL HYDROCARBON CLUSTERS BY MOLECULAR BEAM PHOTOIONIZATION MASS SPECTROMETRY. II. PHOTOFRAGMENT DYNAMICS STUDY OF CARBON DISULFIDE BY HIGH RESOLUTION MOLECULAR BEAM LASER PHOTOFRAGMENT TIME-OF-FLIGHT MASS SPECTROMETRY

Iowa State University PH.D. 1986

PLEASE NOTE:

In all cases this material has been filmed in the best possible way from the available copy. Problems encountered with this document have been identified here with a check mark __✓__.

1. Glossy photographs or pages _____
2. Colored illustrations, paper or print _____
3. Photographs with dark background _____
4. Illustrations are poor copy _____
5. Pages with black marks, not original copy _____
6. Print shows through as there is text on both sides of page _____
7. Indistinct, broken or small print on several pages __✓__
8. Print exceeds margin requirements _____
9. Tightly bound copy with print lost in spine _____
10. Computer printout pages with indistinct print _____
11. Page(s) _____ lacking when material received, and not available from school or author.
12. Page(s) _____ seem to be missing in numbering only as text follows.
13. Two pages numbered _____. Text follows.
14. Curling and wrinkled pages _____
15. Dissertation contains pages with print at a slant, filmed as received _____
16. Other _____

_____

_____

Vacuum ultraviolet photochemistry

I. Unimolecular decomposition studies of small hydrocarbon clusters by molecular beam photoionization mass spectrometry

II. Photofragment dynamics study of carbon disulfide by high resolution molecular beam laser photofragment time-of-flight mass spectrometry

by

Wen-Bih Tzeng

A Dissertation Submitted to the
Graduate Faculty in Partial Fulfillment of the
Requirements for the Degree of
DOCTOR OF PHILOSOPHY

Department: Chemistry
Major: Physical Chemistry

Approved:

Signature was redacted for privacy.

In Charge of Major Work

Signature was redacted for privacy.

For the Major Department

Signature was redacted for privacy.

For the Graduate College

Members of the Committee:

Signature was redacted for privacy.

Iowa State University
Ames, Iowa

1986

TABLE OF CONTENTS

ACKNOWLEDGEMENTS

I would like to express my deepest appreciation to Professor Cheuk-Yiu Ng for his consistent support and advice throughout the whole project. His enthusiastic working spirit not only has made a tremendous impact on me through my graduate career at ISU but it will influence me for the rest of my life. Without his guidance and help in various situations, this fruitful project would not have been possible. I very much appreciate his sense of letting me make decisions in most occasions and his willingness to help at all times. Professor Roland M. Marcotte of Texas A & I University, who initiated my interest in scientific instrumentation and in the general fields of chemical kinetics and dynamics, will always be remembered and appreciated.

Dr. Yoshi Ono deserves recognition for teaching me basic soldering techniques for vacuum forelines, and basic electrical wiring techniques for pumps and various instruments. His warm friendship will never be forgotten. I am also indebted to Dr. Steve Linn who patiently showed me how to operate the bulky molecular beam photoionization mass spectrometer. My special thanks go to Dr. Harry F. Prest who taught me basic vacuum technology and mechanical engineering which are essential in machine design and assembly. Many of his ideas have been very helpful and appreciated.

I am grateful to Jerry Flesch for helping me to align the apparatus, loaning me many of his instruments and sharing his 30-year expertise in instrumentation. I have personally benefited a lot by

learning from his good attitude towards colleagues and good habits in treating instruments. The help from J. D. Shao in using LSI-11/23 computer for data acquisition and analysis is valued.

The construction of this sophisticated molecular beam laser photofragment time-of-flight (MB-LP-TOF) mass spectrometer would have been impossible without the work of many skillful people in the Ames Laboratory and Chemistry Department, Iowa State University. In the Ames Lab Metals Development Machine Shop, Carl D. Westberg modified two 20" hexa-port stainless steel chambers and fabricated most major pieces of rotatable beam source chamber; Thomas L. Johnson made the molecular beam nozzle and its holder, time-of-flight chopper wheel and motor housing components, and mounting accessories for beam source chamber rotation driving gear system; Jerry Hand machined the quadrupole rods, MACRO insulator, exit lens set, and dumb bell ion target.

My sincere appreciation is also directed to wonderful and skillful friends in the Chemistry Department Machine shop: Eldon R. Ness, George W. Steiniger, and John L. Sauke. They not only made chamber stands, numerous mounting and alignment accessories, and many small important pieces but also provided quick and excellent services. With their help, I was able to expedite processes of assembly, alignment, modification and initial tests of this MB-LP-TOF apparatus.

Skillful and friendly people in the Instrumentation and Computer Services Department (John H. Erickson, Darwin R. Lekwa, Raymond C. Prior, Clare O. Tweedt, William D. Thomas, Dennis V. Jensen, John F. Holmer, Jr., and John R. Hjortshoj) deserve acknowledgement. The work

in the design and construction of the Laser Multichannel Scaler microprocessor control system by Harold D. Skank is also greatly valued.

My special thanks go to my parents for their endless support, encouragement and love through my life. Lastly, I would like to dedicate my accomplishments in graduate studies to my wife, Meichin. Her deep understanding, support, encouragement and love have been one of the very important sources of strength and driving force for me to work hard with great enthusiasm.

GENERAL INTRODUCTION

Studies of vacuum ultraviolet (VUV) photochemical processes are important for understanding the kinetic and dynamic mechnisms in plasma physics, free radical chemistry, laser-assisted chemistry, and atmospheric chemistry.[1-2] These studies have been greatly promoted due to the rapid development in the techniques of VUV light sources (e.g., synchrotron radiation, continuum VUV light source and pulsed VUV lasers) and molecular and cluster beams in recent years.[3-5]

The first part of this thesis contains the unimolecular decomposition studies of small hydrocarbon clusters using the molecular beam photoionization mass spectrometry method. By combining the use of the Hopfield continuum and the hydrogen many-line pseudocontinuum, the continuous VUV light source covers the wavelength range of 600-2000 Å (~6-21 eV). The supersonic nozzle beam technique has been adopted to produce high intensty, cooled molecules in a collisionless condition. The product ions of photoionization and fragmentation processes are detected by a quadrupole mass spectrometer.

In photoionization experiments one measures photoionization efficiency (PIE, ratio of the detected photoion intensity to the incident photon intensity) as a function of photon energy. The PIE curves provide accurate determinations of molecular ionization energies and fragment appearance energies. The results lead to a better understanding of the kinetic and dynamic mechanisms in photochemical processes.[6-15]

The second part of this thesis describes the photofragment dynamics study of carbon disulfide by high resolution molecular beam

photofragment time-of-flight (TOF) mass spectrometry. The newly constructed apparatus consists of a pulsed single frequency ArF laser (193 nm), a rotatable molecular beam generation system and a movable detection system.

In the laser photofragment TOF experiments one measure flight times of product fragments following the photofragmentation processes. The TOF data taken in the laboratory are then converted to corresponding center-of-mass (c.m.) energy for meaningful interpretations. The studies not only provide accurate measurements of molecular bond dissociation energies but also yield valuable information on the energy partitioning among product fragments in photodissociation, the lifetimes and symmetry properties of the dissociative excited states, and the potential energy surfaces.[16-22]

Explanation of Thesis Format

This thesis contains two parts whose titles are clearly identified. Each of the three sections in Part I represents an independent article in the format of a publication. Part II concerning photofragment dynamics study also has three sections. Sections I and II are the theory of energy partitioning and description of experimental apparatus, respectively, whereas section III represents an independent article in a format ready to be submitted for publication with minor modifications. The figures, tables and references cited in each section refer only to those contained in that section. The references cited in the general introduction and general summary are listed in the reference section at the end of the thesis.

PART I. UNIMOLECULAR DECOMPOSITION STUDIES OF SMALL HYDROCARBON CLUSTERS BY MOLECULAR BEAM PHOTOIONIZATION MASS SPECTROMETRY

Introduction

In principle, a unimolecular reaction which involves the isomerization or decomposition of an isolated reactant molecule through an activated complex is the simplest elementary reaction.[1,2] However, more complicated unimolecular reactions involving the formation of collision complexes are often observed in ion-molecule reactions.

Studies of unimolecular decompositions which involve the formation of collision complexes have increased in numbers since Field, Franklin and Lampe described the ion-molecule reactions of ethylene and acetylene.[3,4] The direct observation of collision complexes can lead to an interpretation that the rate of the reaction is a combination of two factors: (1) the rate of formation of the collision complexes and (2) the fraction of these complexes which decomposes to products. This implies that the collision complexes simply forget how they were formed, and fragment into products according to the available competing decomposition pathways.

Since Becker et al.[5] made the first measurements of the velocity distribution in nozzle beams to demonstrate the narrowed velocity distributions as predicted by Kantrowitz and Grey,[6] the molecular beams from nozzle sources have been widely used in molecular spectroscopy and reaction dynamics studies.[7,8] However, the production of molecular

beams and cluster beams from nozzle sources are closely related so that a supersonic molecular beam apparatus can also be used to generate cluster beams by varying the nozzle conditions.[9]

Upon photoionization these van der Waals clusters can undergo so-called "ion-molecule half-reactions."[10,11] Photoionization of these clusters provides a "clean" way for directly preparing collision complexes which fragment through ion-molecule reaction channels.[12] Observing the decomposition products of the collision complexes can give insight into the mechanisms of ion-molecule reactions, high Rydberg state chemistry, and unimolecular decompositions.[13-40]

References

1. P. J. Robinson and K. A. Holbrook, Unimolecular Reactions (John Wiley & Sons, New York, 1972).
2. W. C. Gardiner, Jr., Rates and Mechanisms of Chemical Reactions (W. A. Benjamin, Inc. Menlo Park, CA, 1972).
3. F. H. Field, J. L. Franklin, and F. W. Lampe, J. Am. Chem. Soc. 79, 2419 (1957).
4. F. H. Field, J. L. Franklin, and F. W. Lampe, J. Am. Chem. Soc. 79, 2665 (1957).
5. E. W. Becker, K. Bier and W. Henkes, Z. Phys. 146, 333 (1956).
6. A. Kantrowitz and J. Grey, Rev. Sci. Instrum. 22, 328 (1951).
7. R. E. Smally, L. Wharton and D. H. Levy, Acct. Chem. Res. 10, 139 (1977).
8. J. D. McDonal, P. R. LeBreton, Y. T. Lee and D. R. Herschback, J. Chem. Phys. 56, 769 (1972).
9. O. F. Hagena, "Cluster Beams from Noxxle Sources", in Molecular Beams and Low Density Gasdynamics, edited by P. P. Wegener (Marcel Dekker, Inc., New York, 1974).
10. C. E. Klots and R. N. Compton, J. Chem. Phys. 69, 1636 (1978).

11. C. E. Klots and R. N. Compton, J. Chem. Phys. 69, 1644 (1978).

12. C. E. Klots, "Ion-Molecular Collision Complexes", in Kinetics of Ion-Molecule Reactions, edited by P. Ausloos (Plenum, New York, 1979).

13. S. L. Anderson, T. Hirooka, P. W. Tiedemann, B. H. Mahan and Y. T. Lee, J. Chem. Phys. 73, 4779 (1980).

14. S. H. Linn, Y. Ono, C. Y. Ng, J. Chem. Phys. 74, 3342 (1981).

15. S. H. Linn, Y. Ono, C. Y. Ng, J. Chem. Phys. 74, 3348 (1981).

16. G. G. Jones and J. W. Taylor, J. Chem. Phys. 68, 1768 (1978).

17. W. M. Trott, N. C. Blais and E. A. Walters, J. Chem. Phys. 71, 1692 (1979).

18. C. Y. Trevor, P. W. Tiedemann, S. T. Ceyer, P. L. Kronebush, B. H. Mahan and Y. T. Lee, J. Chem. Phys. 67, 4235 (1977).

19. E. A. Walters and N. C. Blais, J. Chem. Phys. 75, 4208 (1981).

20. S. T. Ceyer, P. W. Tiedemann, C. Y. Ng, B. H. Mahn and Y. T. Lee, J. Chem. Phys. 70, 2138 (1979).

21. S. T. Ceyer, P. W. Tiedemann, B. H. Mahan and Y. T. Lee, J. Chem. Phys. 70, 14 (1979).

22. C. Y. Ng, D. J. Trevor, B. H. Mahan and Y. T. Lee, J. Chem. Phys. 66, 3985 (1977).

23. P. M. Dehmer and E. D. Poliakoff, Chem. Phys. Lett. 77, 326 (1981).

24. P. M. Dehmer and S. T. Pratt, J. Chem. Phys. 76, 843 (1982).

25. P. M. Dehmer, J. Chem. Phys. 76, 1263 (1982).

26. C. Y. Ng, P. W. Tiedemann, B. H. Mahan and Y. T. Lee, J. Chem. Phys. 66, 5737 (1977).

27. S. T. Pratt and P. M. Dehmer, J. Chem. Phys. 76, 3433 (1982).

28. W. M. Trott, N. C. Blais and E. A. Walters, J. Chem. Phys. 69, 3150 (1978).

29. Y. Ono, S. H. Linn, H. F. Prest, M. E. Gress and C. Y. Ng, J. Chem. Phys. 73, 2523 (1980).

30. Y. Ono, S. H. Linn, H. F. Prest, M. E. Gress and C. Y. Ng, J. Chem. Phys. 74, 1125 (1981).

31. Y. Ono, E. A. Osuch and C. Y. Ng, J. Chem. Phys. 74, 1645 (1981).

32. J. Erickson and C. Y. Ng, J. Chem. Phys. 75, 1650 (1981).

33. S. H. Linn and C. Y. Ng, J. Chem. Phys. 75, 4921 (1981).

34. Y. Ono and C. Y. Ng, J. Chem. Phys. 77, 2947 (1982).

35. Y. Ono and C. Y. Ng, J. Am. Chem. Soc. 104, 4752 (1982).

36. C. Y. Ng, Adv. Chem. Phys. 52, 263 (1983).

37. Y. Ono, S. H. Linn, W.-B Tzeng and C. Y. Ng, J. Chem. Phys. 80, 1482 (1984).

38. W. -B. Tzeng, Y. Ono, S. H. Linn and C. Y. Ng, J. Chem. Phys. 83, 2803 (1985).

39. W. -B. Tzeng, Y. Ono, S. H. Linn and C. Y. Ng, J. Chem. Phys. 83, 2813 (1985).

40. P. M. Dehmer, J. Chem. Phys. 83, 24 (1985).

SECTION I. A STUDY OF THE UNIMOLECULAR DECOMPOSITION OF THE $(C_2H_4)_2^+$ COMPLEX

Abstract

The energetics of the unimolecular reactions $C_2H_4^+ \cdot C_2H_4 \longrightarrow C_3H_5^+ + CH_3$ and $C_4H_7^+ + H$ have been reinvestigated by the molecular beam photoionization method. At nozzle expansion conditions where the concentrations of $(C_2H_4)_3$ and heavier clusters produced in the beam are high, the appearance energies (AE) for $C_3H_5^+$ and $C_4H_7^+$ were found to shift to energies lower than the expected thermochemical thresholds for the formation of $C_3H_5^+$ and $C_4H_7^+$ from ethylene dimers. This indicates that ethylene trimers and heavier clusters can give rise to the same product ions as ethylene dimers. The AE's for $C_3H_5^+$ and $C_4H_7^+$ from $(C_2H_4)_2$ measured in an ethylene beam, which mainly consists of C_2H_4 and $(C_2H_4)_2$, are 10.21±0.04 eV (1214±5 Å) and 10.05±0.04 eV (1234±5 Å), respectively. Taking into account the error estimates of the thermochemical thresholds for the formation of $C_3H_5^+$ and $C_4H_7^+$ from $(C_2H_4)_2$, the latter values are in accordance with the conclusion of previous studies that the barriers for the reverse reactions of the ion-molecule reactions $C_2H_4^+ + C_2H_4$ are negligible. From the observed ionization energies of $(C_2H_4)_2$ (9.84±0.04 eV) and C_2H_4 (10.505±0.004 eV) and the estimated binding energy of $(C_2H_4)_2$ (0.02 eV), the bond dissociation energy for $C_2H_4^+ \cdot C_2H_4$ is calculated to be 15.8±1 kcal/mol.

Introduction

The ion-molecule reactions of $C_2H_4^+ \cdot C_2H_4$ have been studied extensively in the past.[1-30] The major product ions observed for these reactions are $C_3H_5^+$ and $C_4H_7^+$. The results of previous investigations support the conclusion that the reactions proceed through long-lived complexes $[C_4H_8^+]^*$, i.e.,

$$C_2H_4^+ + C_2H_4 \rightleftharpoons [C_4H_8^+]^* \longrightarrow C_3H_5^+ + CH_3, \quad (1)$$

$$\longrightarrow C_4H_7^+ + H. \quad (2)$$

The lifetime of the $[C_4H_8^+]^*$ complex was estimated to be $\sim 2.9 \times 10^{-7}$ sec.[8] Thus it can be readily stabilized by collisions in the gas cell. The study of the reactions $C_2H_4^+$ with C_2D_4 in the energy range from thermal to a few eV by Tiernan and Futrell[1] shows that the $C_2D_4^+$ ions resulted from charge transfer consisting of ~ 30% of the product ions. It has been pointed out[31] that the loosely bound collision complex $C_2H_4^+ \cdot C_2H_4$ may be the precursor of the $[C_4H_8^+]^*$ complex. Ceyer et al.[32] have performed a photoionization study of $(C_2H_4)_2$ and obtained a value of 18.2±0.5 kcal/mol for the dissociation energy of $C_2H_4^+ \cdot C_2H_4$ from the measured ionization energy (IE) of $(C_2H_4)_2$. In a recent theoretical study using the transition state switching model by Chesnavich et al.,[33] it was shown that for thermal energy ethylene ion-molecule reaction, 36% of all collision pairs which reach the shallow $(C_2H_4)_2^+$ well will back dissociate to $C_2H_4^+ + C_2H_4$ rather than proceed to the deep $C_4H_8^+$ well. They suggested that the

relatively large probability for charge transfer is due to collision pairs which back dissociate from the loosely bound collision complex.

Ceyer et al.[32] have also measured the appearance energies (AE) of $C_3H_5^+$ and $C_4H_7^+$. They found that the AE for $C_4H_7^+$ was in agreement with the accepted thermochemical threshold for reaction (2), whereas the AE for $C_3H_5^+$ was approximately 7.7 kcal/mol greater than the accepted thermodynamical threshold. This value was interpreted to be the magnitude of a barrier in the exit channel for the formation of $C_3H_5^+$. As pointed out by Chesnavich et al.,[33] this interpretation is in conflict with AE's for $C_3H_5^+$ obtained from electron impact[34] and photoionization[35] of various C_4H_8 neutral isomers and the translational energy distribution for $C_3H_5^+$ measured by Kemper and Bowers.[36]

Recently, in a photoionization study of $(C_2H_2)_2$ and $(C_2H_2)_3$, Ono and Ng[37,38] found that the AE for the formation of $C_4H_4^+$ from $(C_2H_2)_3$ is lower than the IE of $(C_2H_2)_2$. Since both $C_4H_4^+$ and $(C_2H_2)_2^+$ have the same mass, they showed that the IE of $(C_2H_2)_2$ must be measured in an acetylene beam, which has negligible intensities of acetylene trimers and heavier clusters. In the previous photoionization experiment of Ceyer et al.[32] the ratio of the intensities for $(C_2H_4)_3^+$ and $(C_2H_4)_2^+$ was approximately 0.34, indicating that the beam consisted of substantial intensities of ethylene trimer and heavier clusters. A study of the unimolecular decomposition of $(C_2H_2)_3$ supports the interpretation that the $(C_2H_2)_3^+$ ions rearrange to some common precursor ions, as do other stable $C_6H_6^+$ isomers prior to dissociation.[37] If some $(C_2H_4)_3^+$ ions formed by photoionization of $(C_2H_4)_3$ also rearrange to

stable $C_6H_{12}^+$ precursors before fragmenting, one would anticipate $C_4H_8^+$ and $C_4H_7^+$ to be possible fragment ions from $(C_2H_3)_3^+$.

$$(C_2H_4)_3 \xrightarrow{h\nu} (C_2H_4)_3^+ + e^- \longrightarrow [C_6H_{12}^+]^* + e^-$$

$$\longrightarrow C_4H_8^+ + C_2H_4 + e^-, \qquad (3)$$

$$\longrightarrow C_4H_7^+ + C_2H_5 + e^-. \qquad (4)$$

This speculation is based on the fact that both $C_4H_8^+$ and $C_4H_7^+$ were observed to be major product ions from the reactions of propylene ion with propylene, which are believed to proceed via long-lived collisional complexes $[C_6H_{12}^+]^*$.[2,39-43] Stemming from the consideration that the thermochemcial thresholds for reactions (3) and (4) are lower than the corresponding thresholds from $(C_2H_4)_2$, the values for the AE's for $C_4H_7^+$ from $(C_2H_4)_2$ and the IE of $(C_2H_4)_2$ reported previously might have been influenced by reactions (3) and (4).

In this report we present an analysis and the result of a reinvestigation on the unimolecular decomposition of $(C_2H_4)_2^+$ prepared by photoionization of $(C_2H_4)_2$ in supersonic ethylene beams.

$$(C_2H_4)_2 \xrightarrow{h\nu} (C_2H_4)_2^+ + e^- \longrightarrow [C_4H_8^+]^* + e^-$$

$$\longrightarrow C_3H_5^+ + CH_3 + e^-, \qquad (5)$$

$$\longrightarrow C_4H_7^+ + H + e^-. \qquad (6)$$

The measurements were made in nozzle expansion conditions which have minimized the formation of ethylene trimers and heavier clusters. The photoionization efficiency (PIE) curve for $C_2H_4^+$ near the threshold, obtained with a higher wavelength resolution, is also examined here.

Experimental

The experimental arrangement and procedures were essentially the same as those described previously.[44,45] Briefly, the apparatus consists of a 3-meter near-normal incidence vacuum ultraviolet (VUV) monochromator (McPherson 2253 M), a supersonic molecular beam production system, a capillary discharge lamp, a VUV light detector, and a quadrupole mass spectrometer for ion detection. The gratings employed in this study are Bausch and Lomb 1200 lines/mm MgF2 or Os coated aluminum gratings blazed at 1360 Å. Either the hydrogen many-lined pseudocontinuum, the argon continuum, or the helium Hopfield continuum was used as the light source, depending on the wavelength region to be studied.

The ethylene was obtained from Matheson with a quoted purity of $\geq$ 99.5 mole %. The C_2H_4 molecular beam was produced by supersonic expansion through a variable-temperature nozzle having a diameter of 120 μm. Most of the data for ethylene dimers were obtained at a nozzle temperature (T_0) of ~ 210 K and a stagnation pressure (P_0) of 480 Torr. In a typical experiment, the fluctuation in the nozzle temperature was less than $\pm$3 K as monitored with thermocouples. Some of the data were obtained at room temperature (T_0 ~ 298 K) and P_0 ~ 1000 Torr. Under

these expansion conditions, ions containing more than four carbon atoms were found to be negligible, indicating that C_2H_4 and $(C_2H_4)_2$ were the major constituents of the molecular beam. Since the ethylene beam was sampled in a collisionless environment, the observed fragment ions represent the primary fragments of $C_2H_4^+$ and $(C_2H_4)_2^+$. The PIE data for $C_2H_4^+$ were obtained at T_0 ~ 298 K and P_0 ~ 500 Torr.

With the exception of the high resolution PIE spectrum for $C_2H_4^+$ near the ionization threshold, which was measured using a wavelength resolution of 0.14 Å (FWHM), all the other PIE spectra were obtained with a wavelength resolution of 1.4 Å (FWHM). Data points were taken at 0.05 Å intervals for the high resolution experiment and at either 0.5 or 1 Å intervals for the low solution study. The standard deviations of the PIE data presented here are better than 10%. Each PIE spectrum was based on at least two scans, and prominent structures in the plotted data were found to be reproducible. Wavelength calibrations were achieved by using known atomic resonance lines or H_2 emission lines[46] when the H_2 pseudocontinuum was used.

Results and Discussion

The PIE spectrum for $C_2H_4^+$ near the threshold (1160-1185 Å) obtained using a wavelength resolution of 1.4 Å (FWHM) is shown in Fig. 1(a). Three steps are clearly resolved at 1163.0, 1174.5, and 1180.5 Å, an observation in good agreement with previous studies.[47-50] The second and the third steps have been assigned to the thresholds for the excitations of two quanta of the twisting vibrational mode (ν_4)

Figure 1. PIE curves for $C_2H_4^+$ in the region of 1160–1185 Å.

(a) PIE curve for $C_2H_4^+$ in the region of 1160–1185 Å obtained using the hydrogen many-lined pseudocontinuum as the light source [wavelength resolution = 1.4 Å (FWHM), P_o ~ 500 Torr, T_o ~ 298 K].

(b) PIE curve for $C_2H_4^+$ in the region of 1161–1182 Å obtained using the argon continuum as the light source [wavelength resolution = 0.14 Å (FWHM), P_o ~ 500 Torr, T_o ~ 298 K].

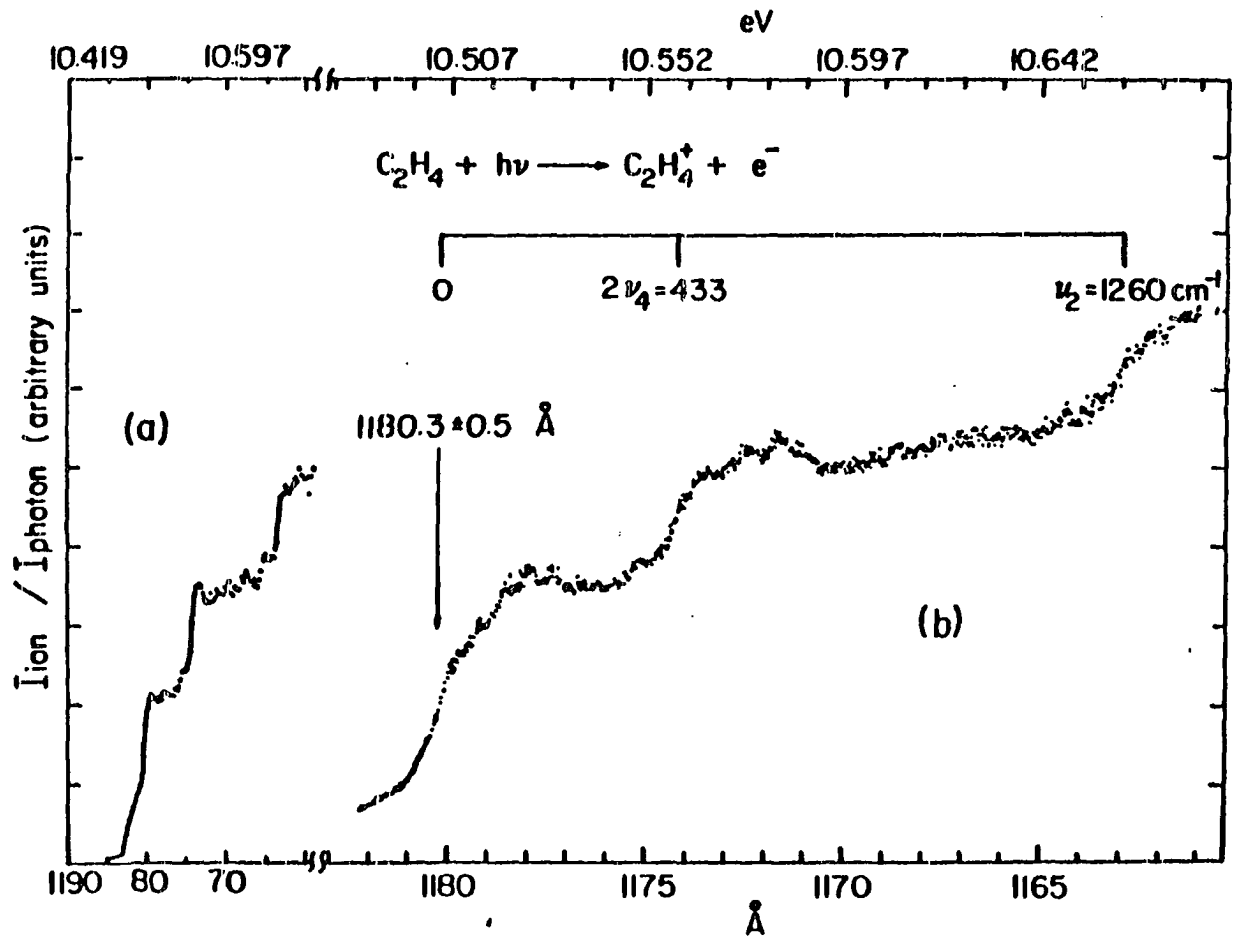
eV
10.419
10.597
10.507
10.552
10.597
10.642
$C_2H_4 + h\nu \longrightarrow C_2H_4^+ + e^-$
0
$2\nu_4 = 433$
$\nu_2 = 1260\ cm^{-1}$
(a)
1180.3 ± 0.5 Å
(b)
I_{ion} / I_{photon} (arbitrary units)
1190
80
70
1180
1175
1170
1165
Å

and one quantum of the totally symmetric C-C stretching vibrational mode (ν_2) of $C_2H_4^+$ ($\tilde{X}^2B_{3u}$), respectively.[47,48] The first step, which corresponds to the ionization threshold of C_2H_4, is found to decrease rapidly from 1180 to 1181 Å. In the region 1181-1183 Å, a small hump is discernable. Similar structure can also be found at the second and third steps. Because of the efficient rotational relaxation in a supersonic expansion, the rotational temperature of C_2H_4 is expected to be low. Furthermore, rotational excitations of C_2H_4 are expected to give rise to a nearly exponential tailing structure below the threshold. Therefore, the hump observed here cannot be completely due to rotational hot band effects. Since all the vibrational modes of C_2H_4 have vibrational frequencies greater than 810 cm^{-1} (Ref. 51) according to a Boltzmann distribution, vibrationally excited C_2H_4 should constitute less than 4% of C_2H_4 in this experiment. Stemming from the consideration that the energy span of the hump (~ 145 cm^{-1}) is substantially less than the vibrational frequencies of C_2H_4, the possibility that the hump originates from a vibrational hot band can be excluded. Careful examination of the ionization thresholds of H_2S[52] and C_2H_2[53] reveals similar observations. It has been known that the electric field applied across the ion repeller in a photoionization experiment can lower the ionizing threshold.[54,55] Recently in a multiphoton ionization study of high Rydberg states in NO, Seaver et al.[56] pointed out that the prominent nf Rydberg states of NO are very long-lived and susceptible to ionization and that the nearly 50 cm^{-1} difference between the ionization threshold observed in a

photoionization experiment using a supersonic beam of NO by Ono et al.[45] and the IE of NO obtained by Miescher and Huber[57] is most likely due to field ionization. For polyatomic molecules such as C_2H_4, predissociation processes are usually very fast; hence, polyatomic molecules in high Rydberg states should be less susceptible to field ionization with the exception of Rydberg states with very high effective principal quantum numbers.[58] In accordance with the above discussion it is logical to believe that the small hump arises from field ionization of very high Rydberg states converging to the IE of C_2H_4.[59]

Figure 1(b) shows the PIE curve for $C_2H_4^+$ in the region 1161-1182 Å obtained with a wavelength resolution of 0.14 Å (FWHM). No additional structure is resolved in the high resolution spectrum. Autoionization features appear to be broad and weak, indicating that the completing process of predissociation is much more probable than autoionization. Assuming that the wavelength spans (~ 1.0 Å) of the rapidly rising steps were caused by a finite rotational temperature of C_2H_4 in the beam, the rotational temperature of C_2H_4 is estimated to be ~ 50 K which seems to be a reasonable value for the nozzle expansion conditions used in this experiment. It is likely that field ionization also has a finite contribution at the rapidly rising steps. If the midpoint of the first rapidly rising step is taken to be the IE of the $\tilde{X}^2B_{3u}$ state of $C_2H_4^+$, the value of 10.505±0.004 eV (1180.3±0.5 Å) is in agreement with values for the IE of C_2H_4 determined previously by absorption study[60], photoelectron spectroscopy,[61-66] and photoionization studies.[47-50,67-70] The values for $2\nu_4$ and ν_2 were determined to be 433±35 and 1260±40 cm^{-1},

respectively, which are also consistent with previously reported measurements.[47,48,61,63]

According to previous photoionization studies,[47-49,71] there is no measurable excess activation energy for the process

$$C_2H_4 + h\nu \longrightarrow C_2H_2^+ + H_2. \qquad (7)$$

Using the known thermochemical data for C_2H_4[72] and $C_2H_2^+$ (317.1±0.2 kcal/mol),[73] the thermochemical threshold at 0 K for reaction (7) is calculated to be ΔH°_{f0} = 302.5±0.2 kcal/mol. If the rotational temperature of C_2H_4 in the beam is higher than 0 K, one expects to find the AE for the formation of $C_2H_2^+$ from C_2H_4 to be lower than the thermochemical threshold. The PIE curve for $C_2H_2^+$ from C_2H_4 in the region 934-948 Å obtained using a wavelength resolution of 0.14 Å (FWHM) is shown in Fig. 2. The rise of the PIE curve for $C_2H_2^+$ near the threshold is linear and a distinct onset is evidenced at 945.8±0.2 Å (302.29±0.06 kcal/mol). The excellent agreement found between the thermochemical threshold and the measured AE for $C_2H_2^+$ indicates that the rotational temperature of C_2H_4 in the beam is close to 0 K, a conclusion consistent with the estimate from the wavelength span of the rapidly rising step.

The pressure dependence of the relative intensities for $C_3H_5^+$, $C_4H_7^+$, $(C_2H_4)_2^+$, $(C_2H_4)_3^+$ and $(C_2H_4)_4^+$ measured at 1160 Å and T_0 ~ 210 K is plotted in Fig. 3. The pressure dependence of the relative intensities for various ions measured here is in qualitative agreement

Figure 2. PIE curve for $C_2H_2^+$ from C_2H_4 in the region of 933-948 Å obtained using the helium Hopfield continuum as the the light source [wavelength resolution = 0.14 Å (FWHM), P_o ~ 500 Torr, T_o ~ 298 K].

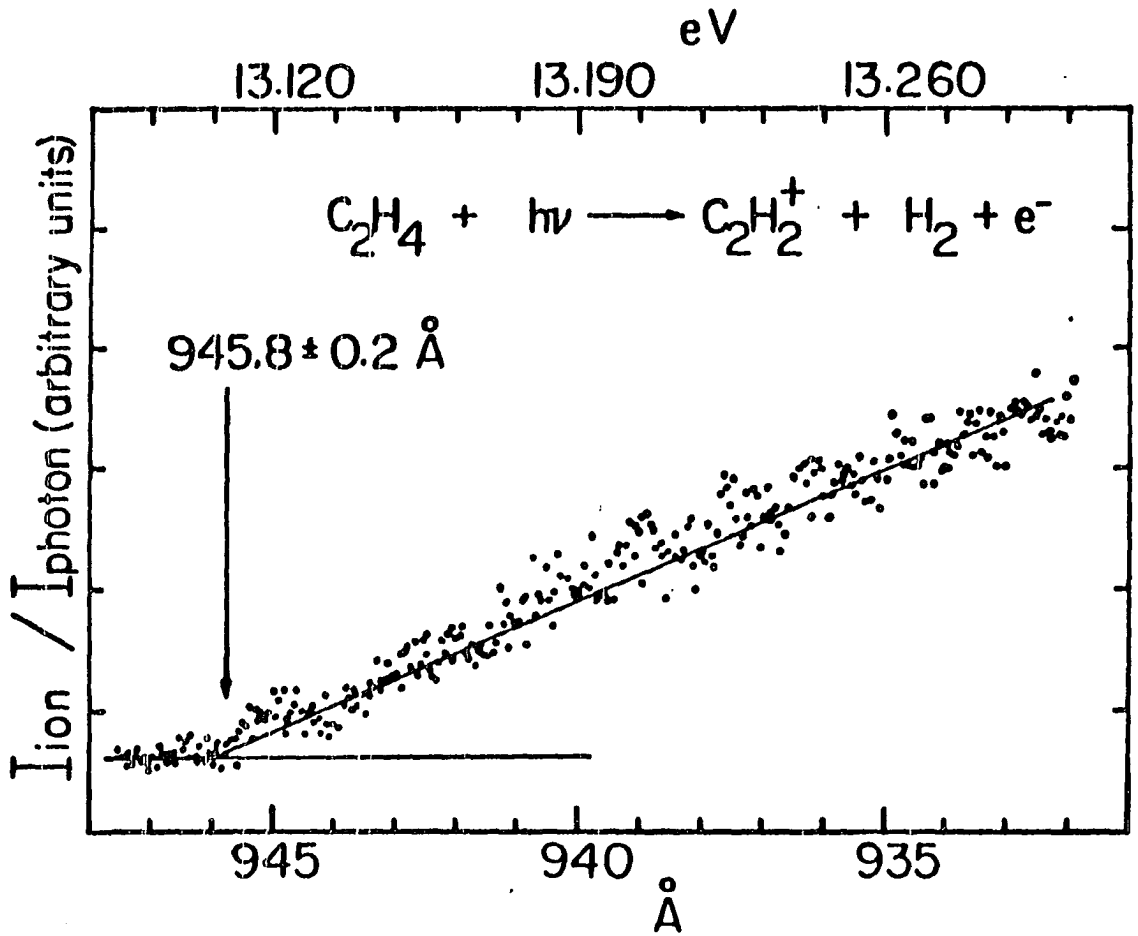
eV
13.120
13.190
13.260
$C_2H_4 + h\nu \longrightarrow C_2H_2^+ + H_2 + e^-$
945.8 ± 0.2 Å
I_{ion} / I_{photon} (arbitrary units)
945
940
935
Å

Figure 3. The pressure dependence of the relative intensities for $C_3H_5^+$, $C_4H_7^+$, $(C_2H_4)_2^+$, $(C_2H_4)_3^+$, and $(C_2H_4)_4^+$ measured at 1160 Å and T_o ~ 210 K.

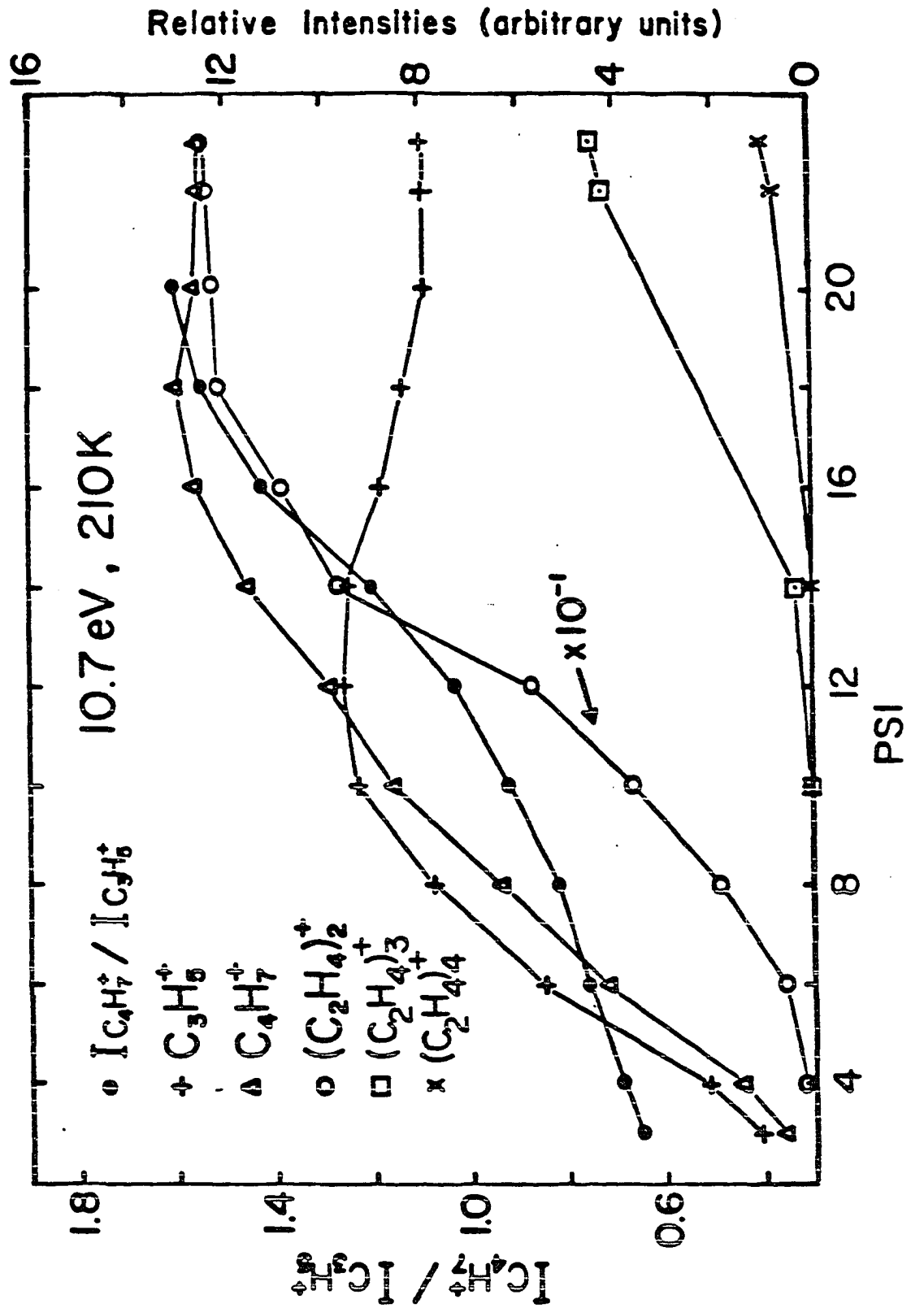
Relative Intensities (arbitrary units)
16
12
8
4
0
10.7 eV, 210K
• $I_{C_4H_7^+} / I_{C_3H_5^+}$
+ $C_3H_5^+$
Δ $C_4H_7^+$
○ $(C_2H_4)_2^+$
□ $(C_2H_4)_3^+$
× $(C_2H_4)_4^+$
×10⁻¹
4
8
12
16
20
PSI
1.8
1.4
1.0
0.6
$I_{C_4H_7^+} / I_{C_3H_5^+}$

with that observed by Ceyer et al.[32] Since the formation of these ions depends on the photon energy, the difference observed between this measurement and that of Ceyer et al. is partly due to the fact that their measurement was made with the monochromator adjusted to zero order.[74] The intensities for $(C_2H_4)_3^+$ and higher ethylene cluster ions are negligible at $P_0 \leq 10$ psi. The appearance of $(C_2H_4)_3^+$ seems to correlate with a more dramatic increase in intensity for $(C_2H_4)_2^+$ in the region ~ 11-14 psi. In the region ~ 3-11 psi, the intensities for $C_3H_5^+$, $C_4H_7^+$, and $(C_2H_4)_2^+$ are found to increase as P_0 increases. This trend is in accord with the expectation that the $C_3H_5^+$ and $C_4H_7^+$ ions mainly arise from the decomposition of $(C_2H_4)_2^+$ in this region. The intensity for $C_3H_5^+$ shows a slight decline from ~ 11 psi toward higher stagnation pressures, whereas the intensity for $C_4H_7^+$ continues to increase as the intensity for $(C_2H_4)_3^+$ begins to rise. These observations indicate that the $C_4H_8^+$ (and/or $(C_2H_4)_2^+$) and $C_4H_7^+$ ions can be produced by ethylene trimers possibly via reactions (3) and (4), respectively, and that the process

$$(C_2H_4)_3 \xrightarrow{h\nu} (C_2H_4)_3^+ + e^- \longrightarrow [C_6H_{12}^+]^* + e^-$$

$$\longrightarrow C_3H_5^+ + C_3H_7 + e^- \qquad (8)$$

is less probable than reactions (3) and (4). The more rapid rise in the ratio $I(C_4H_7^+)/I(C_3H_5^+)$ at higher stagnation pressures (> 11 psi) can be attributed to the increase in intensity for $(C_2H_4)_3$ in the beam. Here

Table I. 298 K heats of formation in kcal/mol of neutrals and ions[a]

Compounds	Neutrals	Ions
$(C_2H_4)_3$	42.90±0.15[b,c](72,75)	261.2±0.9[c](76)
$(C_2H_4)_2$	24.66±0.1(72,75)	253.6±0.9[d]
	28.74±0.1[c](72,75)	
1-butene		221(34)
Cis-2-butene		208(34)
Cyclobutane		238(34)
Isobutene		208(34)
Methylcyclopropane		239(34)
C_4H_7		206±2(34)
		204.2±2[e]
C_3H_7	17.6(77)	

[a]The numbers in the parentheses are the references.

[b]This value is calculated by assuming the binding energy for $(C_2H_4)_2 + C_2H_4$ to be the same as that for $C_2H_4 + C_2H_4$.

[c]Heat of formation at 0 K.

[d]This work. Because of the high degree of rotational relaxation in the supersonic expansion, this value, which is deduced from the measured IE of $(C_2H_4)_2$, can be considered to be the heat of formation at 0 K.

[e]Heat of formation at 0 K. This value is converted from the heat of formation at 298 K by assuming an ideal-gas model and excluding any vibrational and electronic contributions to the heat capacity at constant pressure.

Table I. (continued)

Compoundas	Neutrals	Ions
$n\text{-}C_3H_7$	22.6±1.1(78)	
	21.1±1(79)	
$i\text{-}C_3H_7$	20.0±1.1(78)	
	18.2±1(79)	
C_3H_5		226±2(34)
		224.5±1.0(80)
		225.5±1.1(81)
		226±1(82)
		223.7±1.5[e,f]
C_2H_5	25.7(77)	
	28.3±1.1(78)	
	25.9±1(79)	
C_2H_4	12.54±0.07[c](72)	258[c,d](73)
	14.58±0.07(72)	
CH_3	34.8±0.2(72)	
	35.1±0.5(78,79)	
	35.62±0.2[c](72)	
H	52.100±0.001(72)	
	51.631±0.001[c](72)	

[f]This value derives from the average value (255.5 kcal/mol) of the heats of formation reported in Refs. 34 and 80-82. See the text.

$I(C_4H_7^+)$ and $I(C_3H_5^+)$ represent the intensities of $C_4H_7^+$ and $C_3H_5^+$, respectively. By using the known values for the heats of formation of $(C_2H_4)_3^+$, $C_4H_8^+$, $C_4H_7^+$, $C_3H_5^+$, C_3H_7, and C_2H_5 as listed in Table I,[34,71-80] the formations of $C_4H_8^+ + C_2H_4$, $C_4H_7^+ + C_2H_5$, and $C_3H_5^+ + C_3H_7$ from $(C_2H_4)_3^+$ are predicted to be exothermic by ~ 33, 22, and 11 kcal/mol, respectively. The lower exothermicity in the formation of $C_3H_5^+ + C_3H_7$ in comparison with those of the other channels is likely to be the reason for the lower reaction probability for reaction (8) than those for reactions (3) and (4).

It is interesting to note that the ratio $I(C_4H_7^+)/I(C_3H_5^+)$ increases nearly linearly in the region 3-10 psi where the intensities for $(C_2H_4)_3^+$ and higher ethylene cluster ions are negligible. Previous studies [33,83,84] show that relative abundances of the three product channels $C_2H_4^+ + C_2H_4$, $C_3H_5^+ + CH_3$, and $C_4H_7^+ + H$ are strong functions of both energy and angular momentum in the reactant $C_4H_8^+$ ions. According to Meisels et al.,[83] if the fragmentation of the reaction complex $[C_4H_8^+]^*$ is treated in the quasidiatomic approximation, and the attractive potential is governed entirely by the ion-induced dipole interaction, the maximum in the effective potential energy barrier ($V_{eff,max}$) along the dissociative reaction coordinate is related to the reduced mass (μ) of the quasidiatomic complex, the total angular momentum (J), and the polarizability of the neutral fragment (α) by the relation $V_{eff,max} = J^4/8\alpha e^2\mu^2$. In this case, $\alpha(H) = 0.667$ Å^3, $\alpha(CH_3) = 2.2$ Å^3, and μ associated with the $C_3H_5^+ + CH_3$ channel are ~ 11 times that for the $C_4H_7^+ + H$ channel. Thus, $V_{eff,max}$ for H ejection is

greater than that for CH_3 elimination, and the formation of $C_3H_5^+ + CH_3$ is predicted to be the favorable channel for higher J values. The model calculations of Chesnavich et al.[33] suggest that the $[C_4H_8^+]^*$ intermediates with high J values react preferentially to the $C_3H_5^+ + CH_3$ channel because the rotational constant associated with the tight transition state in this channel is smaller than the one associated with the tight transition state in the $C_4H_7^+ + H$ channel. The difference in the rotational constants allows higher J systems to pass through the tight transition state in the $C_3H_5^+ + CH_3$ channel than can pass through the tight transition state in the $C_4H_7^+ + H$ channel. Undoubtedly, if $(C_2H_4)_2^+$ is the precursor of the $[C_4H_8^+]^*$ complex, the initial rotational angular momentum of $(C_2H_4)_2^+$ will contribute to the total angular momentum of $[C_4H_8^+]^*$. The rotational temperature for $(C_2H_4)_2$ prepared in the supersonic expansion is likely to decrease as the stagnation pressure increases in the range of 3-10 psi. Since the rotational temperature for $(C_2H_4)_2^+$ formed by photoionization is essentially the same as $(C_2H_4)_2$, one expects that the reaction complex $[C_4H_8^+]^*$ formed at higher P_0 will have a smaller total angular momentum than that of a reaction complex produced at lower P_0. Following the above discussion, the gradual rise in the ratio $I(C_4H_7^+)/I(C_3H_5^+)$ in the range of 3-10 psi can be rationalized to be the result of a more efficient rotational cooling when a higher stagnation pressure is employed in the nozzle expansion.

Although the intensities for $(C_2H_4)_3^+$ and higher ethylene cluster ions are nearly unobservable at $P_0 \leq 10$ psi, this by no means excludes

reactions (3), (4), and (8) as possible sources for $(C_2H_4)_2^+$ (and/or $C_4H_8^+$), $C_4H_7^+$, and $C_3H_5^+$. Since the formation of $C_3H_5^+$, $C_4H_7^+$ and $C_4H_8^+$ from $(C_2H_4)_3^+$ are all exothermic, it is reasonable to believe that the decompositions of the $(C_2H_4)_3^+$ ions prepared at 1160 Å (10.7 eV) according to reactions (3), (4), and (8) are efficient and that the observed signals for $C_4H_8^+$ (and/or $(C_2H_4)_2^+$), $C_4H_7^+$, and $C_3H_5^+$ at $P_0 \leq$ 10 psi still have minor contributions from the ethylene trimers.

Figure 4 shows the variation of the branching ratio $I(C_4H_7^+)/I(C_3H_5^+)$ as a function of photon energy measured at $P_0 \sim 1000$ Torr and $T_0 \sim 198$ K. The ratio $I(C_4H_7^+)/I(C_3H_5^+)$ was found to decrease dramatically from a value of 1.6 at 1185 Å to 0.5 at 1160 Å and then gradually to 0.3 at 950 Å. The decreasing trend was also observed previously in the study of the ion-molecule reaction of $C_2H_4^+ + C_2H_4$ induced by VUV photons.[2] At low reactant internal and kinetic energies, the branching ratio measured in collisional experiments of $C_2H_4^+ + C_2H_4$ is about 0.10-0.12.[2,3,85] The branching ratio from different $C_4H_8^+$ precursors determined in a state-selected photoionization experiment with an internal energy of 2.57 eV with respect to the most stable $C_4H_8^+$ isomer (2-butene or isobutene ion) is ~ 0.4.[83,86] The difference between the branching ratio observed in collisional experiments and that measured from the stable $C_4H_8^+$ isomer has been shown to be due to the angular momentum effect.[33,83] An internal energy of 2.57 eV of $C_4H_8^+$, with respect to the most stable $C_4H_8^+$ isomer, is equal to ~ 267.5 kcal/mol in the total energy scale [$\Delta H_f(2\text{-}C_4H_8^+$ or iso-$C_4H_8^+$) plus internal energy]. The latter value corresponds to an energy slightly

Figure 4. The wavelength dependence of the ratio of the intensity for $C_4H_7^+$ to that for $C_3H_5^+$ measured at P_o ~ 1000 Torr and T_o ~ 298 K. $I(C_4H_7^+)$ and $I(C_3H_5^+)$ are the intensities for $C_4H_7^+$ and $C_3H_5^+$, respectively.

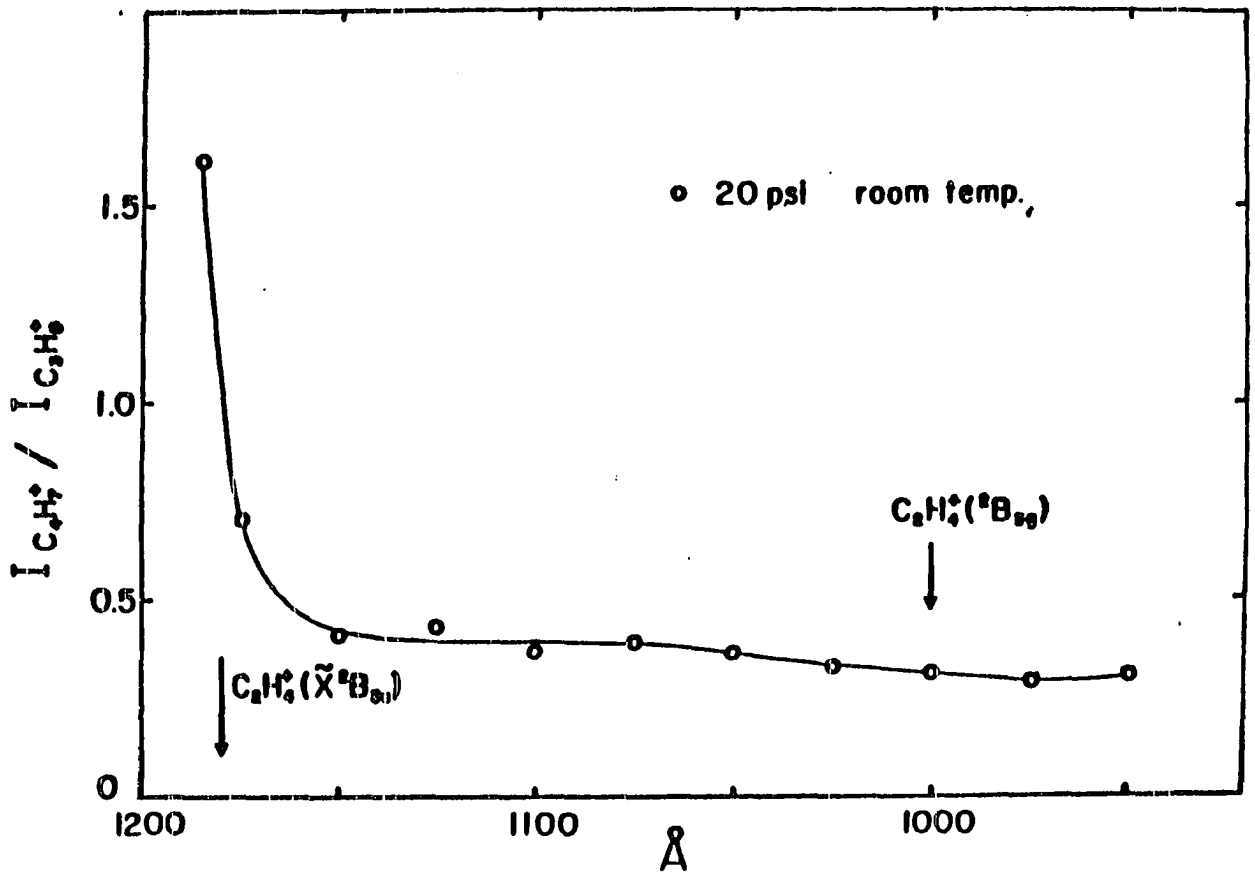
o 20 psi room temp.
$I_{C_2H_4^+} / I_{C_3H_8^+}$
1.5
1.0
0.5
0
1200
1100
1000
Å
$C_2H_4^+(\tilde{X}^2B_{3u})$
$C_2H_4^+(^2B_{2g})$

above the $C_2H_4^+ + C_2H_4$ threshold. At 10.55 eV (1175 Å), which is 0.04 eV above the threshold, the ratio $I(C_4H_7^+)/I(C_3H_5^+)$ from $(C_2H_4)_2^+$ is determined to be ~ 0.7. Since this is not a state-selected experiment, it is not appropriate to compare the branching ratio observed here with those measured by Hsieh et al.[86] In a study of the bimolecular reactions $C_2H_4^+ + C_2H_4$ induced at 1165 Å, Sieck and Ausloos[2] obtained a value of 0.17 for $I(C_4H_7^+)/I(C_3H_5^+)$. The value for the branching ratio at 1165 Å, estimated from Fig. 4, is ~ 0.55. This difference can also be attributed to lower angular momentum involved in the decomposition of $(C_2H_4)_2^+$ than in the decomposition of the complex formed in the bimolecular reactions of $C_2H_4^+ + C_2H_4$.

The thresholds for reactions (5) and (6) and the ionization process

$$(C_2H_4)_2 + h\nu \longrightarrow (C_2H_4)_2^+ + e^- \qquad (9)$$

have been investigated with great care. Figures 5(a)-(f) compare the PIE curves for $(C_2H_2)_2^+$, $C_4H_7^+$, and $C_3H_5^+$ near the thresholds obtained at P_0 ~ 480 Torr and T_0 ~ 210 K to those measured at P_0 ~ 1000 Torr and T_0 ~ 210 K. At P_0 ~ 480 Torr and T_0 ~ 210 K, the observed intensity for $(C_2H_4)_3^+$ is less than 0.5% of that for $(C_2H_4)_2^+$ at 1160 Å. If the measured intensities for $(C_2H_4)_3^+$ and $(C_2H_4)_2^+$ directly reflect those of the corresponding neutrals, the threshold determined in Figs. 5(b), 5(d), and 5(f), which are based on the results of several repetitive scans, can be assigned to be the IE for $(C_2H_4)_2$ and the AE's for $C_4H_7^+$ and $C_3H_5^+$ from $(C_2H_4)_2$, respectively. These thresholds have also been

Figure 5. PIE curves for $C_4H_8^+$, $(C_2H_4)_2^+$, $C_4H_7^+$, and $C_3H_5^+$ near the threshold.

(a) PIE curve for $C_4H_8^+$ near the threshold [wavelength resolution = 1.4 Å (FWHM), P_0 ~ 1000 Torr, T_0 ~ 210 K].

(b) PIE curve for $(C_2H_4)_2^+$ near the threshold [wavelength resolution = 1.4 Å (FWHM), P_0 ~ 480 Torr, T_0 ~ 210 K].

(c) PIE curve for $C_4H_7^+$ near the threshold [wavelength resolution = 1.4 Å (FWHM), P_0 ~ 1000 Torr, T_0 ~ 210 K].

(d) PIE curve for $C_4H_7^+$ near the threshold [wavelength resolution = 1.4 Å (FWHM), P_0 ~ 480 Torr, T_0 ~ 210 K].

(e) PIE curve for $C_3H_5^+$ near the threshold [wavelength resolution = 1.4 Å (FWHM), P_0 ~ 1000 Torr, T_0 ~ 210 K].

(f) PIE curve for $C_3H_5^+$ near the threshold [wavelength resolution = 1.4 Å (FWHM), P_0 ~ 480 Torr, P_0 ~ 210 k].

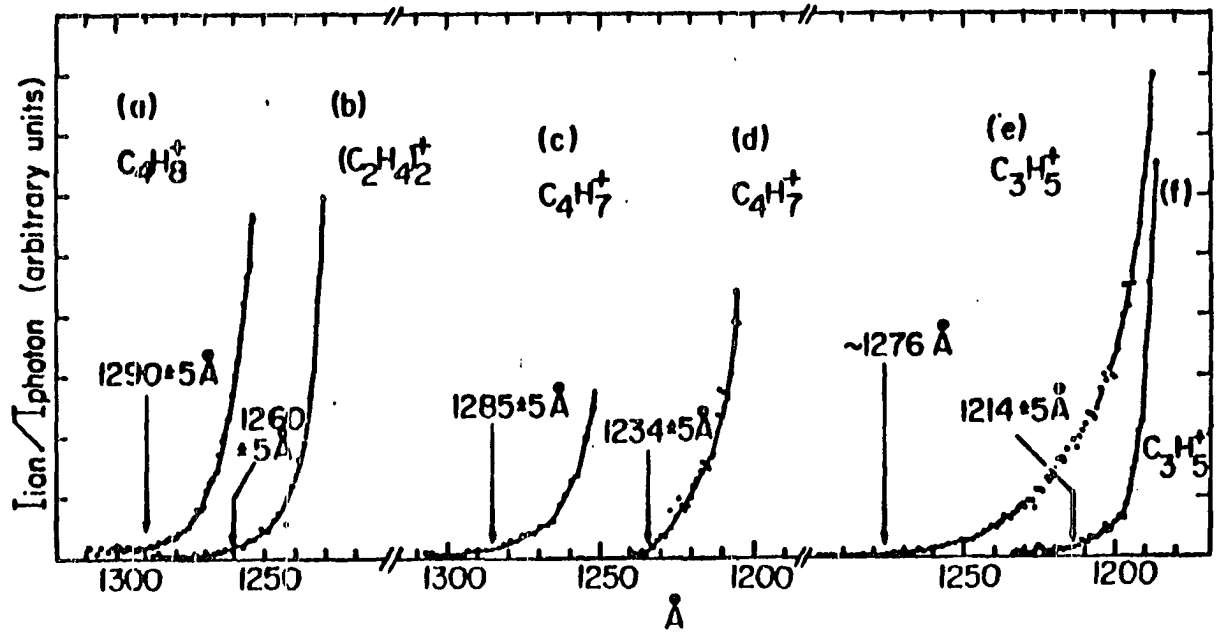
(a)
$C_4H_8^+$
(b)
$(C_2H_4)_2^+$
(c)
$C_4H_7^+$
(d)
$C_4H_7^+$
(e)
$C_3H_5^+$
(f)
1290±5Å
1260 ±5Å
1285±5Å
1234±5Å
~1276 Å
1214±5Å
$C_3H_5^+$
I ion / I photon (arbitrary units)
1300
1250
1300
1250
1200
1250
1200
Å

measured at P_0 ~ 1000 Torr and T_0 ~ 298 K, where the intensity for $(C_2H_4)_3^+$ and higher ethylene cluster ions were found to be within the noise level. The values obtained are within the error limits of the thresholds determined in Figs. 5(b), 5(d), and 5(f).

The IE of $(C_2H_4)_2$ is determined to be 9.84±0.04 eV (1260± 5 Å). This value is 0.12 eV higher than the value obtained by Ceyer et al.[32] The interaction potential of the ethylene dimer has been the subject of many theoretical calculations.[87-92] Depending on the geometry of the ethylene dimer, these calculations yield values for the well depth for the $C_2H_4 + C_2H_4$ interaction in the range ~ 0.2-12.1 kcal/mol. The average value for the dissociation energy of $(C_2H_4)_2$ derived from second virial coefficient and viscosity measurements[75] is 0.42±0.03 kcal/mol. Using the latter value, the IE's of C_2H_4[73] and $(C_2H_4)_2$, the dissociation energy for $(C_2H_4)_2^+$ is calculated to be 15.8±1 kcal/mol. This value is substantially lower than the binding energy for $C_2H_2^+ + C_2H_2$ (22.5±1 kcal/mol) which has been determined previously in a similar experiment.[38] Nevertheless, it is found to be in good agreement with a theoretical value of 16 kcal/mol obtained by Almlof et al. in an ab initio study.[93]

As shown in Figs. 5(d) and 5(f), the AE's for the formation of the $C_4H_7^+$ and $C_3H_5^+$ are determined to be 10.047± 0.041 eV (1234±5 Å) and 10.213±0.042 eV (1214±5 Å), respectively. The AE for $C_3H_5^+$ observed here is approximately 0.2 eV lower than the previously reported value, whereas that for $C_4H_7^+$ is slightly higher than a value of 9.96 eV obtained by Ceyer et al.[32] According to known thermodynamical data (see

Table I), the thermochemical thresholds for the formations of $C_3H_5^+$ and $C_4H_7^+$ from $(C_2H_4)_2$ at 298 K are estimated to be 10.22±0.07 and 10.12±0.09 eV, respectively. The average value (225.5±1.5 kcal/mol) of the heats of formation for $C_3H_5^+$ reported in Refs. 34 and 80-82 has been used in the calculation. However, since the AE's for $C_3H_5^+$ and $C_4H_7^+$ obtained here are close to the values at 0 K, it is more appropriate to compare the experimental values with the thermochemical thresholds at 0 K. The values for $\Delta H^\circ_{f0}(C_3H_5^+)$ and $\Delta H^\circ_{f0}(C_4H_7^+)$ are not known. Assuming an ideal-gas model and excluding any vibrational and electronic contribution to the heat capacities, the values for $\Delta H^\circ_{f0}(C_3H_5^+)$ and $\Delta H^\circ_{f0}(H)$ are estimated to be 223.7±1.5 and 204.2±2 kcal/mol, respectively. The latter values, together with the known values for $\Delta H^\circ_{f0}(CH_3)$, $\Delta H^\circ_{f0}[(C_2H_4)_2]$, and $\Delta H^\circ_{f0}(C_4H_7)$ as listed in Table I, allow the calculation of the thermochemical thresholds for reactions (5) and (6) to be 10.00±0.07 and 9.85±0.09 eV, respectively. Taken into account the error estimates of the latter values and the experimental AE's, the thermochemical thresholds at 0 K are still lower than the experimental values by approximately 0.1 eV. In view of the estimated nature for the values of $\Delta H^\circ_{f0}(C_3H_5^+)$ and $\Delta H^\circ_{f0}(C_4H_7^+)$ used in the calculation and a finite rotational temperature for the C_2H_4 beam employed in this experiment, we feel that it is satisfactory to conclude from the AE measurements for $C_3H_5^+$ and $C_4H_7^+$ that the potential energy barriers for the reverse reactions of reactions (1) and (2) are negligible. This conclusion is also consistent with the previous interpretation that the reactions of $C_2H_4^+ + C_2H_4$ proceed through the loosely bound dimer $C_2H_4^+$

C_2H_4 ions and then rearrange to long-lived $[C_4H_8^+]^*$ complexes prior to dissociation.

At the nozzle expansion conditions, P_0 ~1000 Torr and T_0 ~ 210 K, the intensities of $(C_2H_4)_3^+$ and $(C_2H_4)_4^+$ are ~ 30% and 5% of $(C_2H_4)_2^+$, respectively. Therefore, it is logical to assume that the $C_4H_8^+$ [and/or $(C_2H_4)_2^+$], $C_4H_7^+$, and $C_3H_5^+$ ions observed in Figs. 5(a), 5(c), and 5(e) mostly originated from $(C_2H_4)_3$ and to a lesser extent from higher ethylene clusters. The most convincing evidence, which supports this assumption, is that the AE's for $C_4H_7^+$ [9.65 eV (1285 Å)] and $C_3H_5^+$ [~ 9.72 eV (1275 Å)] are lower than the corresponding thermochemical thresholds for $C_4H_7^+$ and $C_3H_5^+$ from ethylene dimers. The results and an analysis of a photoionization study of $(C_2H_4)_3$ will be reported in a separate publication.[76] The rise in PIE for $C_3H_5^+$ from $(C_2H_4)_3$ above the threshold, as shown in Fig. 5(e), is much more gradual than that for $C_4H_8^+$ [Fig. 5(a)] and $C_4H_7^+$ [Fig. 5(d)]. This indicates that the reaction probability for reaction (8) is much lower than that for reactions (3) and (4) near the thresholds, a conclusion in agreement with that deduced from the pressure dependence measurement (Fig. 3).

The PIE curves for $(C_2H_4)_2^+$, $C_3H_5^+$, $C_4H_7^+$ from $(C_2H_4)_2$ in the region ~ 650–1275 Å, obtained at P_0 ~ 480 Torr and T_0 ~ 210 K, are shown in Figs. 6(b), 6(c), and 6(d), respectively. The PIE curve for $C_2H_4^+$ obtained with the same wavelength resolution [1.4 Å (FWHM)] is shown in Fig. 6(a) for comparison. The PIE spectrum for $C_2H_4^+$ in the region 600–1185 Å recorded here is in excellent agreement with those reported previously.[47-49] The general profiles for the PIE spectra for $(C_2H_4)_2^+$,

Figure 6. PIE curves for $C_2H_4^+$, $(C_2H_4)_2^+$, $C_3H_5^+$, and $C_4H_7^+$ in the region of 600–1265 Å.

(a) PIE curve for $C_2H_4^+$ in the region of 600–1185 Å [wavelength resolution = 1.4 Å (FWHM), P_0 ~ 500 Torr, T_0 ~ 298 k].

(b) PIE curve for $(C_2H_4)_2^+$ in the region of 650–1265 Å [wavelength resolution = 1.4 Å (FWHM), P_0 ~ 480 Torr, T_0 ~ 210 k].

(c) PIE curve for $C_3H_5^+$ in the region of 650–1240 Å [wavelength resolution = 1.4 Å (FWHM), P_0 ~ 480 Torr, T_0 ~ 210 k].

(d) PIE curve for $C_4H_7^+$ in the region of 650–1250 Å [wavelength resolution = 1.4 Å (FWHM), P_0 ~ 480 Torr, T_0 ~ 210 K].

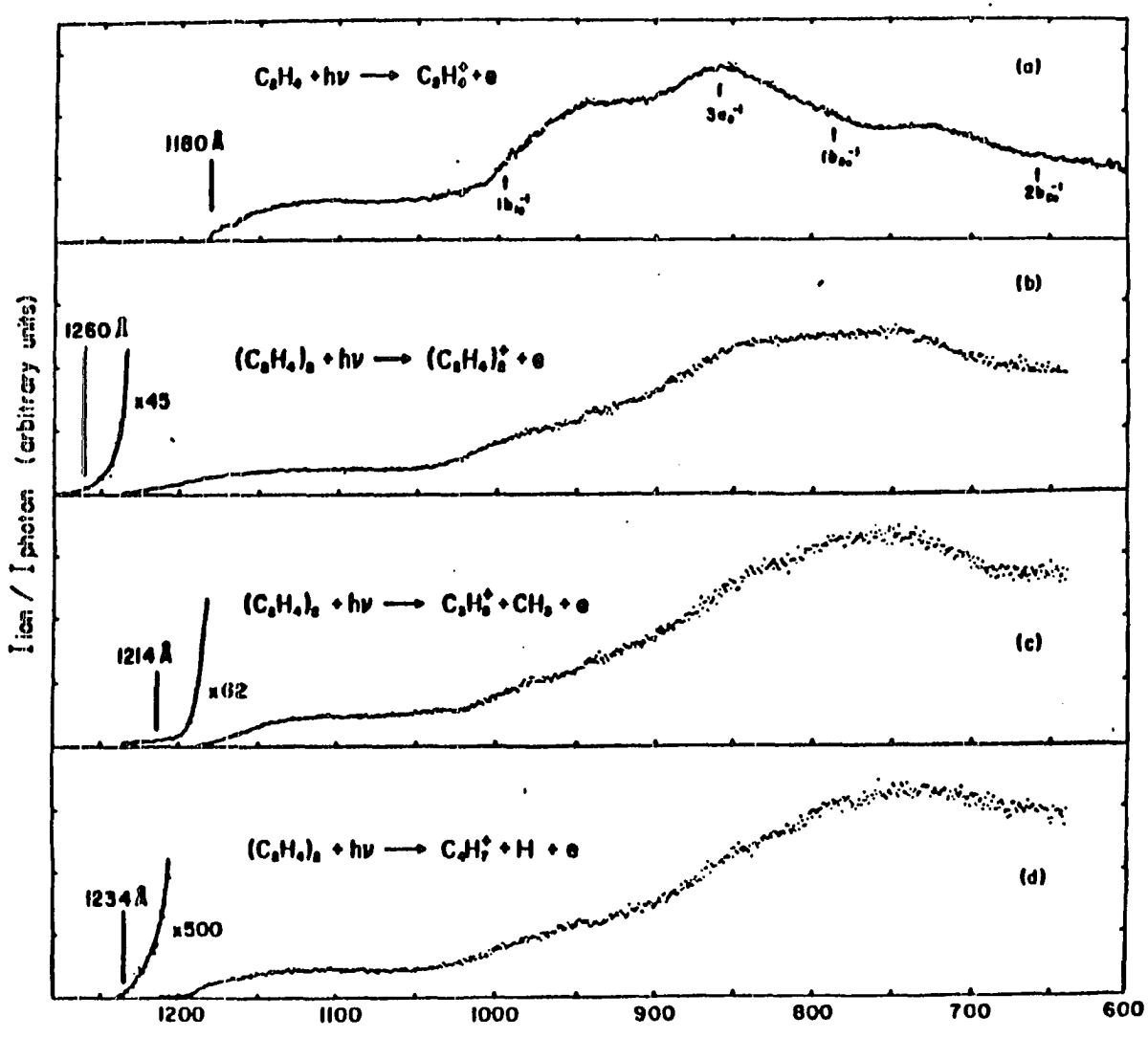
$C_6H_6 + h\nu \longrightarrow C_6H_6^+ + e$
(a)
1180 Å
$1b_{2u}^{-1}$
$3a_g^{-1}$
$1b_{2u}^{-1}$
$2b_{2u}^{-1}$
(b)
1260 Å
x45
$(C_6H_6)_2 + h\nu \longrightarrow (C_6H_6)_2^+ + e$
$(C_6H_6)_2 + h\nu \longrightarrow C_5H_5^+ + CH_3 + e$
1214 Å
x62
(c)
$(C_6H_6)_2 + h\nu \longrightarrow C_6H_7^+ + H + e$
1234 Å
x500
(d)
I_{ion} / I_{photon} (arbitrary units)
1200
1100
1000
900
800
700
600

$C_4H_7^+$ and $C_3H_5^+$ are similar. In the region ~ 650–950 Å, the appearance of the spectrum for $C_2H_4^+$ is markedly different from that for $(C_2H_4)_2^+$, $C_4H_7^+$, and $C_3H_5^+$. The formations of $C_2H_2^+$ and $C_2H_3^+$ from C_2H_4 have the AE's at 13.11 eV (945.8 Å) and 13.22 eV (938 Å),[49,71] respectively. At a photon energy of 21.2 eV, the relative abundance $C_2H_4^+$:$C_2H_3^+$:$C_2H_2^+$ was reported to be 100:137:76.[47] The relative yields for $C_2H_4^+$, $C_2H_3^+$, and C_2H_2 have not been measured in this experiment. However, when the PIE's for $C_2H_2^+$ and $C_2H_3^+$ observed by Botter et al.[47] were added to the PIE for $C_2H_4^+$ in this region, the profile of the summed PIE curve was found to be in rough resemblance to those for $(C_2H_4)_2^+$, $C_4H_7^+$, and $C_3H_5^+$. Similar observations have also been found in other systems such as SO_2[94] and H_2S.[95]

The relative abundances $I[(C_2H_4)_2^+]/\Sigma$, $I(C_4H_7^+)/\Sigma$, and $I(C_3H_5^+)/\Sigma$ for $(C_2H_4)_2^+$, $C_4H_7^+$, and $C_3H_5^+$, respectively, in percentage, as a function of photon energy in the region of 950–1250 Å, are plotted in Fig. 7. Here, $I[(C_2H_4)_2^+]$ represents the intensity for $(C_2H_4)_2^+$ and Σ is the sum of $I[(C_2H_4)_2^+]$, $I(C_4H_7^+)$, and $I(C_3H_5^+)$. The relative abundance diagram is based on PIE data for various ions measured at P_0 ~ 1000 Torr and T_0 ~ 298 K, at wavelength intervals of 25 Å. The differences in transmission of these ions through the mass spectrometer used in this experiment have not been corrected for. As a result of a much shorter time span in obtaining these data, in comparison to that needed for measurements of PIE data shown in Figs. 6(b)–6(d), the data plotted in Fig. 7 are believed to be less susceptible to minor experimental fluctuations and thus more representative of the relative

Figure 7. The variations of the relative abundances for $(C_2H_4)_2^+$(O), $C_4H_7^+$(Δ), and $C_3H_5^+$(+) as a function of photon energy. Σ is the sum of $I[(C_2H_4)_2^+]$, $I(C_4H_7^+)$, and $I(C_3H_5^+)$, where $I[(C_2H_4)_2^+]$, $I(C_4H_7^+)$, and $I(C_3H_5^+)$ represent the intensities for $(C_2H_4)_2^+$, $C_4H_7^+$, and $C_3H_5^+$, respectively. No corrections were made to account for transmission factors of these ions through the mass spectrometer used in this experiment [wavelength resolution = 1.4 Å (FWHM), P_0 ~ 1000 Torr, T_0 ~ 298 K].

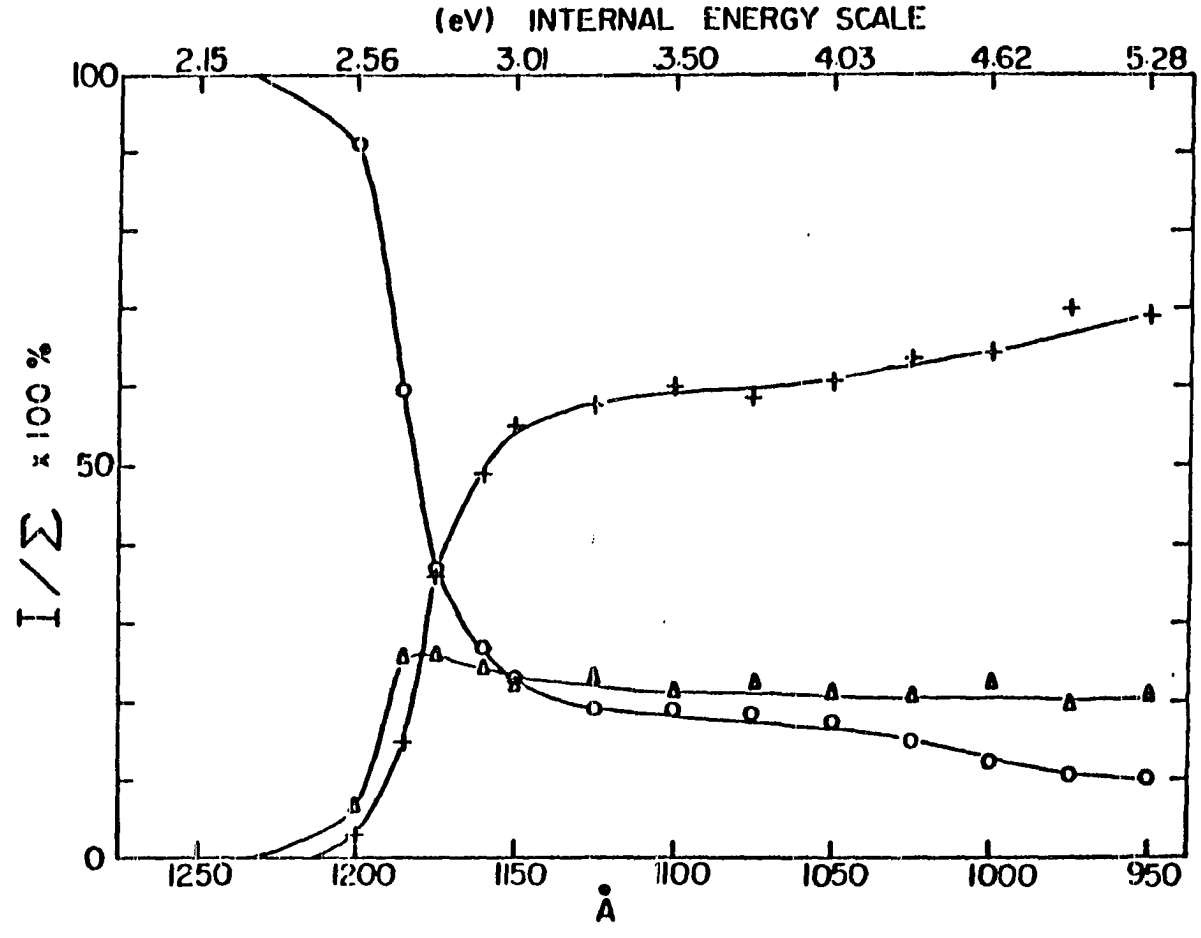
(eV) INTERNAL ENERGY SCALE
2.15
2.56
3.01
3.50
4.03
4.62
5.28
100
50
0
I / Σ x 100 %
1250
1200
1150
1100
1050
1000
950
Å

abundances of these ions. Despite the fact that the PIE data obtained here are not state-selected data and that the dissociation channel to form $C_2H_4^+ + C_2H_4$ from $(C_2H_4)_2^+$ cannot be probed in this experiment and thus is not included, the relative abundances of $(C_2H_4)_2^+$, $C_4H_7^+$, and $C_3H_5^+$ as a function of photon energy are in qualitative agreement with breakdown curves observed for $C_4H_8^+$, $C_4H_7^+$, and $C_3H_5^+$ from various $C_4H_8^+$ precursor ions in a photoion-photoelectron coincidence study.[86] The corresponding values between photon wavelengths and internal energies, with respect to the most stable $C_4H_8^+$ isomer ($2\text{-}C_4H_8^+$ or $iso\text{-}C_4H_8^+$), are also shown in Fig. 7.

In summary, the photoionization of $(C_2H_4)_2$ has been investigated with higher sensitivity. The AE's for $C_3H_5^+$ and $C_4H_7^+$ measured in nozzle expansion conditions, which have minimized the formations of ethylene trimers and higher clusters, are found to be in fair agreement with the thermochemical thresholds for reactions (5) and (6), respectively. This and the qualitative agreement found in the relative abundances for $(C_2H_4)_2^+$, $C_4H_7^+$, and $C_3H_5^+$ observed here and those measured previously for $C_4H_8^+$, $C_4H_7^+$, and $C_3H_5^+$ from various $C_4H_8^+$ isomers in a state-selected experiment can be taken as evidence that the major fragmentation pathway for $(C_2H_4)_2^+$ involves the rearrangement to some stable $C_4H_8^+$ isomers prior to dissociation.

References

1. T. O. Tiernan and J. H. Futrell, J. Phys. Chem. 72, 3080 (1968).

2. L.W. Sieck and P. Ausloos, J. Res. Natl. Bur. Stand. Sect. A 76, 253 (1972).

3. P. R. LeBreton, A. D. Williamson, J. L. Beauchamp, and W. T. Huntress, J. Chem. Phys. 62, 1623 (1975).

4. J. J. Meyer and A. G. Harrison, Can. J. Chem. 46, 101 (1968).

5. F. H. Field, J. L. Franklin, and F. W. Lampe, J. Am. Chem. Soc. 79, 2419 (1957).

6. C. E. Melton and P. S. Rudolph, J. Chem. Phys. 32, 1128 (1960).

7. Von R. Fuchs, Z. Naturforsch. Teil A 16, 1026 (1961).

8. F. H. Field, J. Am. Chem. Soc. 83, 1523 (1961).

9. A. G. Harrison, Can. J. Chem. 41, 236 (1961).

10. S. Wexler and R. Marshall, J. Am. Chem. Soc. 86, 781 (1964).

11. P. Kebarle and A. M. Hogg, J. Chem. Phys. 42, 668 (1965).

12. I. Saabo, Arkiv Fysik. 33, 57 (1966).

13. P. Kebarle, R. M. Hayes, and S. Searles, Adv. Chem. Ser. 58, 210 (1966).

14. S. Wexler, A. Lifshitz, and A. Quattrochi, Adv. Chem. Ser. 58, 193 (1966).

15. G. G. Meisels, J. Chem. Phys. 42, 2328 (1965).

16. G. G. Meisels, J. Chem. Phys. 42, 3237 (1965).

17. P. Warneck, Ber. Bunsenges, Phys. Chem. 76, 421 (1972).

18. M. T. Bowers, D. D. Elleman, and J. L. Beauchamp, J. Phys. Chem. 72, 3599 (1968).

19. M. L. Gross and J. Norbeck, J. Chem. Phys. 54, 3651 (1971).

20. R. M. O'Malley and K. R. Jennings, Int. J. Mass Spectrom. Ion Phys. 2, 441 (1969).

21. W. T. Huntress, J. Chem. Phys. 56, 5111 (1972).

22. Z. Herman, A. Lee, and R. Wolfgang, J. Chem. Phys. 51, 452 (1969).

23. A. Lee, R. L. Leory, Z. Herman, and R. Wolfgang, Chem. Phys. Lett. 12, 569 (1972).

24. J. Weiner, A. Lee, and R. Wolfgang, Chem. Phys. Lett. 13, 613 (1972).

25. I. H. Suzuki and K. Maeda, Int. J. Mass Spectrom. Ion Phys. 17, 253 (1975).

26. A. A. Herod and A. G. Harrison, Int. J. Mass Spectrom. Ion Phys. 4, 415 (1970).

27. P. G. Miasek and A. G. Harrison, J. Am. Chem. Soc. 97, 714, (1975).

28. A. J. Ferrer-Correia and K. R. Jennings, Int. J. Mass Spectrom. Ion Phys. 11, 111 (1973).

29. P. S. Gill, Y. Inel, and G. G. Meisels, J. Chem. Phys. 54, 2811 (1971).

30. P. Kebarle and R. M. Haynes, J. Chem. Phys. 47, 1676 (1967).

31. S. G. Lias and P. Ausloos, J. Am. Chem. Soc. 92, 1840 (1970).

32. S. T. Ceyer, P. W. Tiedemann, C. Y. Ng, B. H. Mahan, and Y. T. Lee, J. Chem. Phys. 70, 2138 (1979).

33. W. J. Chesnavich, L. Bass, T. Su, and M. T. Bowers, J. Chem. Phys. 70, 2138 (1981).

34. F. P. Lossing, Can. J. Chem. 50, 3937 (1972).

35. T. Baer, D. Smith, B. P. Tsai, and A. S. Werner, Adv. Mass Spectrom. A7, 56 (1978).

36. P. A. M. Kemper and M. T. Bowers (unpublished data).

37. Y. Ono and C. Y. Ng, J. Am. Chem. Soc. 104, 4752 (1982).

38. Y. Ono and C. Y. Ng, J. Chem. Phys. 77, 2947 (1982).

39. A. A. Herod, A. G. Harrison, R. M. O'Malley, A. J. Ferror-Correia, and K. R. Jennings, J. Phys. Chem. 74, 2720 (1970).

40. J. M. S. Henis, J. Chem. Phys. 52, 292 (1970).

41. I. Koyano, I. Omura, and I. Tanaka, J. Chem. Phys. 44, 3850 (1966).

42. F. P. Abramson and J. H. Futrell, J. Phys. Chem. 72, 1994 (1968).

43. A. MacKenzie Peers, Int. J. Mass Spectrom. Ion Phys. 5, 483 (1970).

44. Y. Ono, S. H. Linn, H. F. Prest, M. E. Gress, and C. Y. Ng, J. Chem. Phys. 73, 2523 (1980).

45. Y. Ono, S. H. Linn, H. F. Prest, C. Y. Ng, and E. Meisher, J. Chem. Phys. 73, 4855 (1980).

46. K. E. Schubert and R. D. Hudson, Rep. No. ATN-64(9233)-2 (Aerospace Corp., Los Angeles, 1963).

47. R. Botter, V. H. Dibeler, J. A. Walker, and H. M. Rosenstock, J. Chem. Phys. 45, 1298 (1966).

48. B. Brehm, Z. Naturforsch. Teil A 21, 196 (1966).

49. W. A. Chupka, J. Berkowitz, and K. M. A. Refaey, J. Chem. Phys. 50, 1938 (1969).

50. K. V. Wood and J. W. Taylor, Int. J. Mass Spectrom. Ion Phys. 30, 307 (1979).

51. G. Herzberg, Molecular Spectra and Molecular Structure III. Electronic Spectra and Electronic Structure of Polyatomic Molecules (Van Nostrand Reinhold, New York, 1966), p. 629.

52. H. F. Prest, W.-B. Tzeng, J. M. Brom, Jr., and C. Y. Ng, Int. J. Mass Spectrom. Ion Phys. 50, 315 (1983).

53. Y. Ono, E. A. Osuch, and C. Y. Ng, J. Chem. Phys. 76, 3905 (1982).

54. W. A. Chupka and J. Berkowitz, J. Chem. Phys. 51, 4244 (1969).

55. C. J. Bakker, Proc. R. Acad Sci. Amsterdam 36, 589 (1933).

56. M. Seaver, W. A. Chupka, S. D. Colson, and D. Gauyacq, J. Chem. Phys. 87, 2226 (1983).

57. E. Miescher and K. P. Huber in International Preview of Science, Physical Chemistry Series Two, edited by D. Ramsay (Butterworths, London, 1976), Vol. 3, and references therein.

58. The lifetime of a Rydberg state is expected to be proportional to n^{*3}, where n^* is the effective principal quantum number.

59. A reliable test of the field ionization effect is to observe the change in the ionization threshold by varying the ion-repeller field at the photoionization region. The usual ion-repeller field used in our experiment is in the range of 50-60 V/cm. Due to the specific experimental arrangement used in our apparatus, a severe loss in ion signal will result when the ion-repeller field is lower than 30 V/cm. We have examined the effect of the repeller field on the ionization threshold of H_2S. By varying the repeller field in the range 30-60 V/cm, only minor variations in the ionization threshold were observed. Thus, the test was not conclusive.

60. W. C. Price and W. T. Tuttle, Proc. Roy. Soc. London Ser. A 174, 207 (1940).

61. A. D. Baker, C. Baker, C. R. Brundle, and D. W. Turner, Int. J. Mass Spectrom. Ion Phys. 1, 285 (1968).

62. J. W. Rabalais, T. P. Debies, J. L. Berkosky, J. T. J. Huang, and F. O. Ellison, J. Chem. Phys. 61, 516 (1974).

63. G. R. Branton, D. C. Frost, T. Makita, C. A. McDowell, and I. A. Stenhouse, J. Chem. Phys. 52, 802 (1970).

64. C. R. Brundle, M. B. Robin, N. A. Kuebler, and H. Basch, J. Am. Chem. Soc. 94, 1451 (1972).

65. J. H. D. Eland, Int. J. Mass Spectrom. Ion Phys. 2, 471 (1969).

66. G. R. Branton, D. C. Frost, T. Makita, C. A. McDowell, and I. A. Stenhouse, Philos. Trans. Roy. Soc. London Ser. A 268, 77 (1970).

67. J. Momigny, Nature 199, 1179 (1963).

68. A. J. C. Nicholson, J. Chem. Phys. 43, 1171 (1965).

69. K. Watanabe, J. Chem. Phys. 22, 1564 (1954).

70. K. Watanabe, T. Nakayama, and J. Mottl, J. Quant. Spectrosc. Radiat. Transfer 2, 369 (1962).

71. R. Stockbauer and M. G. Inghram, J. Chem. Phys. 62, 4862 (1975).

72. D. R. Stull and H. Prophet, JANAF Thermochemical Tables, 2nd ed., NSRDS-NBS 37 (U.S. GPO, Washington, D.C., 1971).

73. H. M. Rosenstock, K. Draxl, B. W. Stiener, and J. T. Herron, J. Phys. Chem. Ref. Data, 6, Suppl. 1, 93, 99 (1977).

74. The hydrogen gas used to produce the hydrogen many-lined pseudo-continuum in the experiment of Ceyer, Tiedemann, Ng, Mahan, and Lee (Ref. 32) might contain a small amount of helium as impurity. The Ar^+ ions observed in their experiment were probably due to the HeI resonance line (584 Å) which was also generated in the discharge.

75. J. O. Hirshfelder, C. F. Curtiss, and R. B. Bird, Molecular Theory of Gases and Liquids (John Wiley & Sons, New York, 1954), p. 1112.

76. W.-B. Tzeng, Y. Ono, S. H. Linn, and C. Y. Ng, J. Chem. Phys. 83, 2813 (1985).

77. S. W. Benson and H. E. O'Neal, Kinetic Data on Gas Phase Unimolecular Reactions, NSRDS-NBS 21 (U.S. GPO, Washington, D.C., 1970).

78. W. v. E. Doering, Proc. Natl. Acad. Sci. USA 78, 5279 (1981).

79. D. F. McMillen and D. M. Golden, Annu. Rev. Phys. Chem. 33, 493 (1982).

80. S. E. Buttrill, Jr., A. D. William, and P. LeBreton, J. Chem. Phys. 62, 1586 (1975).

81. F. A. Houle and J. L. Beauchamp, J. Am. Chem. Soc. 100, 3290 (1978).

82. J. C. Traeger, Int. J. Mass Spectrom. Ion Phys. 32, 309 (1980).

83. G. G. Meisels, G. M. L. Verboom, M. J. Weiss, and T. C. Hsieh, J. Am. Chem. Soc. 79, 7189 (1979).

84. C. E. Klots, Kinetics of Ion-Molecule Reactions, edited by P. Ausloos (Plenum, New York, 1979).

85. J. L. Franklin, F. H. Field, and F. W. Lampe, J. Am. Chem. Soc. 78, 5697 (1956).

86. T. C. Hsieh, J. P. Gilman, M. J. Weiss, and G. G. Meisels, J. Phys. Chem. 85, 2722 (1981).

87. E. J. P. Malar and A. K. Chandra, J. Phys. Chem. 85, 2190 (1981).

88. M. Hashimoto and T. Isobe, Bull. Chem. Soc. Jpn. 46, 2381 (1973).

89. P. E. S. Wormer and A. van der Avoird, J. Chem. Phys. 62, 3326 (1975).

90. A. van der Avoird, P. E. S. Wormer, F. Mulder, and R. M. Berns, Topics Curr. Chem. 93, 1 (1980).

91. K. Suzuki and K. Iguchi, J. Chem. Phys. 75, 779 (1978).

92. K. Suzuki and K. Iguchi, J. Chem. Phys. 77, 4594 (1982).

93. J. Almlof, A. Lund, and K. A. Thuomas, Chem. Phys. Lett. 32, 190 (1975).

94. J. Erickson and C. Y. Ng, J. Chem. Phys. 75, 1650 (1981).

95. H. F. Prest, W.-B. Tzeng, J. M. Brom, Jr., and C. Y. Ng, J. Am. Chem. Soc. 105, 7531 (1983).

SECTION II. A STUDY OF THE UNIMOLECULAR DECOMPOSITION OF THE $(C_2H_4)_3^+$ COMPLEX

Abstract

The energetics and dissociation dynamics of the $(C_2H_4)_3^+$ complexes have been studied by photoionization of neutral van der Waals ethylene trimers. The major product channels identified in the unimolecular decomposition of $(C_2H_4)_3^+$ in the total energy [neutral $(C_2H_4)_3$ heat of formation plus excitation energy] range of ~ 260-336 kcal/mol are $C_3H_6^+ + C_3H_6$, $C_3H_7^+ + C_3H_5$, $C_4H_7^+ + C_2H_5$ (or $C_2H_4 + H$), $C_4H_8^+$ [or $(C_2H_4)_2^+$] + C_2H_4, $C_5H_9^+ + CH_3$ and $C_6H_{11}^+ + H$. The fact that these product channels are similar to those observed in the unimolecular decompositions of $(C_3H_6)_2^+$ and $(c\text{-}C_3H_6)_2^+$ is consistent with the interpretation that the $(C_2H_4)_3^+$, $(C_3H_6)_2^+$, and $(c\text{-}C_3H_6)_2^+$ loose complexes rearrange to similar stable $C_6H_{12}^+$ ions prior to fragmenting. The ionization energies (IE) of $(C_2H_4)_3$ and $(C_2H_4)_4$ are determined to be 9.465±0.036 eV (1310±5Å) and 9.287±0.034 eV (1335±5 Å), respectively. Using the known IE's of $(C_2H_4)_n$, n = 2, 3, and 4, and the estimated binding energies of $(C_2H_4)_2 \cdot C_2H_4$ and $(C_2H_4)_3 \cdot C_2H_4$, the bond dissociation energies for $(C_2H_4)_2^+ \cdot C_2H_4$ and $(C_2H_4)_3^+ \cdot C_2H_4$ are deduced to be 9.2±1 and 4.6±1 kcal/mol, respectively.

Introduction

Recently, in a photoionization study of $(C_2H_2)_3$, Ono and Ng[1] have obtained experimental evidence which strongly favors the conclusion that

the loosely bonded $(C_2H_2)_3^+$ ions rearrange to the same common precursors as do other stable $C_6H_6^+$ isomers prior to dissociation. Tzeng et al.[2] have compared the major fragment ions resulting from the unimolecular decompositions of $(C_3H_6)_2^+$ and $(c\text{-}C_3H_6)_2^+$. The $C_3H_7^+$, $C_4H_7^+$, $C_4H_8^+$, and $C_5H_9^+$ are identified to be the major fragment ions from $(C_3H_6)_2^+$ and $(c\text{-}C_3H_6)_2^+$. The variations of the relative abundances for $C_4H_7^+$, $C_4H_8^+$, and $C_5H_9^+$ from $(C_3H_6)_2^+$ and $(c\text{-}C_3H_6)_2^+$ in the total energy {neutral $(C_3H_6)_2$ [or $(c\text{-}C_3H_6)_2$] heat of formation plus excitation energy} range of ~ 230-450 kcal/mol are found to be in qualitative agreement, indicating that $(C_3H_6)_2^+$ and $(c\text{-}C_3H_6)_2^+$ may rearrange to similar $C_6H_{12}^+$ isomers before fragmenting. Since $(C_2H_4)_3$ consists of the same numbers of carbon and hydrogen atoms, it is interesting to compare the major fragments from $(C_2H_4)_3^+$ with those from $(C_3H_6)_2^+$ and $(c\text{-}C_3H_6)_2^+$. If the decomposition of $(C_2H_4)_3^+$ also involves the rearrangement to some stable $C_6H_{12}^+$ isomers, we would expect to find $C_3H_6^+$, $C_3H_7^+$, $C_4H_7^+$, $C_4H_8^+$, and $C_5H_9^+$ to be the prominent fragment ions from $(C_2H_4)_3^+$. This report presents the results of a careful search for product ions resulting from the unimolecular decomposition of $(C_2H_4)_3^+$. A similar photoionization experiment[3] had identified $C_5H_9^+$ and $C_6H_{11}^+$ to be two of the primary fragments of $(C_2H_4)_3^+$.

Experimental

The experimental arrangement and procedures were essentially the same as those described previously.[4,5] Briefly, the apparatus consists of a 3 m near-normal incidence vacuum ultraviolet (VUV) monochromator

(McPherson 2253 M), a supersonic molecular beam production system, a capillary discharge lamp, a VUV light detector, and a quadrupole mass spectrometer for ion detection. The gratings employed in this study are Bausch and Lomb 1200 lines/mm MgF_2 or Os coated aluminum gratings blazed at 1360 Å. The hydrogen many-lined pseudocontinuum or the helium Hopfield continuum was used as the light source.

The ethylene was obtained from Matheson with a quoted purity of $\geq$ 99.5 mol%. The C_2H_4 molecular beam was produced by supersonic expansion through a variable temperature nozzle having a diameter of 120 μm. Most of the data for the ethylene trimers were obtained at a nozzle temperature (T_0) of ~ 210 K and a stagnation pressure (P_0) of 750 Torr. Under these expansion conditions, the intensities of ions containing more than six carbon atoms were found to be negligible, indicating that C_2H_4, $(C_2H_4)_2$, and $(C_2H_4)_3$ were the major constituents of the molecular beam. Since the ethylene beam was sampled in a collisionless environment, the fragment ions observed represent the primary fragments of $C_2H_4^+$, $(C_2H_4)_2^+$, and $(C_2H_4)_3^+$. The photoionization efficiency (PIE) data for $(C_2H_4)_4^+$ were obtained at T_0 ~ 210 K and P_0 ~ 1000 Torr. The correlations of fragment ions to their parent ions are mostly based on photoionization mass spectra obtained at various nozzle expansion conditions. Similar methods were used previously to correlate fragment ions and parent ions observed in the photoionization of $(C_2H_2)_3$[1] and $(C_2H_4)_2$.[6]

PIE spectra were obtained with a wavelength resolution of 1.4 Å (FWHM). Data points were taken at either 0.5 or 1 Å intervals. The

relative standard deviations of the PIE data were less than 10%. Each PIE spectrum was based on at least two scans and prominent structures in the plotted data were reproducible. Wavelength calibrations were achieved by using known atomic resonance lines, or H_2 emission lines when the H_2 pseudocontinuum was used.[7]

Results and Discussion

The relative intensities of the major fragment ions from $(C_2H_4)_3^+$, $(C_2H_4)_2^+$ and $C_2H_4^+$ observed using a photon energy of 10.64 eV (1165 Å) at P_0 ~ 750 Torr and T_0 ~ 210 K are listed in Table I. Minor ions including $C_6H_{10}^+$, $C_5H_{10}^+$, $C_4H_6^+$, $C_3H_4^+$, and $C_2H_2^+$, which have the intensities less than 2% that of $(C_2H_4)_3^+$ have not been listed. The intensity for $C_4H_8^+$ or $(C_2H_4)_2^+$ is arbitrarily normalized to 1.000. Under these experimental conditions, $(C_2H_4)_4^+$ is the only observable ion with more than six carbons. The intensity of $(C_2H_4)_4^+$ is less than 4% that of $(C_2H_4)_3^+$. Attempts were made to further reduce the intensity of $(C_2H_4)_4^+$ by lowering the P_0 and/or rising T_0. We found that these changes also significantly lowered the intensities of $(C_2H_4)_3^+$ and its fragment ions, making it difficult to measure the PIE spectra for the C_5 and C_6 ions. Assuming the intensity of $(C_2H_4)_4^+$ to be a direct measure of $(C_2H_4)_4$ in the ethylene beam, the contributions from fragments of $(C_2H_4)_4^+$ to the C_5 and C_6 ions observed here should be negligibly small.

In a previous photoionization experiment, Ono et al.[7] showed that the $C_4H_8^+$ [and/or $(C_2H_4)_2^+$], $C_4H_7^+$, and $C_3H_5^+$ ion can be produced by the photoionization of $(C_2H_4)_2$ as well as $(C_2H_4)_3$ and higher ethylene clusters. The appearance energies (AE) for the processes

Table I. Relative intensities of major fragment ions from $(C_2H_4)_3^+$ and $(C_2H_4)_2^+$ observed using a photon wavelength of 1165 Å at P_0 ~ 750 Torr and T_0 ~ 210 K

Ions	Relative Intensities[a,b]
$(C_2H_4)_3^+$	0.093
$C_6H_{11}^+$	0.021
$C_5H_9^+$	0.112
$C_4H_8^+$ [or $(C_2H_4)_2^+$]	1.000
$C_4H_7^+$	0.136
$C_3H_7^+$	0.023
$C_3H_6^+$	0.051
$C_3H_5^+$	0.069
$C_2H_4^+$	18.6

[a]No corrections were made to account for transmission factors of these ions through the quadrupole mass spectrometer.

[b]The intensity for $(C_2H_4)_2^+$ or $C_4H_8^+$ is arbitrarily normalized to 1.000.

$$(C_2H_4)_2 + h\nu \longrightarrow (C_2H_4)_2^+ + e^- \quad (1)$$

$$\longrightarrow C_4H_7^+ + H + e^- \quad (2)$$

$$\longrightarrow C_3H_5^+ + CH_3 + e^- \quad (3)$$

were determined to be 9.84±0.04 (1260±5 Å), 10.05±0.04 (1234±5 Å), and 10.20±0.04 eV (1214±5 Å), respectively. The intensities for $C_6H_{11}^+$, $C_5H_9^+$, $C_3H_7^+$, and $C_3H_6^+$ were found to be negligibly small when beam expansion conditions did not favor the formation of ethylene trimers. This finding shows that the $C_6H_{11}^+$, $C_5H_9^+$, $C_3H_7^+$, and $C_3H_6^+$ ions observed here arise mainly from the unimolecular decomposition of $(C_2H_4)_3^+$. The possible reactions which can give rise to these ions are

$$(C_2H_4)_3 \xrightarrow{h\nu} (C_2H_4)_3^+ + e^- \Longleftrightarrow [C_6H_{12}^+]^* + e^-$$

$$\longrightarrow C_6H_{11}^+ + H + e^- \quad (4)$$

$$\longrightarrow C_5H_9^+ + CH_3 + e^- \quad (5)$$

$$\longrightarrow C_4H_8^+ + C_2H_4 + e^- \quad (6)$$

$$\longrightarrow C_4H_7^+ + C_2H_5 + e^- \quad (7)$$

$$\longrightarrow C_4H_7^+ + C_2H_4 + H + e^- \quad (8)$$

$$\longrightarrow C_3H_7^+ + C_3H_5 + e^- \qquad (9)$$

$$\longrightarrow C_3H_6^+ + C_3H_6 + e^- \qquad (10)$$

$$\longrightarrow C_3H_5^+ + C_3H_7 + e^- \qquad (11)$$

$$\longrightarrow C_2H_4^+ + C_4H_8 + e^-. \qquad (12)$$

Due to the overwhelming intensity of $C_2H_4^+$ formed by the direct photoionization of C_2H_4, reaction (12) could not be examined in this study.

The PIE curves obtained for $(C_2H_4)_3^+$, $C_5H_9^+$, $C_3H_6^+$, $C_4H_8^+$, $C_3H_7^+$, $C_4H_7^+$, and $C_6H_{11}^+$, in the region of 950-1325 Å using a wavelength resolution of 1.4 Å (FWHM) at P_0 ~ 750 Torr and T_0 ~ 210 K, are depicted in Figs. 1(a)-1(g). The $C_4H_8^+$ and $C_4H_7^+$ spectra shown in Figs. 1(d) and 1(f) have contributions from both $(C_2H_4)_2$ and $(C_2H_4)_3$. However, at photon energies lower than the AE's of reactions (1) and (2), the $C_4H_8^+$ and $C_4H_7^+$ ions should be solely formed by reactions (6) and (7). The profiles of all the PIE spectra are similar, confirming that these ions are product ions resulting from the photoionization of $(C_2H_4)_3$ and/or $(C_2H_4)_2$. The PIE curve for $C_3H_5^+$, which also has a similar appearance, is not included in Fig. 1.

The PIE curve for $(C_2H_4)_3^+$ in the region of 650-1350 Å can be compared to the PIE spectra for $C_2H_4^+$ and $(C_2H_4)_4^+$ in Figs. 2(a)-2(c). The profiles of these curves are also similar. Since the $(C_2H_4)_3^+$

Figure 1. PIE curves for $(C_2H_4)_3^+$, $C_5H_9^+$, $C_3H_6^+$, $C_4H_8^+$, $C_3H_7^+$, $C_4H_7^+$, and $C_6H_{11}^+$ in the region of 950–1325 Å.

(a) PIE curve for $(C_2H_4)_3^+$ in the region of 950–1320 Å.

(b) PIE curve for $C_5H_9^+$ in the region of 950–1310 Å.

(c) PIE curve for $C_3H_6^+$ in the region of 950–1300 Å.

(d) PIE curve for $C_4H_8^+$ in the region of 950–1310 Å.

(e) PIE curve for $C_3H_7^+$ in the region of 950–1300 Å.

(f) PIE curve for $C_4H_7^+$ in the region of 950–1310 Å.

(g) PIE curve for $C_6H_{11}^+$ in the region of 950–1325 Å.

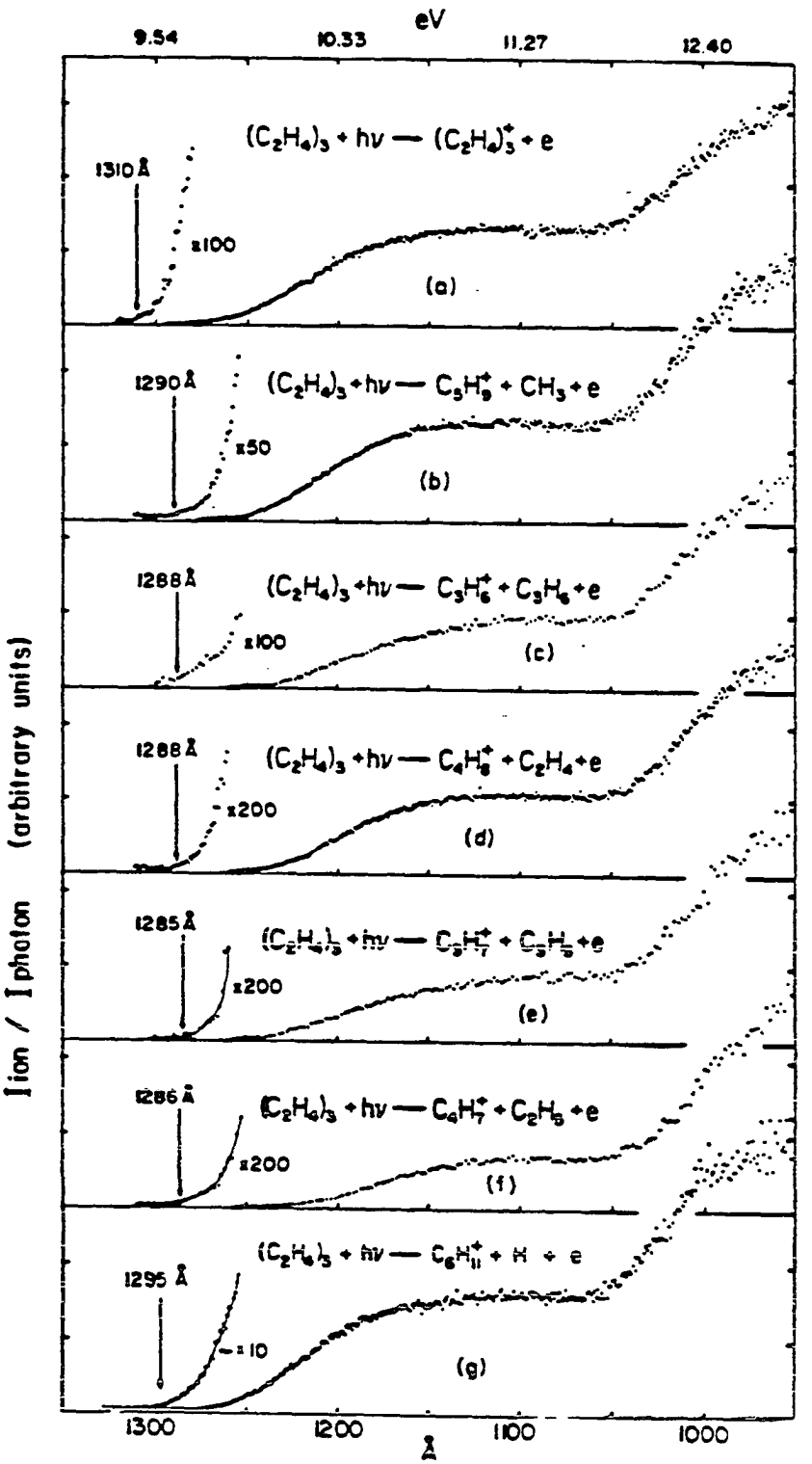
eV
9.54
10.33
11.27
12.40
$(C_2H_4)_3 + h\nu \rightarrow (C_2H_4)_3^+ + e$
1310 Å
x100
(a)
1290 Å
$(C_2H_4)_3 + h\nu \rightarrow C_5H_9^+ + CH_3 + e$
x50
(b)
1288 Å
$(C_2H_4)_3 + h\nu \rightarrow C_3H_5^+ + C_3H_6 + e$
x100
(c)
1288 Å
$(C_2H_4)_3 + h\nu \rightarrow C_4H_8^+ + C_2H_4 + e$
x200
(d)
1285 Å
$(C_2H_4)_3 + h\nu \rightarrow C_5H_7^+ + C_3H_5 + e$
x200
(e)
1286 Å
$(C_2H_4)_3 + h\nu \rightarrow C_4H_7^+ + C_2H_5 + e$
x200
(f)
$(C_2H_4)_3 + h\nu \rightarrow C_6H_{11}^+ + H + e$
1295 Å
x10
(g)
1300
1200
1100
1000
Å
I ion / I photon (arbitrary units)

Figure 2. PIE curves for $C_2H_4^+$, $(C_2H_4)_3^+$, and $(C_2H_4)_4^+$ in the region of 640–1350 Å.

(a) PIE curve for $C_2H_4^+$ in the region of 640–1185 Å.

(b) PIE curve for $(C_2H_4)_3^+$ in the region of 640–1320 Å.

(c) PIE curve for $(C_2H_4)_4^+$ in the region of 640–1350 Å.

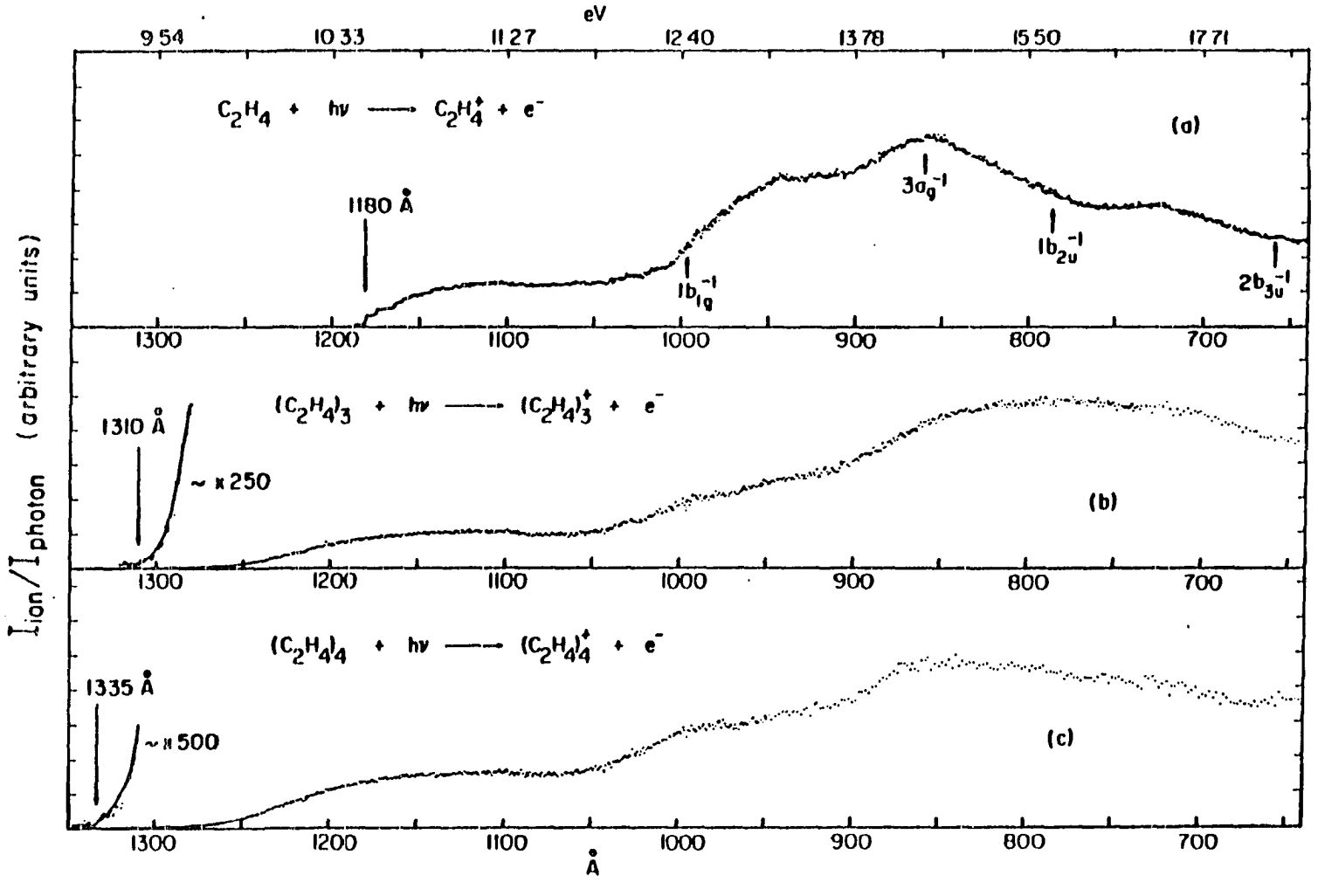
eV
9.54
10.33
11.27
12.40
13.78
15.50
17.71
$C_2H_4 + h\nu \longrightarrow C_2H_4^+ + e^-$
(a)
1180 Å
$1b_{1g}^{-1}$
$3a_g^{-1}$
$1b_{2u}^{-1}$
$2b_{3u}^{-1}$
1300
1200
1100
1000
900
800
700
$(C_2H_4)_3 + h\nu \longrightarrow (C_2H_4)_3^+ + e^-$
1310 Å
~ x 250
(b)
$(C_2H_4)_4 + h\nu \longrightarrow (C_2H_4)_4^+ + e^-$
1335 Å
~ x 500
(c)
Å
I_{ion}/I_{photon} (arbitrary units)

spectrum was measured at beam expansion conditions which minimize the formation of higher ethylene clusters, the threshold of 9.465±0.036 eV (1310±5 Å) determined in Fig. 2(b) is the ionization energy (IE) of $(C_2H_4)_3$. The PIE curve for $(C_2H_4)_4^+$ was obtained at P_0 ~ 1000 Torr and T_0 ~ 210 K. The intensity of $(C_2H_4)_4^+$ under these expansion conditions was approximately 35% that of $(C_2H_4)_3^+$. The IE of $(C_2H_4)_4$ was determined to be 9.287±0.034 eV (1335±5 Å). This value was found to be essentially unaffected by the beam expansion conditions and thus the distribution in concentration of higher ethylene clusters. The binding energies for $(C_2H_4)_2 \cdot C_2H_4$ and $(C_2H_4)_3 \cdot C_2H_4$ are not known. Here we assume the binding energies for $(C_2H_4)_2 \cdot C_2H_4$ and $(C_2H_4)_3 \cdot C_2H_4$ to be the same as that for $C_2H_4 \cdot C_2H_4$ (0.42±0.03 kcal/mol).[8] Using this value and the IE's of $(C_2H_4)_2$,[7] $(C_2H_4)_3$, and $(C_2H_4)_4$, the dissociation energies for $(C_2H_4)_2^+ \cdot C_2H_4$ and $(C_2H_4)_3^+ \cdot C_2H_4$ are calculated to be 9.2±1 and 4.6±1 kcal/mol, respectively. These values are significantly lower than the dissociation energy for $C_2H_4^+ \cdot C_2H_4$ (15.8±1 kcal/mol).

In order to rationalize the observation of this study, a pseudo-reaction-coordinate diagram (Fig. 3), illustrating the dissociation pathways and stabilities (or heats of formation) of intermediates and products, was constructed with the use of thermochemical data summarized in Table II.[2,8-22] When an ion or a neutral has more than one possible structure, the heat of formation of the most stable structure was used in calculating the stability of a product channel. The stabilities for $(C_3H_6)_2^+$ and $(c\text{-}C_3H_6)_2^+$ determined in a recent study are also shown in the figure. In the construction of the pseudo-reaction-coordinate

Figure 3. Pseudo-reaction-coordinate diagram for the decompositions of $(C_2H_4)_3^+$, $(C_3H_6)_2^+$, and $(c\text{-}C_3H_6)_2^+$.

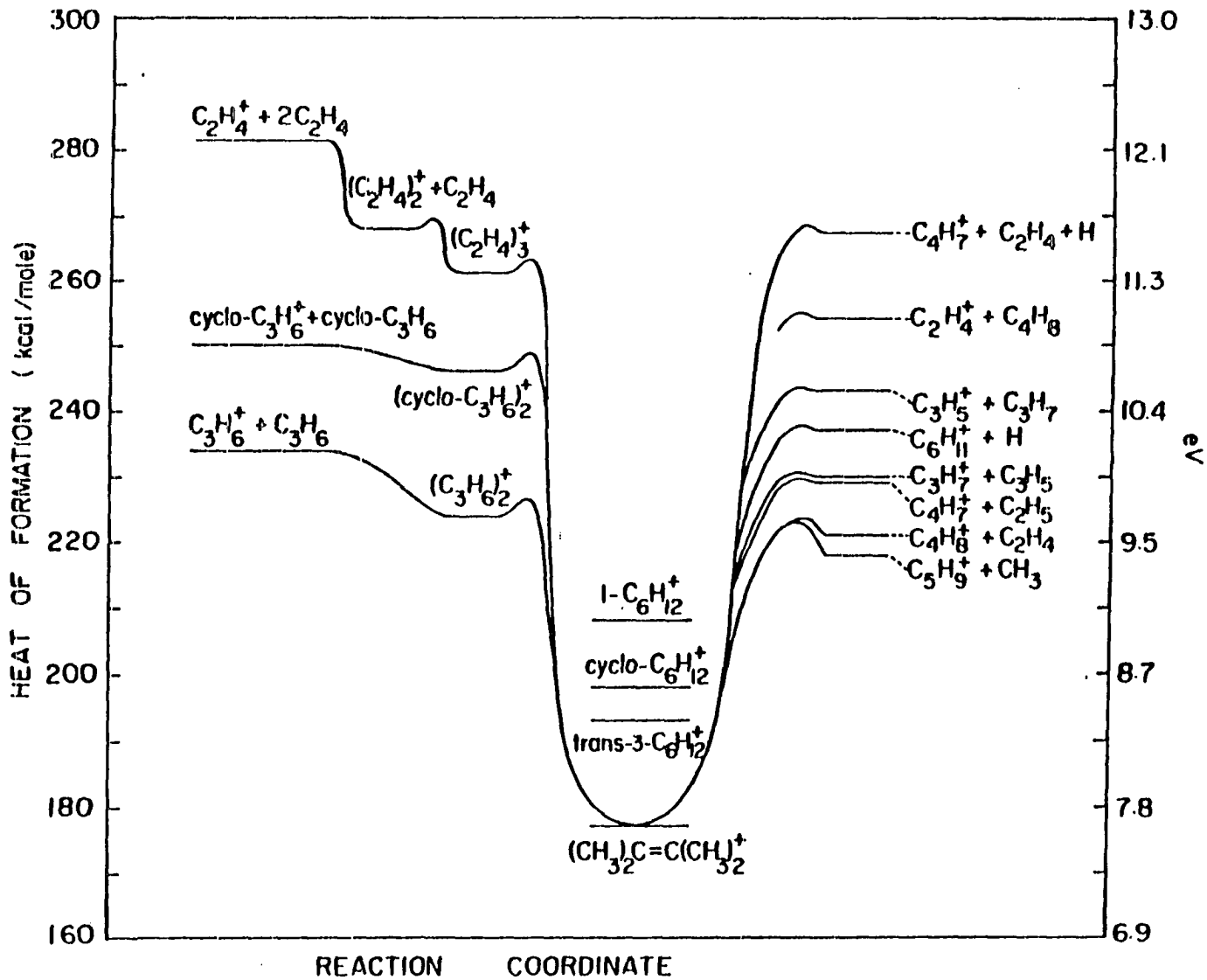
300
280
260
240
220
200
180
160
HEAT OF FORMATION (kcal/mole)
13.0
12.1
11.3
10.4
9.5
8.7
7.8
6.9
eV
$C_2H_4^+ + 2C_2H_4$
$(C_2H_4)_2^+ + C_2H_4$
$(C_2H_4)_3^+$
cyclo-$C_3H_6^+$+cyclo-C_3H_6
(cyclo-$C_3H_6)_2^+$
$C_3H_6^+ + C_3H_6$
$(C_3H_6)_2^+$
1-$C_6H_{12}^+$
cyclo-$C_6H_{12}^+$
trans-3-$C_6H_{12}^+$
$(CH_3)_2C=C(CH_3)_2^+$
$C_4H_7^+ + C_2H_4 + H$
$C_2H_4^+ + C_4H_8$
$C_3H_5^+ + C_3H_7$
$C_6H_{11}^+ + H$
$C_3H_7^+ + C_3H_5$
$C_4H_7^+ + C_2H_5$
$C_4H_8^+ + C_2H_4$
$C_5H_9^+ + CH_3$
REACTION COORDINATE

Table II. 298 K heats of formation in kcal/mol of neutrals and ions[a]

Compounds	Neutrals	Ions
$(C_2H_4)_4$	48.9±0.15 (8,9)	263.1±0.9[b]
$(C_2H_4)_3$	35.34±0.15(8,9)	253.6±0.9[b]
$(C_3H_6)_2$	9.16 (9,10)	224.3 (2)
$(c\text{-}C_3H_6)_2$	24.9 (9)	246.5[c] (2)
$1\text{-}C_6H_{12}$		208 (11)
$trans\text{-}3\text{-}C_6H_{12}$		193 (11)
Cyclohexane		~198 (11)
$(CH_3)_2C = C(CH_3)_2$		177 (11)
C_6H_{11}(cyclohexyl)		185 (12)
1,3-dimethylallyl		183.5 (13)
C_5H_9(cyclopentyl)		197 (14)
$(C_2H_4)_2$	24.66±0.1 (8,9)	255.5±0.9 (7)
C_4H_8(cyclobutane)		238 (15)
Methylcyclopropane		239 (15)
$1\text{-}C_4H_8$		221 (12)
$Cis\text{-}2\text{-}C_4H_8$		209 (12)
$Trans\text{-}2\text{-}C_4H_8$		208 (12)
$Iso\text{-}C_4H_8$		209 (12)

[a]The numbers in the parentheses are the references.

[b]This work.

[c]This value is calculated by assuming the binding energy for $(c\text{-}C_3H_6)_2$ to be the same as for $(C_3H_6)_2$.

Table II. (continued)

Compounds	Neutrals	Ions
1-methylallyl		203.1±1.4 (16)
2-methylallyl		212±1.6 (16)
Cyclobutyl		225.1±1.1 (16)
Allylcarbinyl		231.0±3 (16)
C_3H_7	17.6 (17)	~207 (11,12)
n-C_3H_7	22.6±1.1 (18)	
	21.1±1 (19)	
i-C_3H_7	20.0±1.1 (18)	~191 (11,12)
	18.2±1 (19)	
C_3H_6	4.88 (9)	229.4 (2)
c-C_3H_6	12.74 (9)	237 (2)
C_3H_5	38.4±1.7 (20)	226±2 (15)
		224.5±1.0 (20)
		225.5±1.1 (21)
		226±1 (22)
C_2H_5	25.7 (17)	
	28.3±1.1 (18)	
	25.9±1 (19)	
C_2H_4	12.54±0.07 (9)	
CH_3	34.8±0.2 (9)	
	35.1±0.5 (18,19)	
H	52.100±0.001 (9)	

diagram, we assumed that the loose $(C_2H_4)_3^+$, $(C_3H_6)_2^+$, and $(c\text{-}C_3H_6)_2^+$ complexes rearrange to stable $C_6H_{12}^+$ isomers before fragmenting. Among the stable $C_6H_{12}^+$ structures, $(CH_3)_2C{=}C(CH_3)_2^+$ is the most stable isomer while $1\text{-}C_6H_{12}^+$ is the least stable isomer. As shown in Fig. 3, the stabilities of products of reactions (4), (5), (6), (7), (9), (10), (11), and (12) are all significantly lower than the stability of $(C_2H_4)_3^+$. The exit potential energy barrier between stable $C_6H_{12}^+$ isomers and the products of these reactions cannot be probed unambiguously by the AE measurements of various fragment ions.[7]

Within the error limits of ± 5 Å for the AE measurements, the AE's for $C_5H_9^+$, $C_3H_6^+$, $C_4H_8^+$, $C_3H_7^+$, $C_4H_7^+$, and $C_6H_{11}^+$ are essentially identical and have a value of 9.61±0.04 eV (1290±5 Å). Similar to the observation in the AE measurement for $(C_2H_4)_4^+$, the AEs for these fragment ions as well as that for $(C_2H_4)_3^+$ are unaffected by increasing P_0 and/or lowering T_0. The AEs for these ions obtained at P_0 ~ 1000 Torr and T_0 ~ 210 K differ less than 5 Å in comparison with values shown in Figs. 1(a)-1(f). The difference of ~ 0.15 eV between the AEs of these fragment ions and the IE of $(C_2H_4)_3$ is interpreted to be the energy barrier for the rearrangement from $(C_2H_4)_3^+$ to $C_6H_{12}^+$.

If the fragmentation of $(C_2H_4)_4^+$ involves the prior rearrangement of the loose complex to form a stable $C_8H_{16}^+$ structure, the dissociation process such as

$$(C_2H_4)_4 \xrightarrow{h\nu} (C_2H_4)_4^+ + e^- \rightleftharpoons [C_8H_{16}^+]^* + e^-$$

$$\longrightarrow C_6H_{12}^+ + C_2H_4 + e^- \qquad (13)$$

will have an AE lower than that of the process

$$(C_2H_4)_3 \xrightarrow{h\nu} (C_2H_4)_3^+ + e^-. \qquad (14)$$

This conclusion is simply based on the fact that the heat of formation of $C_6H_{12}^+$ is substantially lower than that for $(C_2H_4)_3^+$. The fragmentation process

$$(C_2H_4)_4 + h\nu \longrightarrow (C_2H_4)_3^+ + C_2H_4 + e^- \qquad (15)$$

is expected to have an AE higher than the IE of $(C_2H_4)_3$. The observation that the lowering of the AEs of $(C_2H_4)_3^+$ and other fragment ions from $(C_2H_4)_3$ is small at high concentrations of $(C_2H_4)_4$ and higher ethylene clusters in the beam can be rationalized on the basis that the rearrangements of $(C_2H_4)_4^+$ and higher ethylene cluster ions to the corresponding stable ion structures are inefficient. As the size of the loose cluster ion increases, the interactions between moieties of the cluster ion should be less effective. This interpretation seems reasonable.

Another possible explanation for the negligible shifts observed in the AE's for $(C_2H_4)_3^+$ and fragment ions from $(C_2H_4)_3$ at high concentrations of $(C_2H_4)_4$ and higher ethylene clusters in the beam is due to the kinetic shift effects.[23-25] It has been demonstrated that the dissociation lifetimes for large polyatomic molecules can prevent

the measurement of the true AE of a dissociation channel to be measured.[26-28] It is likely that the measured AE's of reaction (13) and similar fragmentation processes from $(C_2H_4)_4^+$ and higher ethylene cluster ions are limited by the kinetic shift effects. Due to the tailing ion intensities near thresholds and the kinetic shift effects, the AE's for fragment ions measured in this experiment should be considered as upper bounds. We believe the value of 9.72 (1276 Å) for the AE of reaction (11) reported previously is an upper limit. The very gradual rise in PIE of $C_3H_5^+$ near the threshold has made the measurement of the true AE of $C_3H_5^+$ difficult.

The ionization photon of 1165 Å used to measure the relative fragment ion intensities (Table I) corresponds to a value of 280 kcal/mol (12.18 eV) in the total energy scale. The previous photoionization study[2] of $(C_3H_6)_2$ and $(c\text{-}C_3H_6)_2$ shows that the relative intensities of $C_4H_8^+$, $C_5H_9^+$, and $C_4H_7^+$ from $(C_3H_6)_2^+$ and $(c\text{-}C_3H_6)_2^+$ are in the order $I(C_4H_8^+) \gg I(C_5H_9^+) > I(C_4H_7^+)$. Here $I(C_4H_8^+)$, $I(C_5H_9^+)$, and $I(C_4H_7^+)$ are the intensities of $C_4H_8^+$, $C_5H_9^+$, and $C_4H_7^+$, respectively. The relative intensities of these ions listed in Table I are in the order $I(C_4H_8^+) \gg I(C_4H_7^+) \gtrsim I(C_5H_9^+)$. As mentioned above, the $C_4H_7^+$ ion observed in this study can be formed by the fragmentations of $(C_2H_4)_2^+$ and $(C_2H_4)_3^+$. After correcting for the contribution from $(C_2H_4)_2^+$, the intensity of $C_4H_7^+$ arising from $(C_2H_4)_3^+$ is expected to be smaller than that of $C_5H_9^+$.

Because of the extremely strong $C_3H_6^+$ and $c\text{-}C_3H_6^+$ background signals produced by the direct photoionization of C_3H_6 and $c\text{-}C_3H_6$, the

formation of $C_3H_6^+ + C_3H_6$ channel from $(C_3H_6)_2^+$ and $(c\text{-}C_3H_6)_2^+$ cannot be identified in the photoionization study of $(C_3H_6)_2$ and $(c\text{-}C_3H_6)_2$.[2] The identification of $C_3H_6^+ + C_3H_6$ as a major fragmentation channel from $(C_2H_4)_3^+$ is consistent with the dissociation mechanism shown in reaction (10).

In summary, prominent fragment ions, $C_3H_7^+$, $C_4H_7^+$, $C_4H_8^+$, and $C_5H_9^+$ observed in the unimolecular decompositions of $(C_3H_6)_2^+$ and $(c\text{-}C_3H_6)_2^+$ are identified as the major product ions resulting from the decomposition of $(C_2H_4)_3^+$. This observation is in accord with the interpretation that $(C_3H_6)_2^+$, $(c\text{-}C_3H_6)_2^+$, and $(C_2H_4)_3^+$ rearrange to some common stable $C_6H_{12}^+$ isomers prior to the formation of these fragment ions. The fact that the $C_6H_{11}^+$ ion is found to be a fragment from $(C_2H_4)_3^+$ and $(C\text{-}C_3H_6)_2^+$ but not $(C_3H_6)_2^{+2}$ indicates that the distributions of stable $C_6H_{12}^+$ isomers involved in the decompositions of $(C_2H_4)_3^+$, $(C_3H_6)_2^+$, and $(c\text{-}C_3H_6)_2^+$ are different.

References

1. Y. Ono and C. Y. Ng, J. Am. Chem. Soc. 104, 4752 (1982).
2. W.-B. Tzeng, Y. Ono, S. H. Linn, and C. Y. Ng, J. Chem. Phys. 83, 2803 (1985).
3. S. T. Ceyer, P. W. Tiedemann, C. Y. Ng, B. H. Mahan, and Y. T. Lee, J. Chem. Phys. 70, 2138 (1979).
4. Y. Ono, S. H. Linn, H. F. Prest, M. E. Gress, and C. Y. Ng, J. Chem. Phys. 73, 2523 (1980).
5. Y. Ono, S. H. Linn, H. F. Prest, C. Y. Ng, and E. Meisher, J. Chem. Phys. 73, 4855 (1980).
6. Y. Ono, S. H. Linn, W.-B. Tzeng, and C. Y. Ng, J. Chem. Phys. 80, 1482 (1984).

7. K. E. Schubert and R. D. Hudson, Rep. No. ATN-64(9233)-2, Aerospace Corp., Los Angeles, 1963.

8. J. O. Hirshfelder, C. F. Curtiss, and R. B. Bird, Molecular Theory of Gases and Liquids (John Wiley & Sons, New York, 1954), p. 1112. Depending on the geometry of the ethylene dimer, the previous theoretical calculations yield values for the well depth for the $C_2H_4 + C_2H_4$ interaction in the range of ~ 0.2-12.1 kcal/mol (see Ref. 7 and references therein). The value of 0.42±0.03 kcal/mol used here and in Ref. 7 is the average value for the dissociation energy of $(C_2H_4)_2$ derived from second virial coefficient and viscosity measurements.

9. D. R. Stull, E. F. Westrum, Jr., and G. C. Sinke, The Chemical Thermodynamics of Organic Compounds (John Wiley & Sons, New York, 1969).

10. L. W. Flynn and G. Thodos, A. I. Ch. E. Journal 8, 362 (1962).

11. H. M. Rosenstock, K. Draxl, B. W. Steiner, J. T. Herron, J. Phys. Chem. Ref. Data 6, Suppl. 1 (1977).

12. J. L. Franklin, J. G. Dillard, H. M. Rosenstock, J. T. Herron, K. Draxl, and F. H. Field, Ionization Potentials, Appearance Potentials, and Heats of Formation of Gaseous Positive Ions, NSRDS-NBS 26 (U. S. GPO, Washington, DC., 1969).

13. D. H. Aue and M. T. Bowers, in Gas Phase Ion Chemistry, edited by M. T. Bowers (Academic Press, New York, 1979), Vol. 2, p. 1.

14. F. P. Lossing and J. C. Traeger, J. Am. Chem. Soc. 97, 1579 (1975).

15. F. P. Lossing, Can. J. Chem. 50, 3973 (1972).

16. J. C. Schultz, F. A. Houle, and J. L. Beauchamp, J. Am. Chem. Soc. 106, 7336 (1984).

17. S. W. Benson and H. E. O'Neal, Kinetic Data on Gas Phase Unimolecular Reactions, NSRDS-NBS 21 (U. S. GPO, Washington, D.C., 1970).

18. W. v. E. Doering, Proc. Natl. Acad. Sci. USA 78, 5279 (1981).

19. D. F. McMillen and D. M. Golden, Annu. Rev. Phys. Chem. 33, 493 (1982).

20. S. E. Buttrill, Jr., A. D. William, and P. LeBreton, J. Chem. Phys. 62, 1586 (1975).

21. F. A. Houle and J. L. Beauchamp, J. Am. Chem. Soc. 100, 3290 (1978).

22. J. C. Traeger, Int. J. Mass Spectrom. Ion Phys. 32, 309 (1980).

23. L. Friedman, F. A. Long, and M. Wolfsberg, J. Chem. Phys. 26, 714 (1957).

24. L. Friedman, F. A. Long, and M. Wolfsberg, J. Chem. Phys. 27, 613 (1957).

25. W. A. Chupka, J. Chem. Phys. 30, 191 (1959). 26. M. L. Gross, Org. Mass Spectrom. 6, 827 (1972).

27. C. Lifshitz, A. M. Peers, M. Weiss, and M. J. Weiss, Adv. Mass Spectrom. 6, 871 (1974).

28. S. M. Gordon and N. W. Reid, Int. J. Mass Spectrom. Ion Phys. 18, 379 (1975).

SECTION III. A STUDY OF THE UNIMOLECULAR DECOMPOSITIONS OF THE $(C_3H_6)_2^+$ and $(c\text{-}C_3H_6)_2^+$ COMPLEXES

Abstract

The major product channels identifies in the unimolecular decompositions of $C_3H_6^+ \cdot C_3H_6$ and $c\text{-}C_3H_6^+ \cdot c\text{-}C_3H_6$ in the total energy [neutral $(C_3H_6)_2$ or $(c\text{-}C_3H_6)_2$ heat of formation plus excitation energy] range of ~ 230-450 kcal/mol are $C_3H_7^+ + C_3H_5$, $C_4H_7^+ + C_2H_5$, $C_4H_8^+ + C_2H_4$, and $C_5H_9^+ + CH_3$. The measured appearance energy for $C_4H_7^+$ (9.54±0.04 eV) from $(C_3H_6)_2$ is equal to the thermochemical threshold for the formation of $C_4H_7^+ + C_2H_5$ from $(C_3H_6)_2$, indicating that the exit potential energy barrier for the ion-molecule reaction $C_3H_6^+ + C_3H_6 \longrightarrow C_4H_7^+ + C_2H_5$ is negligible. There is evidence that the formations of $C_4H_7^+ + C_2H_4 + H$ from $(C_3H_6)_2^+$ and $(c\text{-}C_3H_6)_2^+$ also proceed with high probabilities when they energetically allowed. The variations of the relative abundances for $C_4H_7^+$, $C_4H_8^+$, and $C_5H_9^+$ from $(C_3H_6)_2^+$ and $(c\text{-}C_3H_6)_2^+$ as a function of ionizing photon energy are in qualitative agreement, suggesting that $(C_3H_6)_2^+$ and $(c\text{-}C_3H_6)_2^+$ rearrange to similar $C_6H_{12}^+$ isomers prior to fragmentation. The fact that $C_6H_{11}^+$ is found to be a primary ion from the unimolecular decomposition of $(c\text{-}C_3H_6)_2^+$ but not $(C_3H_6)_2^+$ supports the conclusion that the distribution of $C_6H_{12}^+$ collision complexes involved in the $C_3H_6^+ + C_3H_6$ reactions is different from that in the cyclopropane ion-molecule reactions. Using the ionization energies (IE) of $(C_3H_6)_2$ (9.33±0.04 eV) and $(c\text{-}C_3H_6)_2$ (9.61±0.04 eV) determined in this study, the calculation of the bond

dissociation energies for $C_3H_6^+ \cdot C_3H_6$ and $c\text{-}C_3H_6^+ \cdot c\text{-}C_3H_6$ gives 0.43 and 0.14 eV, respectively. The measured IE of C_3H_6 is 9.738±0.003 eV and that of $c\text{-}C_3H_6$ is 9.721±0.011 eV.

Introduction

The propylene ion-molecule reactions

$$C_3H_6^+ + C_3H_6 \rightleftharpoons [C_6H_{12}^+]^* \longrightarrow C_3H_7^+ + C_3H_5 \quad (1)$$

$$\longrightarrow C_4H_7^+ + C_2H_5 \quad (2)$$

$$\longrightarrow C_4H_8^+ + C_2H_4 \quad (3)$$

$$\longrightarrow C_5H_9^+ + CH_3 \quad (4)$$

have been subjected to detailed scrutiny by mass spectrometry in the past three decades.[1-18] The common conclusion from these studies is that the primary reactions proceed through long-lived $[C_6H_{12}^+]^*$ complex ions. Due to the long lifetimes of the collisional complexes, the bimolecular formation of stable $C_6H_{12}^+$ in propylene has been observed.[14,18] Fragmentation patterns of $C_6H_{12}^+$ prepared by electron ionization of some stable H_6H_{12} isomers have been found to be in good correlation with the relative intensities of $C_4H_7^+$, $C_4H_8^+$, and $C_5H_9^+$ observed in the $C_3H_6^+ + C_3H_6$ reactions.[15] This observation suggests that the branching ratios for $C_4H_7^+$, $C_4H_8^+$, and $C_5H_9^+$ produced by

reactions (2), (3), and (4) are governed mainly by the unimolecular decomposition of the $[C_6H_{12}^+]^*$ collisional complexes.

The internal energy effect on the propylene ion-molecule reactions has been examined by preparing the $C_3H_6^+$ ions by photoionization of C_3H_6 at 10 and 11.7 eV. The observed reduction in the total rate coefficient with increasing internal energy of $C_3H_6^+$ can be partly attributed to a decrease in the lifetime of the collisional complex. Previous experiments[13,14,18] have shown that when the kinetic or internal energies of $C_3H_6^+$ are increased, the fractional yields of $C_3H_7^+$ and $C_4H_7^+$ increase while $C_4H_8^+$ and $C_5H_9^+$ decrease. The tandem mass spectrometric experiment of Abramson and Futrell[16] indicates that the production of $C_3H_7^+$ also proceeds through a long range process which is chemically distinct from those responsible for the formation of $C_4H_7^+$, $C_4H_8^+$, $C_5H_9^+$, and $C_6H_{12}^+$. The long range process is believed to be favored when the reactant $C_3H_6^+$ ion is produced in high vibrational states or under conditions of high kinetic energy.

Several mass spectrometric studies of the c-$C_3H_6^+$ + c-C_3H_6 reactions[9,11,17,18] have been made to compare with the results of reactions (1)-(4). The internal and kinetic energy effects on the formation of $C_3H_7^+$, $C_4H_7^+$, $C_4H_8^+$, and $C_5H_9^+$ are found to be similar to those observed in the propylene ion-molecule reactions.

In this report we present the results and an analysis of the unimolecular decompositions of $(C_3H_6)_2^+$ and $(c\text{-}C_3H_6)_2^+$ which had been prepared by photoionization of $(C_3H_6)_2$ and $(c\text{-}C_3H_6)_2$ formed in supersonic beams,

$$(C_3H_6)_2 \xrightarrow{h\nu} (C_3H_6)_2^+ + e^- \longrightarrow [C_6H_{12}^+]^* + e^-$$

$$\longrightarrow C_4H_7^+ + C_2H_5 + e^- \quad (5)$$

$$\longrightarrow C_4H_7^+ + C_2H_4 + H + e^- \quad (6)$$

$$\longrightarrow C_4H_8^+ + C_2H_4 + e^- \quad (7)$$

$$\longrightarrow C_5H_9^+ + CH_3 + e^-, \quad (8)$$

$$(c\text{-}C_3H_6)_2 \xrightarrow{h\nu} (c\text{-}C_3H_6)_2^+ + e^- \longrightarrow [C_6H_{12}^+]^* + e^-$$

$$\longrightarrow C_4H_7^+ + C_2H_5 + e^- \quad (9)$$

$$\longrightarrow C_4H_7^+ + C_2H_4 + H + e^- \quad (10)$$

$$\longrightarrow C_4H_8^+ + C_2H_4 + e^- \quad (11)$$

$$\longrightarrow C_5H_9^+ + CH_3 + e^-. \quad (12)$$

Since the loose $(C_3H_6)_2^+$ and $(c\text{-}C_3H_6)_2^+$ complexes are the precursors of stable $[C_6H_{12}^+]^*$ complexes, the comparison of the unimolecular fragmentation of $(C_3H_6)_2^+$ and $(c\text{-}C_3H_6)_2^+$ in this study provides additional insight into the complex mechanisms of the $C_3H_6^+ + C_3H_6$ and $c\text{-}C_3H_6^+ + c\text{-}C_3H_6$ reactions which cannot be obtained by other means.

Similar studies on the unimolecular decompositions of $(C_2H_4)_2^+$,[19,20] $(C_2H_2)_2^+$,[21] and $(C_2H_2)_3^+$[22] have been reported. Higher resolution photoionization efficiency (PIE) curves for $C_3H_6^+$ and c-$C_3H_6^+$ near the thresholds are also examined.

Experimental

The experimental arrangement and procedures were essentially the same as those described previously.[23,24] Briefly, the apparatus consists of a 3 m near-normal incidence vacuum ultraviolet (VUV) monochromator (McPherson 2253 M), a supersonic molecular beam production system, a capillary discharge lamp, a VUV light detector, and a quadrupole mass spectrometer for ion detection. The gratings employed in this study are Bausch and Lomb 1200 lines/mm MgF_2 or Os coated aluminum gratings blazed at 1360 Å. The hydrogen many-lined pseudocontinuum, or the argon continuum, or the helium Hopfield continuum was used as the light source, depending on the wavelength region to be studied.

The propylene and cyclopropane were obtained from Matheson with quoted purities of $\geq$ 99.6% and $\geq$ 99%, respectively, and were used without further purification. The C_3H_6 or c-C_3H_6 molecular beam was produced by supersonic expansion of pure C_3H_6 or c-C_3H_6 through a variable temperature nozzle having a diameter of 120 μm. Most of the data for propylene and cyclopropane dimers were obtained at a nozzle temperature (T_0) of ~ 250 K and a stagnation pressure (P_0) of ~ 500 Torr. In a typical experiment, the fluctuation in the nozzle

temperature was less than ± 3 K as monitored with thermocouples. The PIE data for $C_3H_6^+$ and $c\text{-}C_3H_6^+$ were obtained at room temperature (T_0 ~ 298 K) and P_0 ~ 200 Torr. Under these expansion conditions, the intensities of ions containing more than six carbon atoms were found to be negligible, indicating that the C_3H_6 ($c\text{-}C_3H_6$) and $(C_3H_6)_2$ [$(c\text{-}C_3H_6)_2$] were the major constituents of the molecular beam. Since the propylene and cyclopropane beams were sampled in a collisionless environment, the observed fragment ions are the primary fragments of $C_3H_6^+$($c\text{-}C_3H_6^+$) and $(C_3H_6)_2^+$[$(c\text{-}C_3H_6)_2^+$].

With the exception of the high resolution PIE spectrum for $C_3H_6^+$ near the ionization threshold, which was measured using a wavelength resolution of 0.14 Å (FWHM), all other PIE spectra were obtained with a wavelength resolution of 1.4 Å (FWHM). Data points were taken at 0.05 Å intervals for the high resolution experiment. The other low resolution PIE data were accumulated at either 0.5 or 1 Å intervals except for the PIE data in the region of ~ 650-1150 Å for $C_4H_7^+$ from $(c\text{-}C_3H_6)_2$, which were taken at 5 Å intervals. The relative standard deviations of the PIE data were less than 10%. Each PIE spectrum was based on at least two scans, and prominent structures in the plotted data were reproducible. Wavelength calibrations were achieved by using known atomic resonance lines or H_2 emission lines[25] when the H_2 pseudocontinuum was used.

Results and Discussion

Figure 1 shows the high resolution PIE spectrum for $C_3H_6^+$ in the region of 1250-1276 Å. This spectrum resembles closely that for C_2H_4[20] obtained with the same wavelength resolution. The ionization of C_3H_6 to form $C_3H_6^+$ in the ground $\tilde{X}^2A''$ state results from the removal of an electron from the C=C π orbital. Based on arguments similar to those used in the assignment of the PIE spectrum for $C_2H_4^+$, we take the midpoint of the first rapidly rising step to be the IE for the $\tilde{X}^2A''$ state of $C_3H_6^+$. A value of 9.738±0.003 eV (1273.2±0.4 Å) determined here is in good agreement with values for the IE of C_3H_6 deduced previously by photoionization,[26-34] photoelectron spectroscopy,[35-38] and absorption studies.[32,39,40] The decrease in this IE by 0.77 eV with respect to that of C_2H_4 is attributable to the combined resonance and inductive effects through interactions between the C=C π orbital and the methyl group orbitals in C_3H_6.[38]

The C=C stretching (ν_6), C=C twisting or torsional (ν_{20}), and C=C-C bending (ν_{14}) modes of $C_3H_6^+$ can be excited upon the removal of an electron from the C=C π orbital of C_3H_6. The ν_6, ν_{20}, and ν_{14} modes observed in C_3H_6 are 1647, 578, and 417 cm^{-1}, respectively.[41,42] In the photoelectron study of Katrib and Rabalais,[38] two progressions were found in the first photoelectron band of C_3H_6. The strong progression having an average spacing of 1340 cm^{-1} was assigned to the excitation of the ν_6 mode, while the weak progression with a spacing of ~ 600 cm^{-1} was assigned to the ν_{14} mode of $C_3H_6^+$. The second and third steps observed in Fig. 1 are 472±25 and 1260±32 cm^{-1} above the IE for $C_3H_6^+(\tilde{X}^2A'')$.

Figure 1. PIE curve for $C_3H_6^+$ in the region of 1250-1276 Å obtained using the argon continuum as the light source [wavelength resolution = 0.14 Å (FWHM), P_0 ~ 200 Torr, T_0 ~ 298 K].

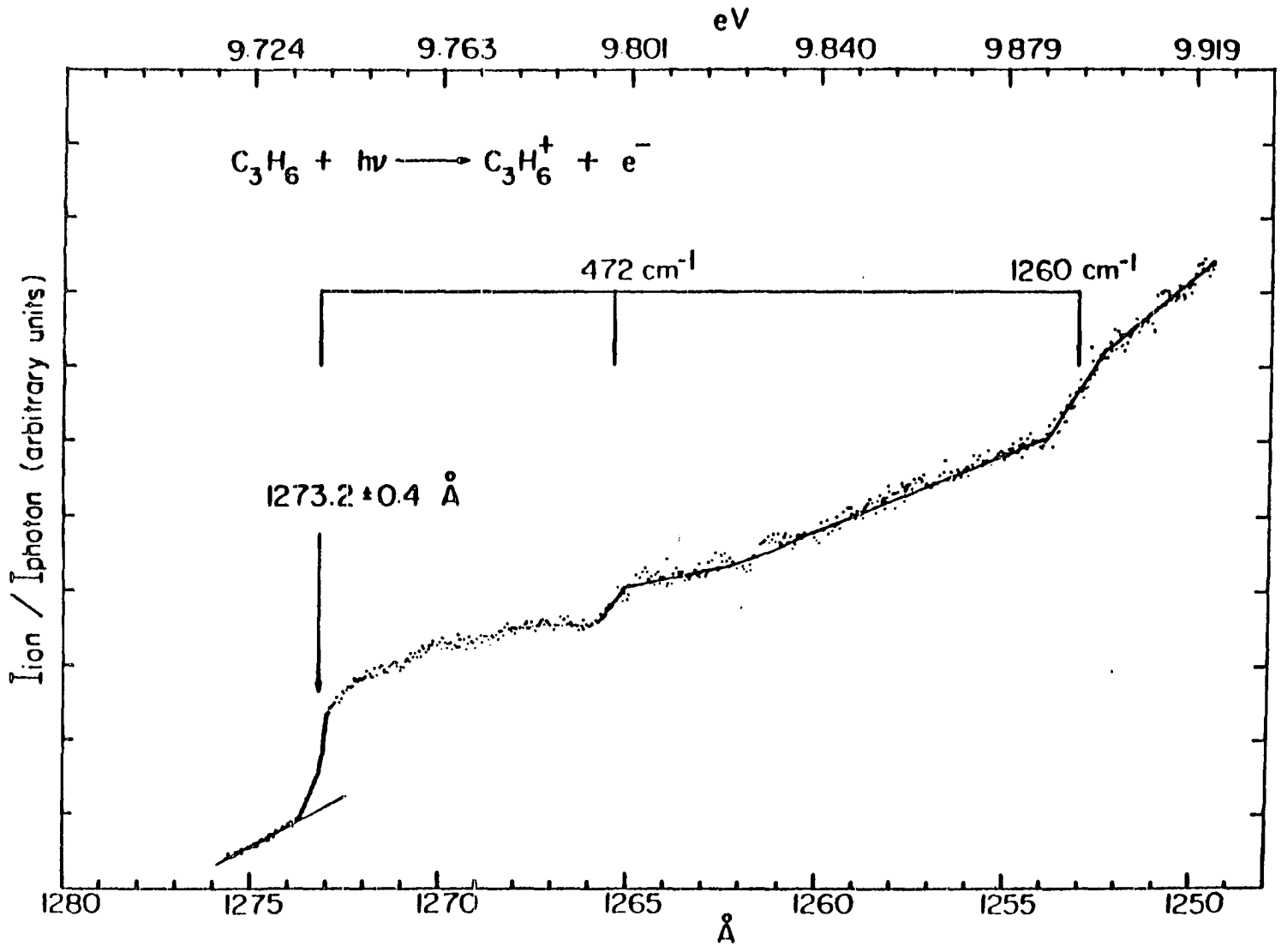
eV
9.724
9.763
9.801
9.840
9.879
9.919
$C_3H_6 + h\nu \longrightarrow C_3H_6^+ + e^-$
472 cm⁻¹
1260 cm⁻¹
1273.2 ± 0.4 Å
I ion / I photon (arbitrary units)
1280
1275
1270
1265
1260
1255
1250
Å

The ejection of a bonding electron from the C=C π orbital necessarily weakens the C=C bond. The fact that the latter values are lower than ν_{20} and ν_6 modes of C_3H_6 favors the assignment of the second and third steps to ν_{20} and ν_6 of $C_3H_6^+$, respectively.

Due to the Jahn-Teller effect, the ionization cross sections near the ionization threshold of c-C_3H_6 are expected to be very small. Since PIE curve for c-$C_3H_6^+$ exhibits a tailing structure near the threshold which makes it difficult to distinguish the hot band effect, previous photoionization experiments[26,28,29] can provide only an upper limit of 9.91 eV[26] for the adiabatic IE of c-C_3H_6. The first band of the photoelectron spectrum of c-C_3H_6[43,44] exhibits a long progression of peaks with an average spacing of ~ 480 cm^{-1} which has been assigned to the ring deformation ν_{11} mode of c-$C_3H_6^+$. The PIE spectrum for c-$C_3H_6^+$ obtained in the region of 1210-1285 Å using the supersonic molecular beam photoionization method is shown in Fig. 2. As a result of efficient rotational relaxation in the supersonic expansion, vibrational structure corresponding to the excitation of the ν_{11} mode of c-$C_3H_6^+$ is clearly evident. The average vibrational spacing (~ 434 cm^{-1}) observed in Fig. 2 is slightly lower than the value of ~ 480 cm^{-1} found in photoelectron experiments. The IE of c-C_3H_6 is determined to be 9.721±0.011 eV (1275.5±1.5 Å). This value is approximately 0.2 eV lower than the estimates obtained by previous photoionization and photoelectron studies.

The PIE curves for $C_3H_6^+$, $C_4H_7^+$, $C_4H_8^+$, $C_5H_9^+$, and $(C_3H_6)_2^+$ in the region of ~ 650-1350 Å obtained with a wavelength resolution of 1.4 Å

Figure 2. PIE curve for $c\text{-}C_3H_6^+$ in the region of 1210-1285 Å obtained using the hydrogen many-lined pseudocontinuum as the light source [wavelength resolution = 1.4 Å(FWHM), P_0 ~ 200 Torr, T_0 ~ 298 K].

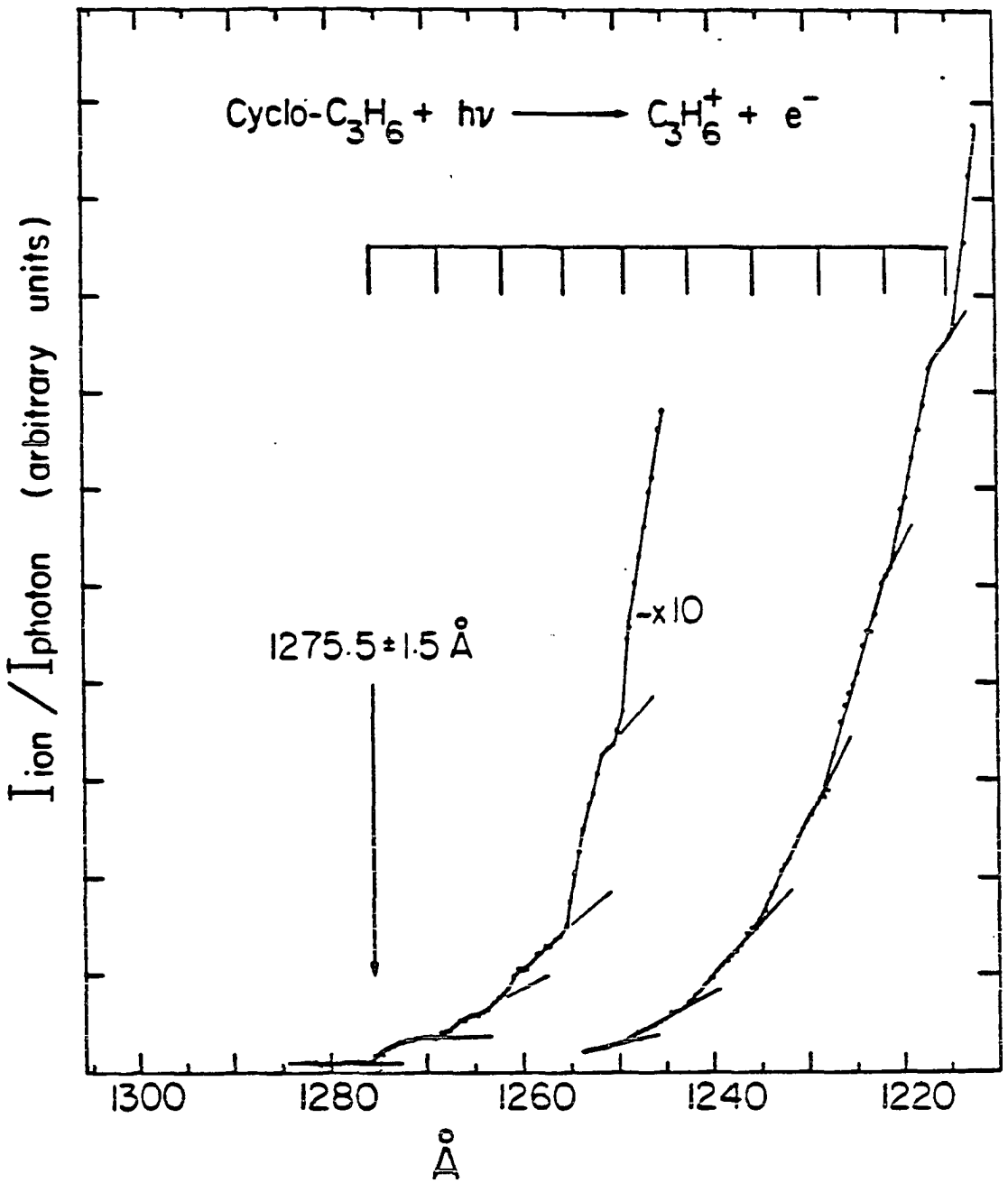
Cyclo-C_3H_6 + hν ⟶ $C_3H_6^+$ + e^-
I_{ion} / I_{photon} (arbitrary units)
1275.5 ± 1.5 Å
-x10
1300
1280
1260
1240
1220
Å

(FWHM) can be compared in Fig. 3. Because the intensity of $C_3H_7^+$ observed in this experiment is much lower than that of $^{13}C^{12}C_2H_6^+$, it is not possible to measure the PIE spectrum for $C_3H_7^+$ with accuracy. The PIE spectrum for $C_3H_6^+$ shown in Fig. 3(a) is in good agreement with those reported previously.[26,27]

The PIE spectrum for $(C_3H_6)_2^+$ is similar to that for $C_3H_6^+$. The IE of $(C_3H_6)_2$ is determined to be 9.33±0.04 eV (1329±5 Å). Using this value, together with the estimated binding energy for $C_3H_6 \cdot C_3H_6$ (0.026 eV)[45] and the IE of C_3H_6, the bond dissociation energy for $C_3H_6^+ \cdot C_3H_6$ is calculated to be 0.43±0.05 eV. This value is substantially lower than the bond dissociation energy for $C_2H_4^+ \cdot C_2H_4$ (0.69±0.04 eV).[20] The lower bond dissociation energy observed for $(C_3H_6)_2^+$ can be rationalized as partly due to steric effects between the methyl group in $C_3H_6^+$ or C_3H_6 with the other moiety of the dimer ion. The methyl groups in $(C_3H_6)_2^+$ may prevent the optimum bonding interaction between $C_3H_6^+$ and C_3H_6. The previous molecular orbital calculation indicates that the C=C π bond in C_3H_6 acquires some antibonding character through interaction with the methyl group orbitals. The comparison of the bond dissociation energies for $(O_2)_2^+$, $(NO)_2^+$, $(CO)_2^+$, and $(N_2)_2^+$ reveals that the bond dissociation energy of a dimer ion decreases dramatically as the number of antibonding electrons in the diatom increases.[46] A lower bond dissociation for $(C_3H_6)_2^+$ in comparison to that for $(C_2H_4)_2^+$ is consistent with that observation.

In order to visualize the observation of this study, a pseudo-reaction-coordinate diagram (Fig. 4) showing the stabilities (or heats

Figure 3. PIE curves for $C_3H_6^+$, $C_4H_7^+$, $C_4H_8^+$, $C_5H_9^+$, and $(C_3H_6)_2^+$ in the region of 650-1350 Å.

(a) PIE curve for $C_3H_6^+$ in the region of 650-1280 Å [wavelength resolution = 1.4 Å (FWHM), P_0 ~ 200 Torr, T_0 ~ 298 K].

(b) PIE curve for $C_4H_7^+$ in the region of 650-1325 Å [wavelength resolution = 1.4 Å (FWHM), P_0 ~ 500 Torr, T_0 ~ 250 K].

(c) PIE curve for $C_4H_8^+$ in the region of 650-1320 Å [wavelength resolution = 1.4 Å (FWHM), P_0 ~ 500 Torr, T_0 ~ 250 K].

(d) PIE curve for $C_5H_9^+$ in the region of 650-1320 Å [wavelength resolution = 1.4 Å (FWHM), P_0 ~ 500 Torr, T_0 ~ 250 K].

(e) PIE curve for $(C_3H_6)_2^+$ in the region of 650-1350 Å [wavelength resolution = 1.4 Å (FWHM), P_0 ~ 500 Torr, T_0 ~ 250 K].

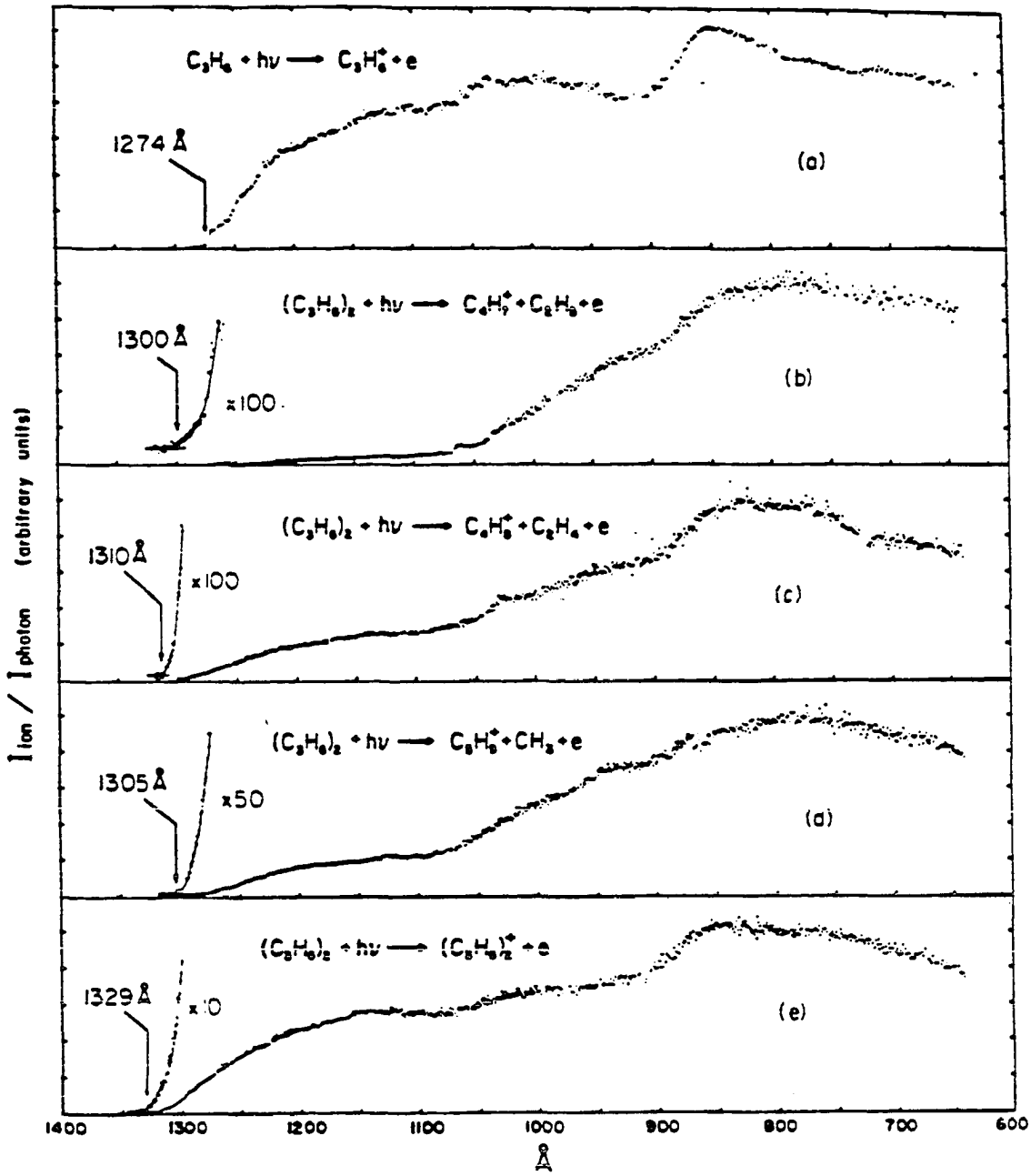
$C_3H_6 + h\nu \longrightarrow C_3H_6^+ + e$
1274 Å
(a)
$(C_3H_6)_2 + h\nu \longrightarrow C_4H_7^+ + C_2H_5 + e$
1300 Å
x100
(b)
$(C_3H_6)_2 + h\nu \longrightarrow C_4H_8^+ + C_2H_4 + e$
1310 Å
x100
(c)
$(C_3H_6)_2 + h\nu \longrightarrow C_5H_9^+ + CH_3 + e$
1305 Å
x50
(d)
$(C_3H_6)_2 + h\nu \longrightarrow (C_3H_6)_2^+ + e$
1329 Å
x10
(e)
I_{ion} / I_{photon} (arbitrary units)
1400
1300
1200
1100
1000
900
800
700
600
Å

Figure 4. Pseudo-reaction-coordinate diagram for the decompositions of $(C_3H_6)_2^+$ and $(c\text{-}C_3H_6)_2^+$.

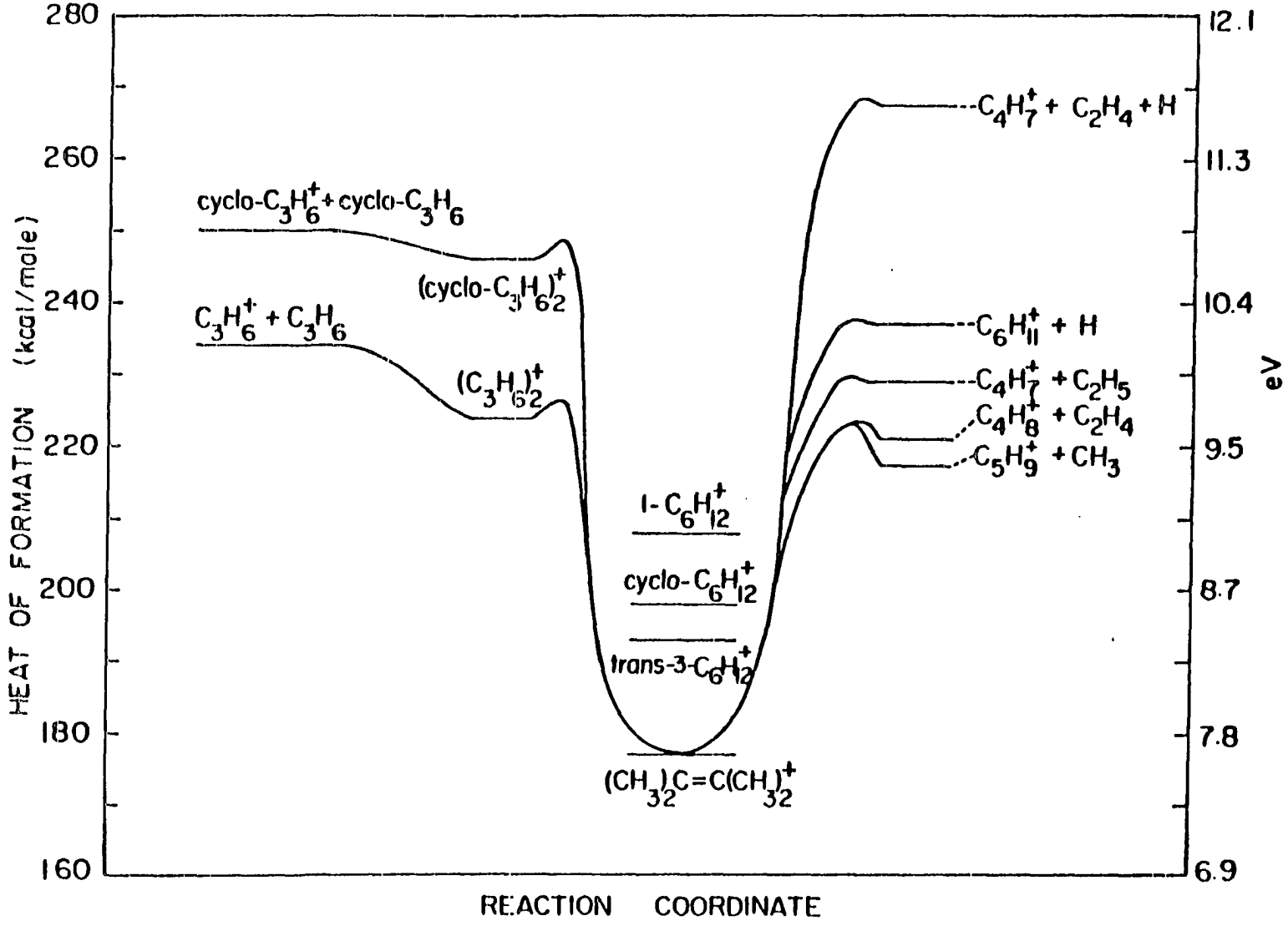
280
260
240
220
200
180
160
HEAT OF FORMATION (kcal/mole)
12.1
11.3
10.4
9.5
8.7
7.8
6.9
eV
cyclo-C3H6+ + cyclo-C3H6
(cyclo-C3H6)2+
C3H6+ + C3H6
(C3H6)2+
1-C6H12+
cyclo-C6H12+
trans-3-C6H12+
(CH3)2C=C(CH3)2+
C4H7+ + C2H4 + H
C6H11+ + H
C4H7+ + C2H5
C4H8+ + C2H4
C5H9+ + CH3
REACTION COORDINATE

of formation) of various dissociation channels is constructed with use of the thermochemical data reported here and in the literature (see Table I).[45,47-56] We have assumed that the dissociation of the loose $(C_3H_6)_2^+$ [or$(c\text{-}C_3H_6)_2^+$] complex involves prior rearrangements to some stable $C_6H_{12}^+$ complex ions. Based on the known values for the heats of formation of $(C_3H_6)_2$,[45,47] $C_4H_7^+$,[53] and C_2H_5,[54-56] the thermochemical threshold for reaction (5) is predicted to be 9.53±0.09 eV. In the calculation, the $C_4H_7^+$ produced near the threshold is assumed to have the most stable 1-methylallyl cation structure. The appearance energy (AE) for $C_4H_7^+$ from $(C_3H_6)_2$ is determined to be 9.54±0.04 eV (1300±5 Å), a value in excellent agreement with the predicted thermochemical threshold. This observation can be interpreted that the exit potential energy barrier[57] for reaction (2) or (5), located between stable $C_6H_{12}^+$ complexes and $C_4H_7^+ + C_2H_5$ (Fig. 4), is negligible.

Abramson and Futrell[15] have compared the distribution of $C_4H_7^+$, $C_4H_8^+$, and $C_5H_9^+$ formed by reactions (2)-(4) with the low energy electron impact mass spectra of several stable C_6H_{12} isomers. They found good correlations between the fragment ion intensities from 2-hexene as well as 3-hexene and the propylene ion-molecule reaction product distribution. In a solid phase radiolysis study of propylene[58] under conditions where deactivation of $[C_6H_{12}^+]^*$ complexes will freeze the ion in its initial configuration, a large number of C_6H_{12} isomers were observed with the major products being 1-hexene and 3-methyl-1-pentene.

A plausible mechanism[15] for the rearrangement of $(C_3H_6)_2^+$ to various linear $C_6H_{12}^+$ isomer is

Table I. 298 K heats of formation in kcal/mol of neutrals and ions[a]

Compounds	Neutrals	Ions
$(C_3H_6)_2$	9.16(45,47)	224.3[b]
$(c\text{-}C_3H_6)_2$	24.9[c](47)	246.5[b]
$1(C_6H_{12})$		208(48)
Trans-3-C_6H_{12}		193(48)
Cyclohexane		~ 198(48)
$(CH_3)_2C{=}C(CH_3)_2$		177(48)
C_6H_{11}(cyclohexyl)		185(50)
1,3-Dimethylallyl		183.5(50)
1,1-Dimethylallyl		184.9(50)
C_5H_9(cyclopentyl)		194(49)
C_4H_8(cyclobutane)		238(52)
Methylcyclopropane		239(52)

[a]The numbers in the parentheses are the references.

[b]This work.

[c]This value is calculated by assuming the binding energy for $(c\text{-}C_3H_6)_2$ to be the same as $(C_3H_6)_2$.

Table I. (continued)

Compounds	Neutrals	Ions
$1\text{-}C_4H_8$		221(49)
$Cis\text{-}2\text{-}C_4H_8$		209(49)
$Trans\text{-}2\text{-}C_4H_8$		208(49)
$Iso\text{-}C_4H_8$		209(49)
1-Methylallyl		203.1±1.4(53)
2-Methylallyl		212±1.6(53)
Cyclobutyl		225.1±1.1(53)
Allylcarbinyl		231.0±3(53)
C_3H_6	4.88(47)	229.4[b]
$c\text{-}C_3H_6$	12.74(47)	237[b]
C_2H_5	25.7(54)	
	28.3±1.1(55)	
	25.9±1(56)	
C_2H_4	12.54±0.07(47)	
CH_3	34.8±0.2(47)	
	35.1±0.5(55,56)	
H	52.100±0.001(47)	

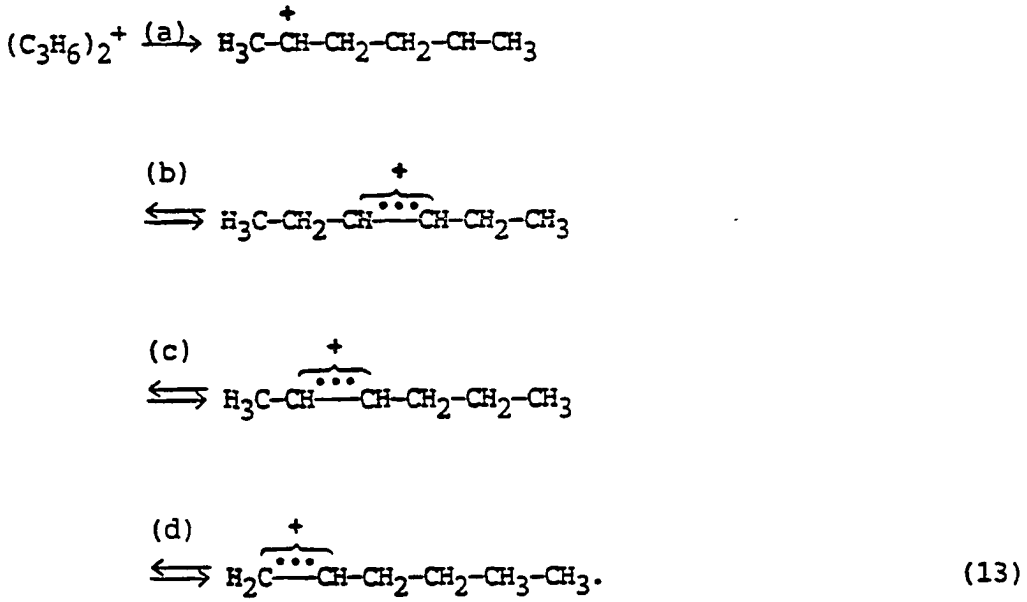

After making a C-C bond between $C_3H_6^+$ and C_3H_6 by step (13a), the formations of the linear hexene ions by steps (13b)-(13d) only involve stepwise 1,2-hydrogen shift which is expected to have a low activation barrier of ~ 6-12 kcal/mol.[59] At the total energy (neutral heat of formation plus excitation energy) range of interest here, the linear hexene ions should be interconvertable. The formation of $C_4H_7^+$ (1-methyallyl cation) most likely proceeds via the 2-hexene ion structure:

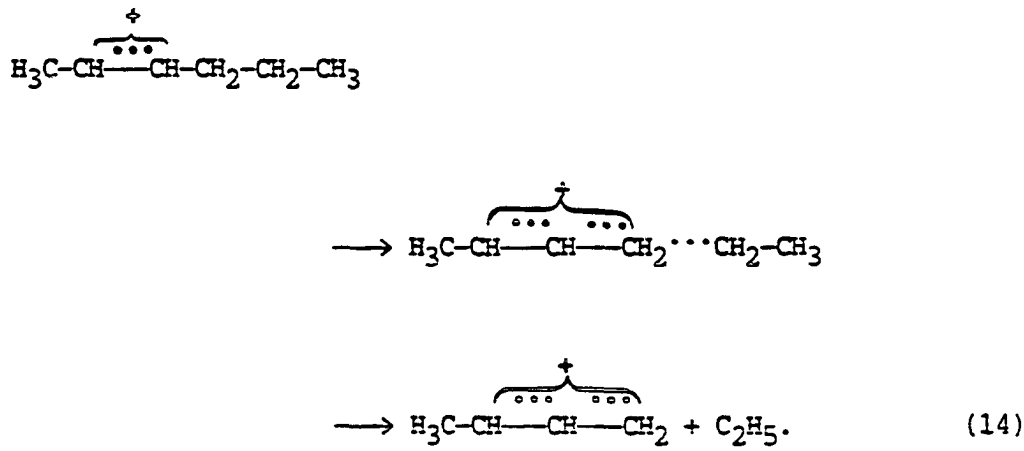

Due to the stabilization of the allyl cationlike structure, reaction (14) should be a favorable dissociation pathway. According to previous studies,[20,21] the reverse of process (14), is expected to have negligible activation energy. The experimental observation is consistent with this expectation.

One of the pathways for the formation of $C_5H_9^+$ is the elimination of CH_3 from 3-hexene. However, the 1-ethylallyl cation resulting is not the most stable $C_5H_9^+$ ion. Other $C_6H_{12}^+$ intermediate ions can be produced by forming a C-C bond between nonequivalent carbon atoms in $C_3H_6^+$ and C_3H_6:

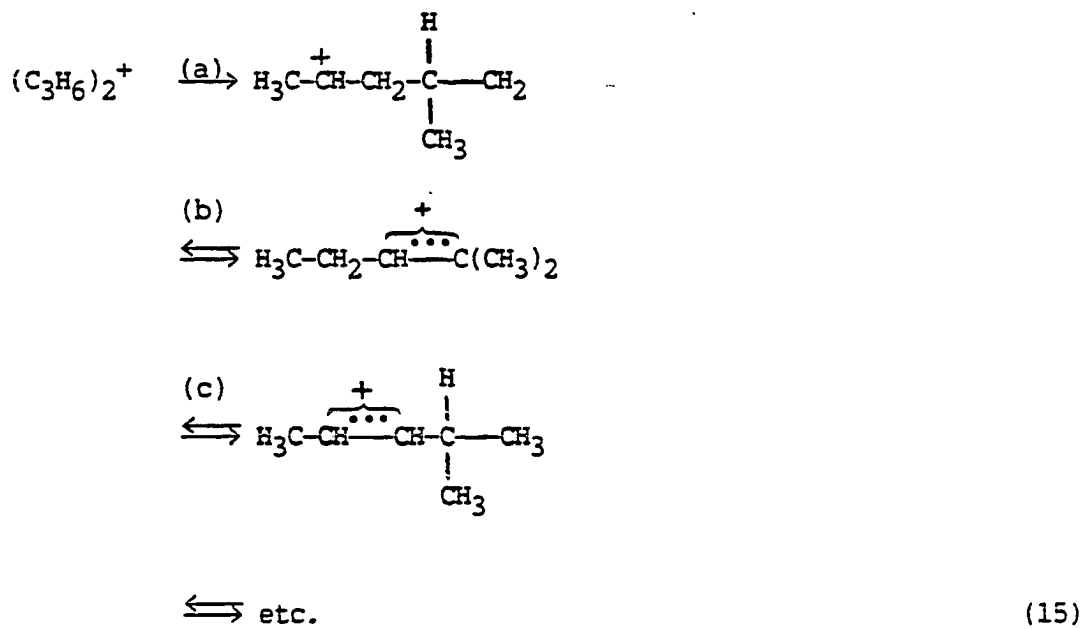

(15)

Again the interconversion of different structures by processes such as (15b) and (15c) involves only hydrogen shifts. The formations of the more stable $C_5H_9^+$ isomers, 1,3-dimethylallyl and 1,1-dimethylallyl cations, can result from the processes

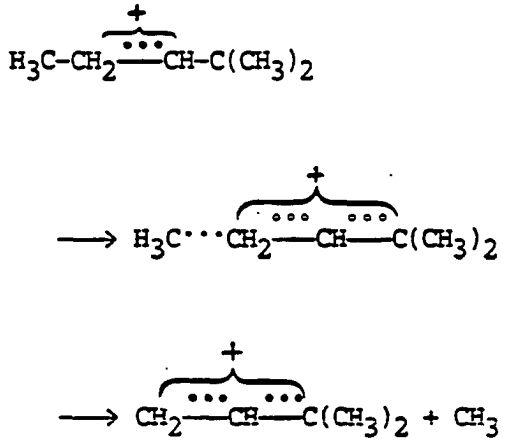

(16)

and

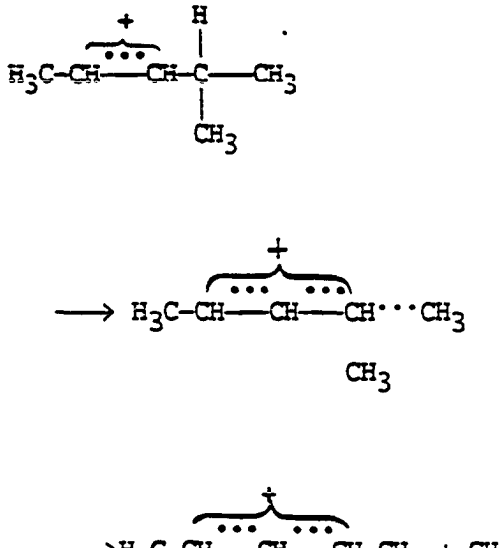

(17)

The isotopic study of the propylene ion-molecule reactions by Abramson and Futrell[16] also suggests the involvement of the symmetric collisional complex,

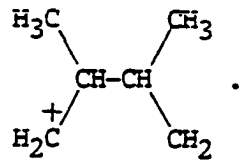

This radicalion can give rise to $C_5H_9^+$ with the 1,1-dimethylally cation structure via rearrangement processes similar to those described above.

The AE for the formation of $C_5H_9^+$ from $(C_3H_6)_2$ is found to be 9.50±0.04 eV (1305±5 Å). If the $C_5H_9^+$ ion is assumed to have the most stable 1,3-dimethylallyl cation structure, the predicted thermochemical threshold (9.08 eV) for reaction (8) is ~ 0.4 eV lower than the measured AE for $C_5H_9^+$. Since the heat of formation for $(C_3H_6)_2^+$ (224.3 kcal/mol) is higher than the sum of the heats of formation for 1,3-dimethylallyl cation and CH_3 (218.6 kcal/mol) this experiment cannot provide an unambiguous value for the exit potential energy barrier for reaction (4) or (8). Nevertheless, the AE for $C_5H_9^+$ measured here gives an upper bound of 9.2 kcal/mol for the activation barrier for the reverse of reaction (8). As discussed above, if $C_5H_9^+$ ions are formed via processes (16) and (17) which are similar to process (14), the exit potential energy barrier for reaction (4) or (8) is also expected to be negligibly small. The difference (0.17±0.06 eV) between the AE for $C_5H_9^+$ and the IE of $(C_3H_6)_2$ is interpreted as the potential energy barrier for the rearrangement of $(C_3H_6)_2^+$ to stable $C_6H_{12}^+$ isomers by processes such as (13a) and (15a). We note that the AE for $C_5H_9^+$ is in

agreement with the thermochemical threshold for reaction (8) if the $C_5H_9^+$ product ion has the cyclopentyl cation structure. Since there are no strong arguments which exclude the formations of the 1,1-dimethylallyl and 1,3-dimethylallyl cations near the threshold, we believe the coincidence is fortuitous.

Assuming that the $C_4H_8^+$ ions formed near the threshold have the most stable trans-2-$C_4H_8^+$ structure, the thermochemical threshold for reaction (7) is calculated to be 9.17 eV. This value is lower than the AE of 9.46±0.04 eV (1310±5 Å) for $C_4H_8^+$ from $(C_3H_6)_2$ measured in this experiment. The later value provides an upper limit of ~ 6 kcal/mol for the potential energy barrier for the reverse of reaction (7). Taking into account the error limits of both measurements, the AE for $C_4H_8^+$ is equal to that for $C_5H_9^+$ from $(C_3H_6)_2$. Therefore, the AE for $C_4H_8^+$ probably also reflects the potential energy barrier for the rearrangement from $(C_3H_6)_2^+$ to stable $C_6H_{12}^+$ isomers involved in the dissociation process.

It can be seen from the PIE spectra for $C_4H_7^+$, $C_4H_8^+$, $C_5H_9^+$, and $(C_3H_6)_2^+$ [Figs. 3(b)-3(e)] that the relative intensities of these ions vary in the region of ~ 900-1350 Å. The relative abundances $I[(C_3H_6)_2^+]/\Sigma$, $I(C_4H_7^+)/\Sigma$, $I(C_4H_8^+)/\Sigma$, and $I(C_5H_9^+)/\Sigma$ for $(C_3H_6)_2^+$, $C_4H_7^+$, $C_4H_8^+$, and $C_5H_9^+$, respectively, in percentage, as a function of photon energy in the region of 650-1350 Å, are plotted in Fig. 5. Here $I[(C_3H_6)_2^+]$, $I(C_4H_7^+)$, $I(C_4H_8^+)$, and $I(C_5H_9^+)$ represent the intensities of $(C_3H_6)_2^+$, $C_4H_7^+$, $C_4H_8^+$, and $C_5H_9^+$, respectively. Σ is the sum of $I[(C_3H_6)_2^+]$, $I(C_4H_7^+)$, $I(C_4H_8^+)$, and $I(C_5H_9^+)$. The relative abundance

Figure 5. The variations of the relative abundances for $(C_3H_6)_2^+$ (+), $C_4H_8^+$ (O), $C_5H_9^+$ (Δ), and $C_4H_7^+$ (●) as a function of photon energy. Σ is the sum of $I[(C_3H_6)_2^+]$, $I(C_4H_8^+)$, $I(C_5H_9^+)$, and $I(C_4H_7^+)$, where $I[(C_3H_6)_2^+]$, $I(C_4H_8^+)$, $I(C_5H_9^+)$, and $I(C_4H_7^+)$ represent the intensities for $(C_3H_6)_2^+$, $C_4H_8^+$, $C_5H_9^+$, and $C_4H_7^+$, respectively. No corrections were made to account for transmission factors of these ions through the mass spectrometer.

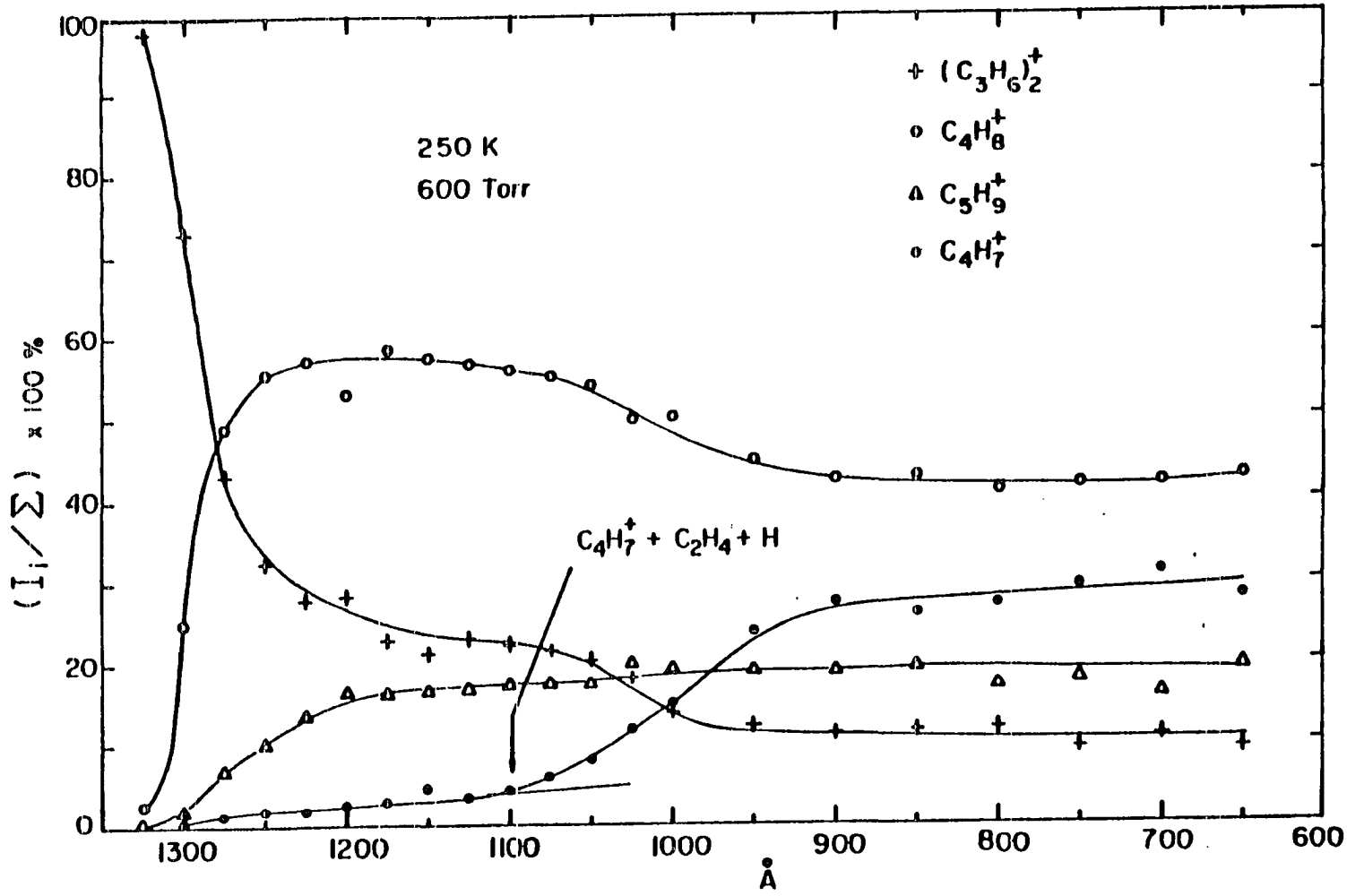
250 K
600 Torr
$(C_3H_6)_2^+$
$C_4H_8^+$
$C_5H_9^+$
$C_4H_7^+$
$C_4H_7^+ + C_2H_4 + H$
(I_i/Σ) x 100 %
100
80
60
40
20
0
1300
1200
1100
1000
900
800
700
600
Å

diagram is based on PIE data measured at P_0 ~ 600 Torr, T_0 ~ 250 K, and wavelength intervals of either 25 or 50 Å. No corrections have been made for the differences in transmission of these ions through the mass spectrometer. As a result of a much shorter time span used to obtain these data, in comparison to that needed to measure the PIE data shown in Figs. 4(b)-4(e), the data plotted in Fig. 5 are believed to be less susceptible to minor experimental fluctuations and thus to be more representative of the relative abundances of these ions.

As a consequence of autoionization and direct ionization processes, the internal energy of $(C_3H_6)_2^+$ should increase as the excitation photon energy increases. Although the $C_3H_7^+ + C_3H_5$ and the $C_3H_6^+ + C_3H_6$ channels are excluded in this measurement,[60] the relative abundance plot shown in Fig. 5 still displays the important features anticipated in the unimolecular decomposition of $(C_3H_6)_2^+$. Similar to the observations in previous studies,[20,21] the relative abundance of the parent dimer ion $(C_3H_6)_2^+$ decreases dramatically while those for $C_4H_7^+$, $C_4H_8^+$, and $C_5H_9^+$ increase after the onsets of $C_4H_7^+$, $C_4H_8^+$, and $C_5H_9^+$. The relative abundances for $C_4H_7^+$, $C_4H_8^+$, and $C_5H_9^+$ observed in the region of ~ 1000-1270 Å are found to be in the order $I(C_4H_8^+) > I(C_5H_9^+) > I(C_4H_7^+)$, in qualitative agreement with those found for the $C_3H_6^+ + C_3H_6$ reactions in a single chamber photoionization mass spectrometeric study induced with 10.0 and 11.7 eV photons.[18] The value for $I(C_5H_9^+)/\Sigma$ remains nearly constant in the region of ~ 650-1200 Å. The relative abundance for $C_4H_7^+$ is low at wavelengths longer than ~ 1100 Å. Accompanying the decreases of $I(C_4H_8^+)/\Sigma$ and $I[(C_3H_6)_2^+]/\Sigma$, a substantial increase in

$I(C_4H_7^+)/\Sigma$ is found in the region of ~ 900-1100 Å. Since the thermochemical threshold of reaction (6) (11.27 eV) coincides with the onset (~ 1100 Å) of the further increase in $I(C_4H_7^+)/\Sigma$, the increase in relative abundance at wavelengths shorter than ~ 1100 Å is most likely due to the formation of $C_4H_7^+ + C_2H_4 + H$ and to the further decomposition of $C_4H_8^+$ into $C_4H_7^+ + H$.

The PIE data for $(c\text{-}C_3H_6)_2^+$, $C_5H_9^+$, $C_4H_8^+$, and $C_4H_7^+$ from $(c\text{-}C_3H_6)_2$ in the region of 650-1300 Å obtained at P_o ~ 500 Torr and T_o ~ 250 K are plotted in Fig. 6. The PIE curve for $c\text{-}C_3H_6^+$, recorded using the same wavelength resolution of 1.4 Å (FWHM) at P_o ~ 200 Torr and T_o ~ 298 K, is shown in Fig. 6(a) for comparison. This $c\text{-}C_3H_6^+$ spectrum is in excellent agreement with that reported previously.[26]

The IE for $(c\text{-}C_3H_6)_2^+$ is determined to be 9.61±0.04 eV (1290±5 Å). The binding energy for $(c\text{-}C_3H_6)_2$ is not known. Assuming the binding enrgy for $(c\text{-}C_3H_6)_2$ to be the same as that for $(C_3H_6)_2$ and using the IE's for $c\text{-}C_3H_6$ and $(c\text{-}C_3H_6)_2$ determined here, we calculate the bond dissociation energy for $(c\text{-}C_3H_6)_2^+$ to be 0.14 eV. This value is less than one third that for $(C_3H_6)_2^+$.

Taking into account the experimental uncertainties, the values for the AE's for $C_5H_9^+$, $C_4H_8^+$, and $C_4H_7^+$ are identical. The difference of ~ 0.09 eV between the AE's of these ions and the IE of $(c\text{-}C_3H_6)_2$ can be interpreted as the potential energy barrier for the rearrangement from $(c\text{-}C_3H_6)_2^+$ to stable $C_6H_{12}^+$ isomers (Fig. 4).

The relative abundances for $C_4H_7^+$, $C_4H_8^+$, $C_5H_9^+$, and $(c\text{-}C_3H_6)_2^+$ from $(c\text{-}C_3H_6)_2$ are plotted as a function of photon energy in Fig. 7.

Figure 6. PIE curves for $c\text{-}C_3H_6^+$, $(c\text{-}C_3H_6)_2^+$, $C_5H_9^+$, $C_4H_8^+$, and $C_4H_7^+$ in the region of 650–1305 Å.

(a) PIE curve for $c\text{-}C_3H_6^+$ in the region of 650–1295 Å [wavelength resolution = 1.4 Å (FWHM), P_0 ~ 200 Torr, T_0 ~ 298 K].

(b) PIE curve for $(c\text{-}C_3H_6)_2^+$ in the region of 650–1305 Å [wavelength resolution = 1.4 Å (FWHM), P_0 ~ 500 Torr, T_0 ~ 250 K].

(c) PIE curve for $C_5H_9^+$ in the region of 650–1295 Å [wavelength resolution = 1.4 Å (FWHM), P_0 ~ too Torr, T_0 ~ 250 K].

(d) PIE curve for $C_4H_8^+$ in the region of 650–1290 Å [wavelength resolution = 1.4 Å (FWHM), P_0 ~ 500 Torr, T_0 ~ 250 K].

(e) PIE curve for $C_4H_7^+$ in the region of 650–1290 Å [wavelength resolution = 1.4 Å (FWHM), P_0 ~ 500 Torr, T_0 ~ 250 K].

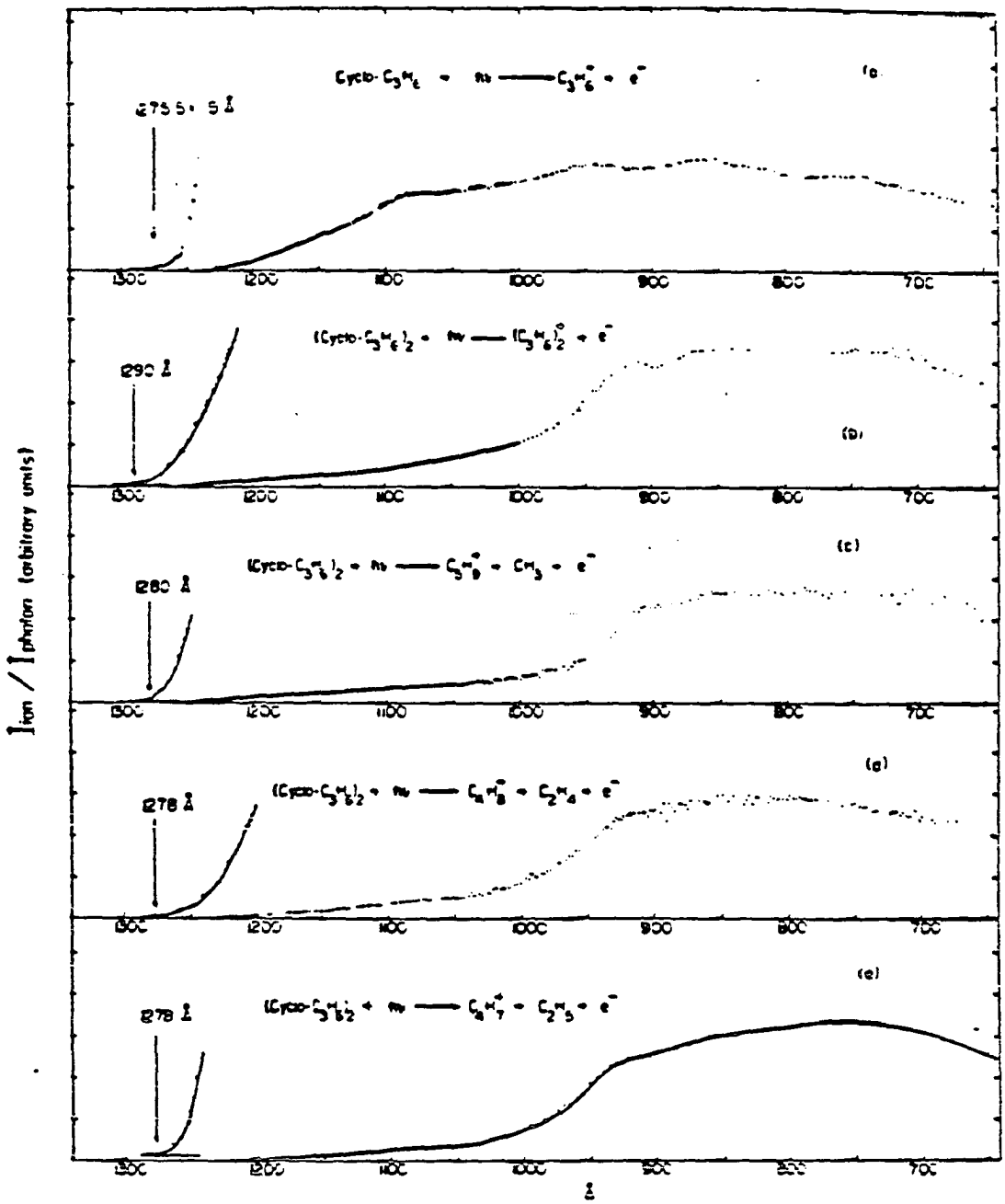
Cyclo-C_3H_6 + hν ——— $C_3H_6^+$ + e^-
(a)
2755 ± 5 Å
1300
1200
1100
1000
900
800
700
$(Cyclo\text{-}C_3H_6)_2$ + hν ——— $(C_3H_6)_2^+$ + e^-
2900 Å
(b)
$(Cyclo\text{-}C_3H_6)_2$ + hν ——— $C_5H_9^+$ + CH_3 + e^-
(c)
2800 Å
$(Cyclo\text{-}C_3H_6)_2$ + hν ——— $C_4H_8^+$ + C_2H_4 + e^-
(d)
2780 Å
$(Cyclo\text{-}C_3H_6)_2$ + hν ——— $C_4H_7^+$ + C_2H_5 + e^-
(e)
2780 Å
I_{ion} / I_{photon} (arbitrary units)
Å

Figure 7. The variations of the relative abundances for $(c\text{-}C_3H_6)_2^+$ (●), $C_4H_8^+$ (+), $C_5H_9^+$ (O), and $C_4H_7^+$ (Δ) as a function of photon energy. Σ is the sum of $I[(c\text{-}C_3H_6)_2^+]$, $I(C_4H_8^+)$, $I(C_5H_9)^+$, and $I(C_4H_7)^+$, where $I[(c\text{-}C_3H_6)_2^+]$, $I(C_4H_8^+)$, $I(C_5H_9^+)$, and $I(C_4H_7^+)$ represent the intensities for $(c\text{-}C_3H_6)_2^+$, $C_4H_8^+$, $C_5H_9^+$, and $C_4H_7^+$, respectively. No corrections were made to account for transmission factors of these ions through the mass spectrometer.

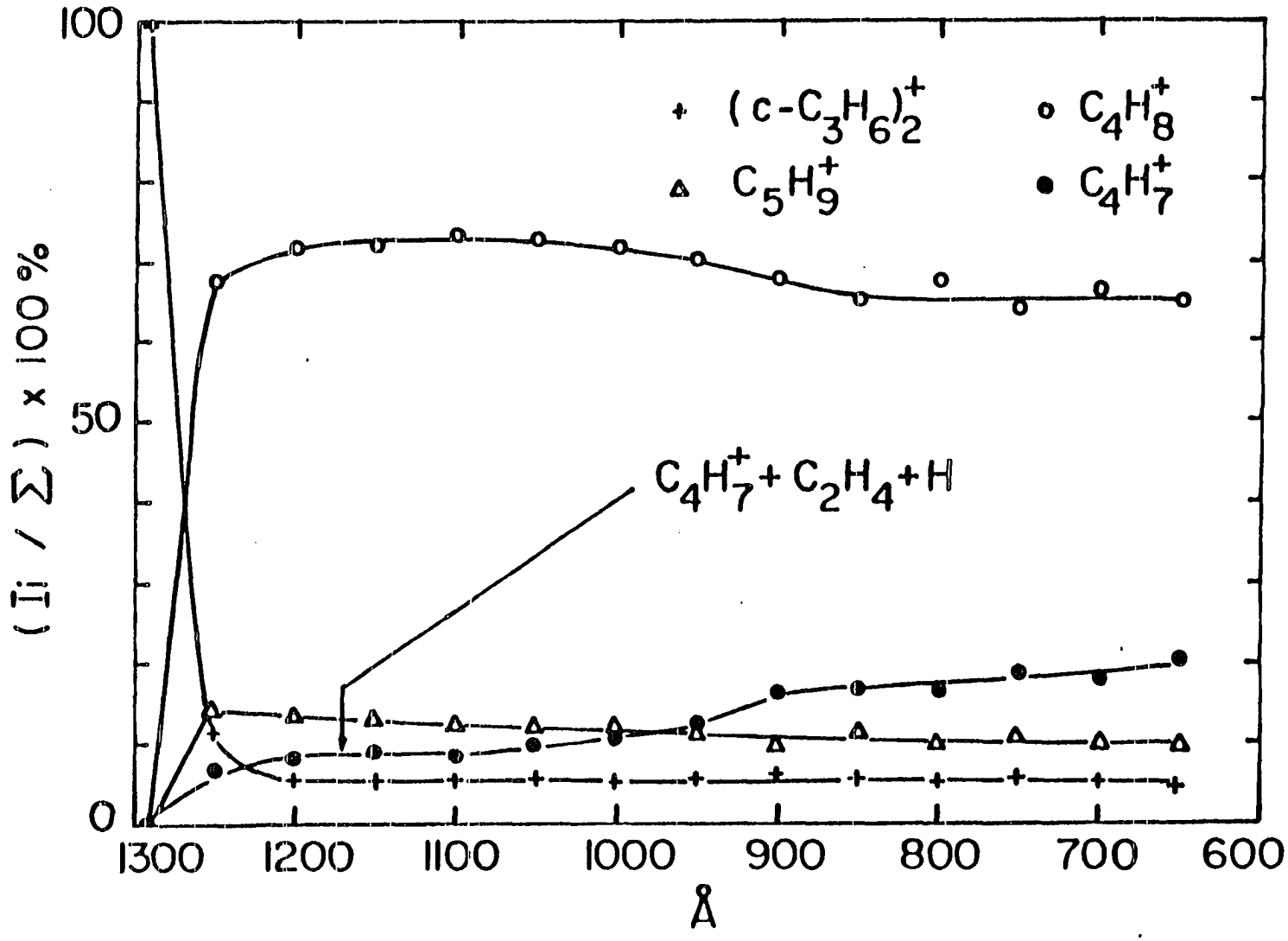
100
50
0
(Ii / Σ) x 100 %
(c-C3H6)2+
C4H8+
C5H9+
C4H7+
C4H7+ + C2H4 + H
1300
1200
1100
1000
900
800
700
600
Å

The variations of the relative abundances for $C_4H_7^+$, $C_4H_8^+$, $C_5H_9^+$ from $(c\text{-}C_3H_6)_2$ are in qualitative agreement with those found in Fig. 5. The relative yield for $C_4H_8^+$ from the unimolecular decomposition of $(c\text{-}C_3H_6)_2^+$ shown in Fig. 7 is greater than that from $(C_3H_6)_2^+$. Previous experiments also reveal that the relative intensity for $C_4H_8^+$ produced in the ion-molecule reaction of $c\text{-}C_3H_6^+ + c\text{-}C_3H_6$ is higher than that from reaction (7). The first step in the rearrangement of $(c\text{-}C_3H_6)_2^+$ to form a $C_6H_{12}^+$ complex most likely involves the breaking of a C-C bond in the neutral partner. It has been pointed out[18] that since the elimination of C_2H_4 from the neutral can occur rapidly without extensive rearrangement, the relative abundance of $C_4H_8^+$ from $(c\text{-}C_3H_6)_2^+$ is expected to be higher. The thermochemical threshold for reaction (10) is calculated to be 10.52 eV (1179 Å). As shown in Fig. 7, the correlation between the threshold for the formation of $C_4H_7^+ + C_2H_4 + H$ and the further rise of the relative abundance is less apparent than that observed in Fig. 5.

The $C_6H_{11}^+$ ion has been identified as a prominent fragment ion from the unimolecular decomposition of $(C_2H_4)_3^+$.[19,20] If $(C_2H_4)_3^+$, $(C_3H_6)_2^+$, and $(c\text{-}C_3H_6)_2^+$ rearrange to some common stable $C_6H_{12}^+$ isomers prior to fragmenting, $C_6H_{11}^+$ should be a primary fragment from both $(C_3H_6)_2^+$ and $(c\text{-}C_3H_6)_2^+$. A careful search for $C_6H_{11}^+$ from $(C_3H_6)_2$ and $(c\text{-}C_3H_6)_2$ was made. Figures 8(a) and 8(b) display the mass spectra of $(C_3H_6)_2$ and $(c\text{-}C_3H_6)_2$ in the mass/e range of ~ 82-85 obtained at 1050 Å, respectively. The photon energy used is well above the thermochemical thresholds for the formation of $C_6H_{11}^+$ from $(C_3H_6)_2$ or $(c\text{-}C_3H_6)_2$. Interestingly,

Figure 8. Mass spectra of (a) $(C_3H_6)_2$ and (b) $(c\text{-}C_3H_6)_2$ in the mass range of 82–85 obtained using a photon wavelength of 1050 Å.

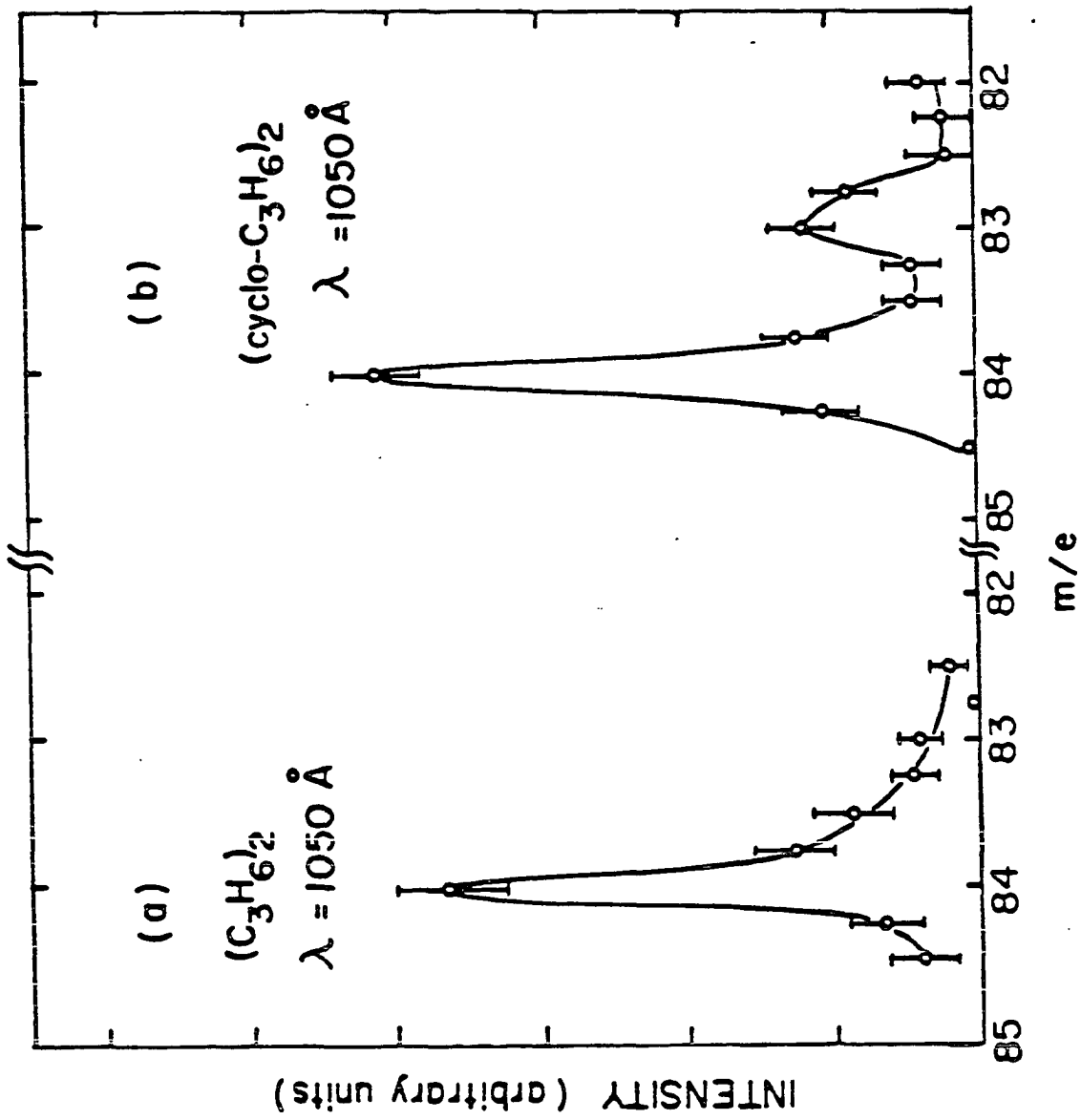
(a)
$(C_3H_6)_2$
λ = 1050 Å
(b)
(cyclo-$C_3H_6)_2$
λ = 1050 Å
INTENSITY (arbitrary units)
m/e
82
83
84
85

$C_6H_{11}^+$ is observed[61] in low abundance from $(c\text{-}C_3H_6)_2^+$ but not at all from $(C_3H_6)_2^+$. This observation supports the conclusion that the distribution of $C_6H_{12}^+$ collision complexes involved in the $C_3H_6^+ + C_3H_6$ reactions is different from that in the cyclopropane ion-molecule reactions. A previous experiment[58] has provided evidence showing that cyclopropane molecular ions do not assume the propylene ion structure prior to reaction with other paraffins.

Due to the tailing threshold intensities for fragment ions observed in this study and the kinetic shift effects,[62-66] all AE's reported here should be viewed as upper bounds. Based on the observation that the measured AE for $C_4H_7^+$ from $(C_3H_6)_2$ is in agreement with the thermochemical threshold of reaction (5), we believe the measured AE's are probably close to the true AE's.

In summary we have obtained higher resolution PIE spectra for $C_3H_6^+$ and $c\text{-}C_3H_6^+$ near the thresholds. The IE's of C_3H_6 and $c\text{-}C_3H_6$ are determined to be 9.738±0.003 and 9.721±0.011 eV, respectively. Based on the measured IE's of $(C_3H_6)_2$ and $(c\text{-}C_3H_6)_2$, the bond dissociation energies for $C_3H_6^+ \cdot C_3H_6$ and $c\text{-}C_3H_6^+ \cdot c\text{-}C_3H_6$ are estimated to be 0.43 and 0.14 eV, respectively. The $C_3H_7^+$, $C_4H_7^+$, $C_4H_8^+$, and $C_5H_9^+$, ions are identified as primary fragments from the unimolecular decompositions of $(C_3H_6)_2^+$ and $(c\text{-}C_3H_6^+)$. The relative abundances for $C_4H_7^+$, $C_4H_8^+$, and $C_5H_9^+$ from $(C_3H_6)_2^+$ and $(c\text{-}C_3H_6)_2^+$ in the total energy range of ~ 230-450 kcal/mol are found to be similar, indicating that $(C_3H_6)_2^+$ and $(c\text{-}C_3H_6)_2^+$ rearrange to similar $C_6H_{12}^+$ isomer ions prior to the formation of these product ions. However, the fact that $C_6H_{11}^+$ is observed as a

primary fragment from $(c\text{-}C_3H_6)_2^+$ but not $(C_3H_6)_2^+$ shows that the distributions of stable $C_6H_{12}^+$ isomers resulting from the rearrangements of $(C_3H_6)_2^+$ and $(c\text{-}C_3H_6)_2^+$ are different. The measured AE for $C_4H_7^+$ from $(C_3H_6)_2$ is consistent with the interpretation that the exit potential energy barrier for the $C_3H_6^+ + C_3H_6 \longrightarrow C_4H_7^+ + C_2H_5$ is negligible. The variations of the relative abundance for $C_4H_7^+$ from $(C_3H_6)_2^+$ and $(c\text{-}C_3H_6)_2^+$ reveal that the formations of $C_4H_7^+ + C_2H_4 + H$ from $(C_3H_6)_2^+$ and $(c\text{-}C_3H_6)_2^+$ proceed with high probabilities when they are energetically allowed.

References

1. V. L. Talrose and A. K. Lyubimova, Dokl. Akad. Nauk SSSR 86, 909 (1952).
2. D. O. Schissler and D. P. Stevenson, J. Chem. Phys. 24, 926 (1956).
3. R. Fuchs, Z. Naturforsch. Teil A 16, 1026 (1961).
4. A. G. Harrison, Can. J. Chem. 41, 236 (1962).
5. I. Koyano, I. Omura, and I. Tanaka, J. Chem. Phys. 44, 3850 (1966).
6. I. Koyano, J. Chem. Phys. 45, 706 (1966).
7. V. Aquilanti, A. Galli, A. Giardin-Guidoni, and G. G. Volpi, Trans. Faraday Soc. 63, 926 (1967).
8. L. W. Sieck and J. H. Futrell, J. Chem. Phys. 45, 560 (1966).
9. M. I. Gross and J. Norbeck, J. Chem. Phys. 54, 3651 (1971).
10. J. M. S. Henis, J. Chem. Phys. 52, 282 (1970).
11. O. P. Strausz, W. K. Duholke, and H. E. Gunning, J. Am. Chem. Soc. 92, 4128 (1970).
12. A. A. Herod and A. G. Harrison, Int. J. Mass Spectrom. Ion Phys. 4, 415 (1970).
13. A. A. Herod and A. G. Harrison, J. Phys. Chem. 73, 3189 (1969).

14. A. M. Peers, Int. J. Mass Spectrom. Ion Phys. 5, 483 (1970).

15. F. P. Abramson and J. H. Futrell, J. Chem. Phys. 72, 1826 (1968).

16. F. P. Abramson and J. H. Futrell, J. Chem. Phys. 72, 1994 (1968).

17. A. A. Herod, A. G. Harrison, R. M. O'Malley, A. J. Ferrer-Correia, and K. R. Jennings, J. Phys. Chem. 74, 2720 (1970).

18. L. W. Sieck and P. Ausloos, J. Res. Natl. Bur. Stand. Sect. A 76, 253 (1972).

19. S. T. Ceyer, P. W. Tiedemann, C. Y. Ng, B. H. Mahan, and Y. T. Lee, J. Chem. Phys. 70, 2138 (1979).

20. Y. Ono, S. H. Linn, W.-B. Tzeng, and C. Y. Ng, J. Chem. Phys. 80, 1482 (1984).

21. Y. Ono and C. Y. Ng, J. Chem. Phys. 77, 2947 (1982).

22. Y. Ono and C. Y. Ng, J. Am. Chem. Soc. 104, 4752 (1982).

23. Y. Ono, S. H. Linn, H. F. Prest, M. E. Gress, and C. Y. Ng, J. Chem. Phys. 73, 2523 (1980).

24. Y. Ono, S. H. Linn, H. F. Prest, C. Y. Ng, and E. Meisher, J. Chem. Phys. 73, 4855 (1980).

25. K. E. Schubert and R. D. Hudson, Rep. No. ATN-64(9233)-2 (Aerospace Corp., Los Angeles, 1963).

26. R. Kraßig, D. Reinke, and H. Baumgartel, Ber. Bunsenges. 78, 425 (1974).

27. K. V. Wood and J. W. Taylor, Int. J. Mass Spectrom. Ion Phys. 30, 307 (1979).

28. K. Watanabe, J. Chem. Phys. 26, 542 (1957).

29. K. Watanabe, T. Nakayama, and J. Mottl, J. Quant. Spectrosc. Radiat. Transfer. 2, 369 (1962).

30. R. Bralsford, P. V. Harris, and W. C. Price, Proc. Roy. Soc. London Ser. A 258, 459 (1960).

31. B. Steiner, C. F. Giese, and M. G. Inghram, J. Chem. Phys. 34, 189 (1961).

32. J. A. R. Samson, F. F. Marmo, and K. Watanabe, J. Chem. Phys. 36, 783 (1962).

33. A. J. C. Nicholson, J. Chem. Phys. 43, 1171 (1965).

34. J. C. Person and P. P. Nicole, J. Chem. Phys. 53, 1767 (1970).

35. M. J. S. Dewar and S. D. Worley, J. Chem. Phys. 50, 654 (1969).

36. P. Masclet, D. Grosjean, and G. Mouvier, J. Electron Spectrosc. Relat. Phenom. 2, 225 (1973).

37. D. C. Frost and J. S. Sandhu, Indian J. Chem. 9, 1105 (1971).

38. A. Katrib and J. W. Rabalais, J. Chem. Phys. 77, 2358 (1973).

39. W. C. Price and W. T. Tuttle, Proc. Roy. Soc. London ser. A 174, 207 (1940).

40. W. C. Price, Chem. Rev. 41, 257 (1974).

41. H. M. Cundy, Proc. Roy. Soc. London 164, 420 (1983).

42. A value of 578 cm^{-1} was mistakenly quoted for ν_{14} of C_3H_6 in Ref. 38.

43. D. W. Turner, Adv. Phys. Org. Chem. 4, 31 (1966).

44. H. Basch, M. B. Robin, N. A. Kuebler, C. Baker, and D. W. Turner, J. Chem. Phys. 51, 52 (1969).

45. L. W. Flynn and G. Thodos, A. I. Ch. E. Journal 8, 362 (1962).

46. S. H. Linn, Y. Ono, and C. Y. Ng, J. Chem. Phys. 74, 3342 (1981).

47. D. R. Stull, E. F. Westrum, Jr., and G. C. Sinke, The Chemical Thermodynamics of Organic Compounds (John Wiley & Sons, New York, 1969).

48. H. M. Rosenstock, K. Draxl, B. W. Steiner, J. T. Herron, J. Phys. Chem. Ref. Data, 6, Suppl.1 (1977).

49. J. L. Franklin, J. G. Dillard, H. M. Rosenstock, J. T. Herron, K. Draxl, and H. H. Field, Ionization Potentials, Appearance Potentials, and Heats of Formation of Gaseous Positive Ions, NSRDS-NBS 26 (U. S. GPO, Washington, D.C., 1969).

50. D. H. Aue and M. T. Bowers, in Gas Phase Ion Chemistry, edited by M. T. Bowers (Academic Press, New York, 1979), Vol. 2, p. 1.

51. F. P. Lossing and J. C. Traeger, J. Am. Chem. Soc. 97, 1579 (1975).

52. F. P. Lossing, Can. J. Chem. 50, 3973 (1972).

53. J. C. Schultz, F. A. Houle, and J. L. Beauchamp, J. Am. Chem. Soc. 106, 7336 (1984).

54. S. W. Benson and H. E. O'Neal, Kinetic Data on Gas Phase Unimolecular Reactions, NSRDS-NBS 21 (U.S. GPO, Washington, D.C., 1970).

55. W. v. E. Doering, Proc. Natl. Acad. Sci. U.S.A. 78, 5279 (1981).

56. D. F. McMillen and D. M. Golden, Annu. Rev. Phys. Chem. 33, 493 (1982).

57. The exit potential energy barrier of a reaction, such as $C_3H_6^+ + C_3H_6 \longrightarrow C_4H_7^+ + C_2H_5$ is defined to be the height of the potential energy barrier between stable $C_6H_{12}^+$ complexes and $C_4H_7^+ + C_2H_5$ measured with respect to the stability of $C_4H_7^+ + C_2H_5$.

58. C. D. Wagner, Tetrahedron 14, 164 (1961).

59. W. A. Lathan, W. J. Hehre, and J. A. Pople, J. Am. Chem. Soc. 93, 808 (1971).

60. The intensity for $C_3H_7^+$ is less than 5% that of $^{13}C^{12}C_2H_6^+$.

61. Ono et al. (Ref. 20) have pointed out that the failure to observe cluster ions higher than the dimer ion does not rule out the presence of trimers in the supersonic beam if the dissociative ionization channel is an efficient one. The results of photoionization samplings of the C_2H_2 (Refs. 21 and 22), C_2H_4 (Ref. 20), C_3H_6, and c-C_3H_6 supersonic beams suggest that, by far, the most efficient fragmentation channel for a trimer ion is the formation of a dimer ion and a neutral monomer. It is unlikely that the C_6H_{11} ions observed here are produced from $(c\text{-}C_3H_6)_3^+$.

62. L. Friedman, F. A. Long, and M. Wolfsberg, J. Chem. Phys. 26, 714 (1957); 27, 613 (1957).

63. W. A. Chupka, J. Chem. Phys. 30, 191 (1959).

64. M. L. Gross, Org. Mass Spectrom. 6, 827 (1972).

65. C. Lifshitz, A. M. Peers, M. Weiss, and M. J. Weiss, Adv. Mass Spectrom. 6, 871 (1974).

66. S. M. Gordon and N. W. Reid, Int. J. Mass Spectrom. Ion. Phys. 18, 379 (1975).

PART II. PHOTOFRAGMENT DYNAMICS STUDY OF CARBON DISULFIDE BY HIGH RESOLUTION MOLECULAR BEAM LASER PHOTOFRAGMENT TIME-OF-FLIGHT MASS SPECTROMETRY

Introduction

The study of photodissociation of small molecules is important for both practical and theoretical reasons.[1] From practical point of view, knowledge of the dissociation products, and the energy distribution in those products, is necessary in order to understand any processes in which the products may participate in successive collisions. Such information is useful in understanding and modeling diverse problems such as laser chemistry and the composition and kinetics of planetary atmospheres.[2-4] On the other hand, from the theoretical viewpoint, the product state distribution is a sensitive probe of the electronic structure of the excited state as well as the dynamics of nuclear motion. With the development of theoretical models[5] for treating the dynamics of photodissociation, it will become realistically possible to compare calculated distributions with measured ones and thus produce empirical potential energy surfaces for molecular excited states.

Photodissociation is the result of the interaction of incident light (electromagnetic wave) with a molecule. Depending upon the energy transferred to the molecule, there are many types of photodissociation processes. In general, photodissociation processes may be classified into two categories: direct and indirect photodissociation.

If the excitation photon energy is large when compared with the minimum energy needed to excite metastable vibronic levels of the molecule, direct dissociation processes will generally dominate. Therefore, when a molecule which has no quasibound levels in the energy region is excited by a high frequency photon, it dissociates directly into continuum states. Each of such continuum states may be specified by the electronic structure, the vibrational and rotational quantum numbers and the relative kinetic energy of the fragments.

Indirect photodissociation involving two steps is a more complicated process. Upon photoabsorption a molecule may be excited to an intermediate (metastable) level which is degenerate with a continuum level or many continua. The excited molecule in the metastable state will then undergo a radiationless transition process and dissociate into product fragments. This photodissociation phenomenon may occur due to interaction between the metastable and the continua belonging to different electronic states as well as through interconversion of vibrational to translational energy on a single potential energy surface.

The indirect photodissociation processes of polyatomic molecules may be further classified:[6] (1) predissociation by electronic transition — where the dissociation continuum that causes radiationless decomposition belongs to another electronic state; the predissociation is accompanied by a change in the potential energy surface, (2) predissociation by vibration — where the dissociation continuum belongs to the same electronic state but joins on to a lower dissociation limit;

the predissociation is a result of vibrational energy redistribution, and (3) predissociation by rotation — where the dissociation continuum belongs to the same electronic state and the same series of vibrational levels; the predissociation is caused by an energy transformation from rotational to vibrational motion.

The process of photofragmentation can be viewed as a "half-collision" event,[7-9] where the system is prepared in a specific state or superposition of states by photoabsorption and is followed by the halfcollision event in which translational, vibrational and rotational energy transfer may occur. The photofragment spectroscopy yields information on final state distribution, excited state symmetries, product angular distributions and translational energy distributions.

Since the suggestion of Kantrowitz and Grey[10] in 1951, supersonic nozzle sources have been used to produce intense molecular beams with narrow velocity distribution (well defined translational energies) in a collisionless condition. With new high power UV lasers and highly sensitive ion detection devices, the time-of-flight (TOF) technique is a promising candidate for studying photofragmentation dynamics.

Busch et al.[11] first constructed a photofragment spectrometer for studying the dynamics of molecular photofragmentation of simple polyatomic molecules.[12-15] Dzvonic and Yang[16] also built a similar continuous wave photofragment spectrometer for investigating photodissociative reactions of large aromatic polyatomics. A few years later, another TOF photofragment spectrometer was completed by Shinohara and co-workers[17-18] for studies of the laser photofragmentation dynamics

of medium size organic molecules. In all these machines the laser propagation direction, molecular beam source direction and detector direction are mutually perpendicular to one another. The disadvantage of such design is that fragments recoiling slowly from a fast molecular beam will not enter the detector. To overcome this problem, Sparks et al.[19] applied the idea of a rotatable detector universal crossed beam machine[20] and constructed a laser photofragment spectrometer with rotatable detector. With all these previous designs in mind, a newer version of a molecular beam laser photofragment mass spectrometer with a rotatable beam source and a movable detector has been built for studying the photofragmentation dynamics of small polyatomic molecules. This machine not only has the improvements of the Sparks and Lee machine, but also has the advantage of changeable flight path for higher velocity analysis resolution. A rotating beam source TOF photofragmentation mass spectrometer with a similar design has been reported recently by Wodtke and Lee.[21]

As the first operational diagnostic of the new machine, a TOF chopper wheel experiment has been performed using argon as a model gas for molecular beam characteristics studies. In addition, the initial velocity of the CS_2 molecules in the laser photofragmentation study has been measured with the same setup.

Because of its high vapor pressure at normal conditions and its spectroscopic properties, (CS_2) was chosen as the first model system for the laser photofragmentation dynamics study using this apparatus. The machine has demonstrated its two outstanding features of rotatable

molecular beam source and movable detector, and that these features are important for angular distribution experiments and for high resolution molecular beam laser photofragment TOF experiments.

References

1. W. M. Gelbart, Annu. Rev. Phys. Chem. 28, 323 (1977).
2. W. M. Jackson, Mol. Photochem. 4, 135 (1972).
3. W. M. Jackson, J. Photochem. 5, 107 (1976).
4. M. Oppenheimer, Acc. Chem. Res. 13, 378 (1980).
5. M. Shapiro and R. Bersohn, Annu. Rev. Phys. Chem. 33, 409 (1982).
6. G. Herzberg, The Spectra and Structure of Simple Free Radicals (Cornell University Press, Ithaca, New York, 1971).
7. S. Mukamel and J. Jortner, J. Chem. Phys. 60, 4760 (1974); 61, 5348 (1975); 65, 3735 (1976).
8. J. A. Beswick, M. Shapiro, and R. Sharon, J. Chem. Phys. 67, 4045 (1977).
9. O. Atabeck and R. Lefebvre, J. Chem. Phys. 67, 4983 (1977).
10. A. Kantrowitz and J. Grey, Rev. Sci. Instrum. 22, 328 (1951).
11. G. E. Busch, J. F. Cornelius, R. T. Mahoney, R. I. Morse, D. W. Schlosser, and K. R. Wilson, Rev. Sci. Instrum. 41, 1066 (1970).
12. G. E. Busch and K. R. Wilson, J. Chem. Phys. 56, 3626, 3638, 3655 (1972).
13. R. D. Clear and K. R. Wilson, J. Mol. Spectrosc. 47, 39 (1973).
14. R. J. Oldman, R. K. Sander, and K. R. Wilson, J. Chem. Phys. 63, 4252 (1975).
15. J. H. Ling and K. R. Wilson, J. Chem. Phys. 63, 101 (1975).
16. M. J. Dzvonik and S. Yang, Rev. Sci. Instrum. 45, 750 (1974).
17. H. Shinohara, and N. Nishi, J. Chem. Phys. 77, 234 (1982).

18. N. Nishi, H. Shinohara, and I. Hanazaki, J. Chem. Phys. 77, 246 (1982).

19. R. K. Sparks, K. Shobatake, L. R. Carlson, and Y. T. Lee J. Chem. Phys. 75, 3838 (1981).

20. Y. T. Lee, J. D. McDonald, P. R. LeBreton, and D. R. Herschbach, Rev. Sci. Instrum. 40, 1402 (1969).

21. A. M. Wodtke and Y. T. Lee, J. Phys. Chem. 89, 4744 (1985).

SECTION I. THEORY

The energy partitioning theory of photofragment TOF spectroscopy is relatively simple.[1,2] Upon absorption of photons the parent molecules are excited to a dissociative excited state and then dissociate into fragments. The product fragments recoiling out of the scattering volume may have translational energy of recoil and internal energy in the form of electronic excitation. In addition, the molecular fragments may be rotationally and vibrationally excited.[3,6]

By conservation of energy in the c.m. system, E_{avl}, the total available energy to be partitioned between E_{trn} (the total c.m. translational energy of both fragments) and E_{int} (the total internal energies of both fragments) can be expressed as

$$E_{avl} = E_{trn} + E_{int} = E_{par} + h\nu - D_o^o$$

in which E_{par} is the total internal energy of the parent molecule, $h\nu$ is the energy of the absorbed photon, D_o^o is the dissociation energy of the ground state parent molecule to ground state fragments (atoms or molecules).

E_{trn}, the total center-of-mass (c.m.) translational energy for both fragments, can be obtained from the flight time of one of the fragments through conservation of momentum by a transformation involving the flight path length l, the initial velocity of the parent molecule u, and the fragment masses m_A and m_B. (See Appendix D.) The total internal (electronic, vibrational, and rotational) energy of both recoiling

fragments, E_{int}, may be obtained by subtracting E_{trn} from E_{avl}, the total available c.m. energy.

References

1. G. E. Busch and K. R. Wilson, J. Chem. Phys. 56, 3626 (1972).

2. R. T. Mahoney, Ph. D. Dissertation, University of California, San Diego, La Jolla, CA 92037, 1971.

3. R. C. Mitchell and J. P. Simons, Disc. Faraday Soc., 44, 208 (1967).

4. M. N. R. Ashfold and J. P. Simons, J. Chem. Soc. Faraday II 73, 858 (1977).

5. S. A. Rice, Dynamics of Primary Photochemical Processes in Excited States, edited by E. C. Lim (Academic Press, New York, 1975), Vol. 2, pp. 111-320.

6. J. P. Simons, The Dynamics of Photodissociation in Gas Kinetics and Energy Transfer (Chem. Soc. Spec. Periodical Reports, 1977), Vol. 2, p. 56.

SECTION II. THE MOLECULAR BEAM LASER PHOTOFRAGMENT TIME-OF-FLIGHT MASS SPECTROMETER

Introduction and Design Considerations

In the past thirty years since Taylor and Datz built the differential detection beam apparatus[1] many molecular beam machines have been constructed for elastic, inelastic, or reactive scattering studies of chemical systems. They all fall into two categories: (1)rotatable source configuration,[2-6] and (2) rotatable detector configuration.[7-9] Early rotatable source type machines, using effusive ovens attached to a single rotatable lid, suffered from a low beam intensity due to lack of extensive differential pumping in the beam generating system. However, the rotatable detector machines have fixed beam interaction angle of 90 degrees and fixed distance between scattering center and detector. Therefore, for cross-beam experiments the change in relative velocity of the collisional partners must rely on heated and/or seeded beam[10] arrangements. After reviewing the designs of some rotatable detector type machines, Prest[11] pointed out the advantages and disadvantages of them and suggested that a rotatable beam source machine with a movable detector is a newer generation apparatus for crossed molecular beam experiments.

The main goal for the design of this molecular beam laser photofragment time-of-flight (MB-LP-TOF) mass spectrometer is to utilize the idea of the rotatable beam source with a movable detector and recent advancement of high power vacuum ultraviolet laser. The machine is

designed to be as versatile as possible in order to be modified easily for more advanced experiments in the future.

Beam source considerations

The molecular beam source generation system must be able to produce an intensive supersonic beam and yet be rotatable for angle-related beam experiments. The angle of the molecular beam source can be set by invoking an executable command in the LASER MCS unit (Appendix A) or by manually rotating the beam source generation unit through a mechanical device. A mechanical drum dial is needed to serve as a redundant indicator of the beam source angle in case of operational failure of the multichannel scaler.

The range of the beam source angles must be reasonably large for presently designed experiments and may be enlarged further by replacing the beam source top head for future experiments such as back scattering beam experiments.

Detection system considerations

The detection system is required to have high detection sensitivity to measure low signal levels of the desired experiments and to have movable capability to achieve high TOF resolution. These requirements are essential in order to minimize the noise level caused by background gas in the detector chamber and to be able to change flight path length according to desired experiments.

The detection system needs to be well aligned with the beam source system, so that the flight path length may be changed by simply replacing the intermediate tube which is placed between the detector chamber and the scattering chamber. The intermediate section between the detector chamber and the scattering chamber functions not only as a means for varying flight path length (by using stainless steel tubes and flexible bellows of various lengths), but also as an expansion port for more advanced and complicated experiments in the future.

The newly constructed molecular beam laser photofragment time-of-flight mass spectrometer (MB-LP-TOF) consists of the following major parts: (1) a sophisticated differentially pumped vacuum system, (2) a rotatable nozzle beam generation system, (3) an excimer laser, and (4) a movable detection system. Figure 1 and Figure 2 are the horizontal and vertical cross section views of this MB-LP-TOF machine. More than 200 detailed original machine drawings[12] for important components have been filed by number LIFTOF-XXX-NN into five groups classified as Assembly (ASM), Beam Source Chamber (BSC), Main Chamber (MCH), Detector Chamber (DET), and Miscellaneous (MIS). Only the essential parts of the machine will be described.

Differentially Pumped Vacuum System

The sophisticated differentially pumped vacuum system, consisting of a source part and a detector part, utilizes extensive pumping capability. The source part generates a well-collimated, intensive, supersonic molecular beam and contains the photofragmentation reaction

Figure 1. Horizontal cross section view of the MB-LP-TOF machine.

AF -- adaptor flange.

BC -- nozzle discharge chamber.

BT -- liquid nitrogen beam catcher.

DR -- collimation chamber.

EI -- electron bombardment ionizer.

FM -- fragment molecules.

GV -- 8" gate valve.

IC -- ionization chamber.

IL -- ion exit lenses.

LB -- laser beam.

LR -- liquid nitrogen cold ring.

MB -- molecular beam axis.

MC -- scattering chamber.

NZ -- molecular beam nozzle.

QF -- quadrupole mass filter.

RA -- beam source rotational axis

RV -- scattering center.

SH -- rotational driving tubular shaft.

TP -- to turbomolecular pump.

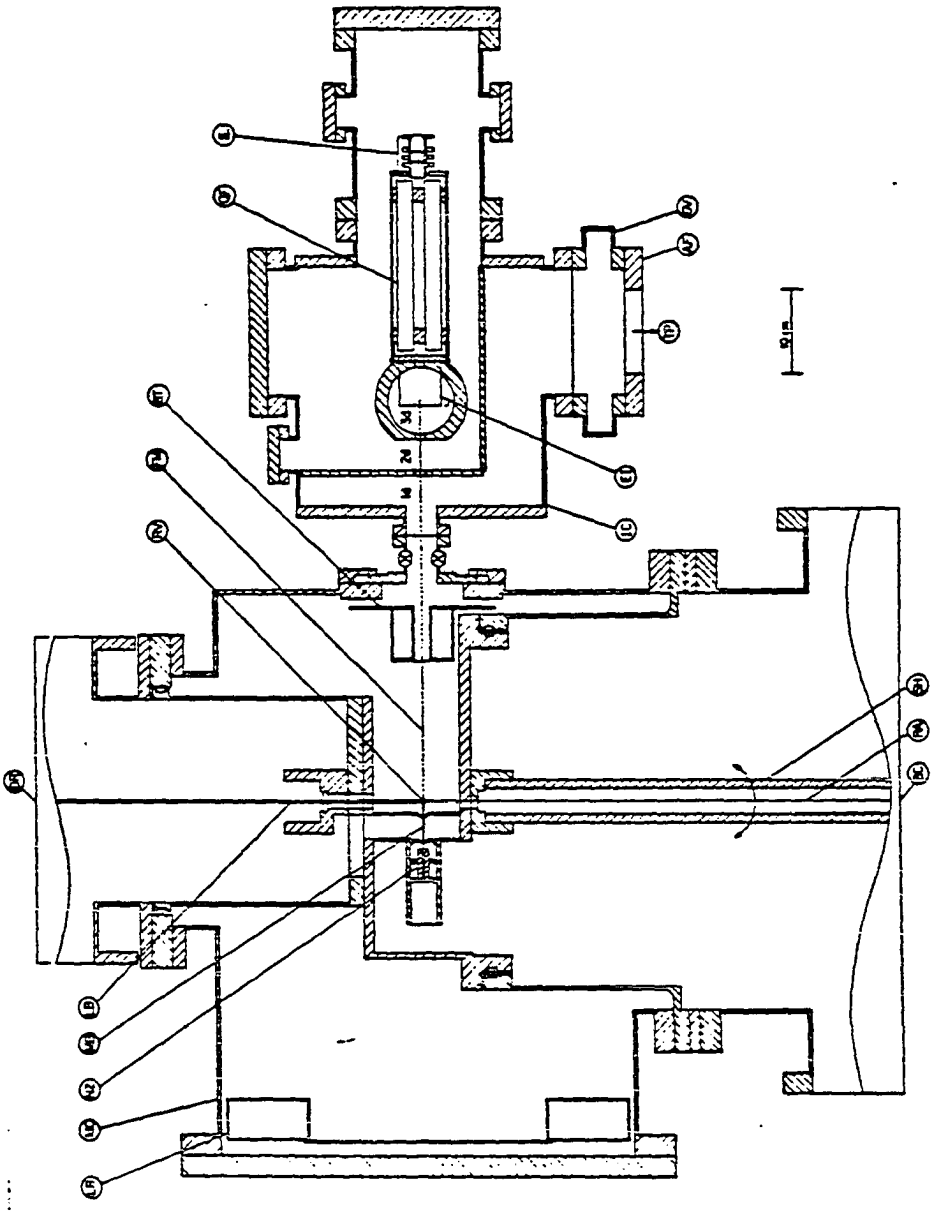

Figure 2. Vertical cross section view of the MB-LP-TOF machine.

BC --- nozzle discharge chamber.
BT --- liquid nitrogen beam catcher.
CP --- to veeco ion pump.
DB --- dumbell ion target.
DC --- ion detection chamber.
DP --- to 10" diffusion pump.
DR --- collimation chamber.
EI --- electron bombardment ionizer.
FM --- fragment molecules.
FT --- 33 kV electrical feedthrough.
IC --- ionization chamber.
IL --- ion exit lenses.
IP --- to ultek ion pump.
LR --- liquid nitrogen cold ring.
MB --- molecular beam axis.
MC --- scattering chamber.
NZ --- molecular beam nozzle.
PM --- photomultiplier holder.
QF --- quadrupole mass filter.
RP --- beam source rotational baseplate.
RV --- scattering center.

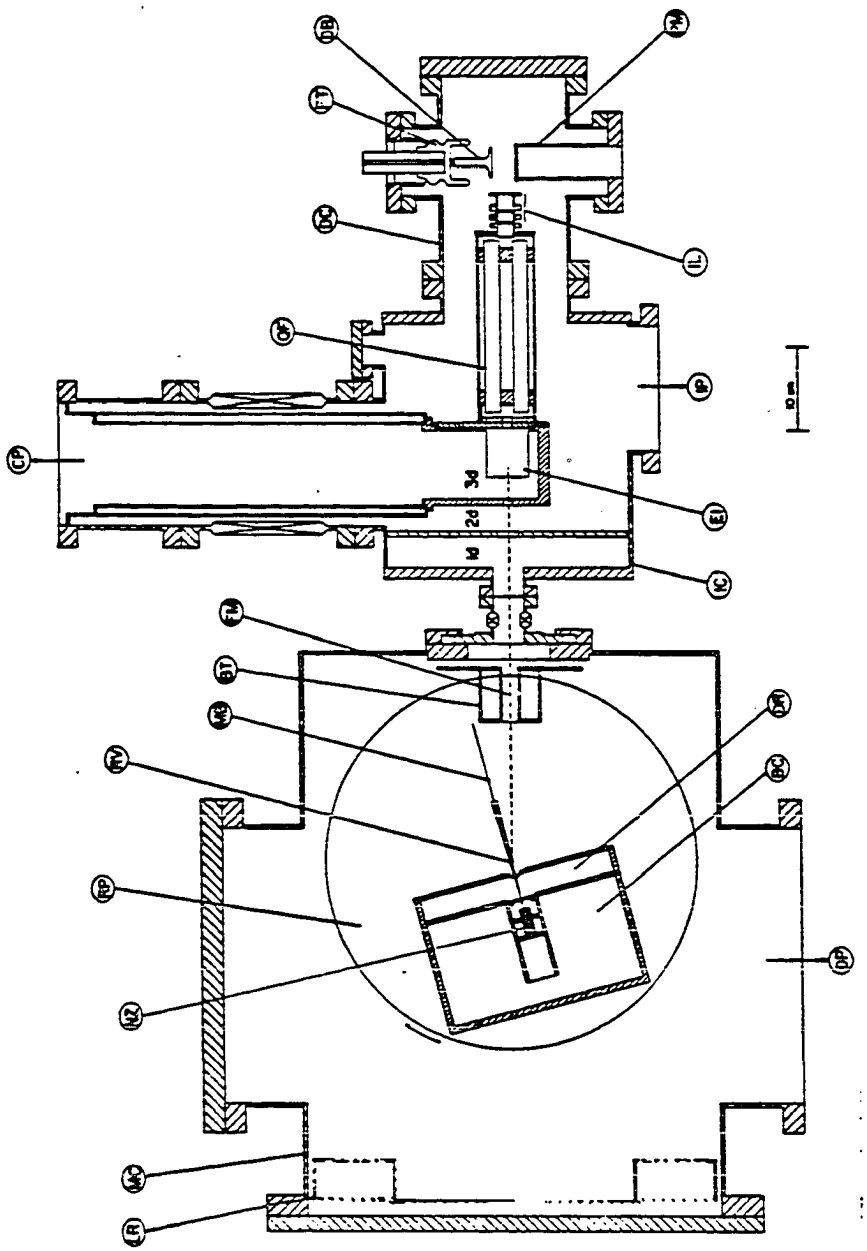
3d
2d
d

volume. It is a differentially pumped unit with three components: nozzle discharge chamber, collimation chamber, and scattering chamber. The detector part minimizes the partial pressure of background gas and achieves high detection efficiency. It is also a bakable differentially pumped unit.

The nozzle discharge chamber houses a gas supply line, a supersonic beam nozzle, and a skimmer. This chamber collects the fraction of the nozzle flow which does not pass through the skimmer. A 20" oil diffusion pump (Varian model HS-20) with a rated ultimate pumping speed of 17,500 l/s is used to evacuate the nozzle discharge chamber. In order to reduce backstreaming without reducing the pumping speed greatly, a water-cooled Halo baffle[13] is employed. This Halo baffle utilizes the standard cold cap of the diffusion pump and an additional water-cooled chevron to intercept backstreaming gases emanating from the top nozzle. As a result, it eliminates 90% of the backstreaming not intercepted by the cold cap, and still retains 60% of the pumping speed.

To match the throughput of the 20" diffussion pump and to achieve its maximum performance, a Stokes[14] model 150-4 4" Ring Jet Booster pump together with a Leybold-Heraeus[15] model D60A Trivac two-stage rotary vane pump with a rated pumping speed of 36.7 CFM is used as the backing pump. During normal operation the pressure in the nozzle discharge chamber is maintained at $< 1 \times 10^{-4}$ Torr.

The collimation chamber has a reasonably large flow conductance and a pressure about an order of magnitude lower than that of nozzle discharge chamber. It is pumped by a liquid nitrogen trapped 6" oil

diffusion pump (Varian model VHS-6) through an aluminum gate valve. The pumping speed of this 6" diffusion pump system is estimated to be 950 l/s. A Leybold-Heraeus model D30A Trivac two-stage rotary vane pump with a rated pumping speed of 26.8 CFM is used as the foreline backing pump for both the collimation and the scattering chambers.

The scattering chamber is where the molecular beam is perpendicularly crossed with the laser beam and where the photofragmentation reaction takes place. A 10" oil diffusion pump with an accompanying gate valve and a Varian model 330 freon-cooled baffle[16] attains an estimated pumping speed of 1830 l/s and maintains a pressure of 10^{-7} Torr during normal operation. A liquid nitrogen cold ring and a cold beam catcher have been installed in this scattering chamber in order to lower the background pressure for condensable gases and thus reduce the attenuation of product fragments by the background gas. A pressure of 10^{-8} Torr is easily maintained in this chamber during normal photofragmentation experiments.

The first differentially pumped section in the bakable detector chamber is pumped by a Balzers[17] Model TPU 330 turbomolecular pump with a pumping speed of 330 l/s. A Varian Model HeS 2" diffusion pump backed by a Leybold-Heraeus D8A Trivac two-stage rotary vane pump maximizes the performance of the turbomolecular pump.

A home-made turbomolecular pump control and a 6" electropneumatic swing gate valve[18] are employed with the turbomolecular pump to protect the detector chamber in case of accidental vacuum failure. The electropneumatic gate valve will be closed and the turbomolecular pump

will be shut off if (1) the turbomolecular pump is not running properly, e.g. not at full rotational speed, (2) there is not sufficient cooling water for the turbomolecular pump, or (3) the foreline pressure of the turbomolecular pump is too high.

An aperture disc mount has been placed between first and second differentially pumped regions in the detector chamber. Since this aperture disc mount has a mechanical keyway, the replacement and alignment of aperture discs can be done easily. Using an aperture disc of 1/8" diameter, a pressure difference between these two regions is about an order of magnitude. The total pressure in this section is normally maintained at 10^{-8} Torr.

The quadrupole mass filter and Daly ion detection unit are located in the second differentially pumped region of the detector chamber. A Cryo-Boostivac D-I combination pump (Ultek Model 224-0620) consisting of a differential ion pump and and a titanium sublimation pump with a pumping speed of 150 l/s is used as trap for the straight through molecules from the scattering chamber. A turbomolecular pump (Balzers Model TPU 050) with a pumping speed of 50 l/s is also employed in this section to keep the pressure at 10^{-9} Torr during normal operation.

The innermost region of the detector chamber houses an electron bombardment ionizer and is pumped by a Veeco 100 l/s noble gas ion pump (Veeco Model PN-201) and a liquid nitrogen cold trap working as a cryogenic pump. The total pressure in this innermost region is maintained at 10^{-10} Torr or less during normal experiments.

Rotatable Supersonic Beam Source System

One of the most important components in the rotatable supersonic beam generation system is the beam source top head whose cross section view is shown in Figure 3. The beam source top head (LIFTOF-BSC-05) houses the source nozzle, skimmer and collimator pieces and is mounted on the beam source inner chamber (LIFTOF-BSC-01) with an inner bearing retainer (LIFTOF-BSC-02), an outer bearing retainer (LIFTOF-BSC-03), and a top-inner bearing retainer (LIFTOF-BSC-04) through the "X" contact of a 16" I.D. Kaydon Reali-Slim type X ball bearing.[19] A detailed cross section view of the bearing, its retaining components and the beam source top head for this rotational mechanism is shown in Figure 4. The seal which ensures a pressure difference between chambers in the static condition and no pressure change in each chamber during rotational motion of the beam source top head is a 16" I.D. x 3/16" wall O-ring.[20]

All bearing retaining pieces are precisely machined to give the best performance of the ball bearing and to eliminate problems that may be caused by improper use of the O-ring. The edges of these machined pieces are chamfered for easier assembling. The rotational motion of the beam source top head is slow (about 1 degree/second) and a 3-5% compression O-ring with good lubrication meets the above design criteria.

The beam source top head is coupled through the tubular shaft holder (LIFTOF-BSC-16) to a 2" O.D. tubular harden steel shaft[21] which extends out of the vacuum chamber (shown in Figure 1). A mechanical handle, a 100-tooth gear[22], and a drum dial angle indicator[23] are

Figure 3. Beam source top head.

1. 3/4" thick x 18" O.D. 304 stainless steel (to mount on Top-Inner Bearing Retainer).
2. 5/8" thick 304 stainless steel for mounting differential chamber can.
3. 1/4" thick 304 stainless steel for mounting back plate.
4. 1/8" thick 304 stainless steel for mounting nozzle/ skimmer holder.
5. 1/8" thick 304 stainless steel for mounting collimator.

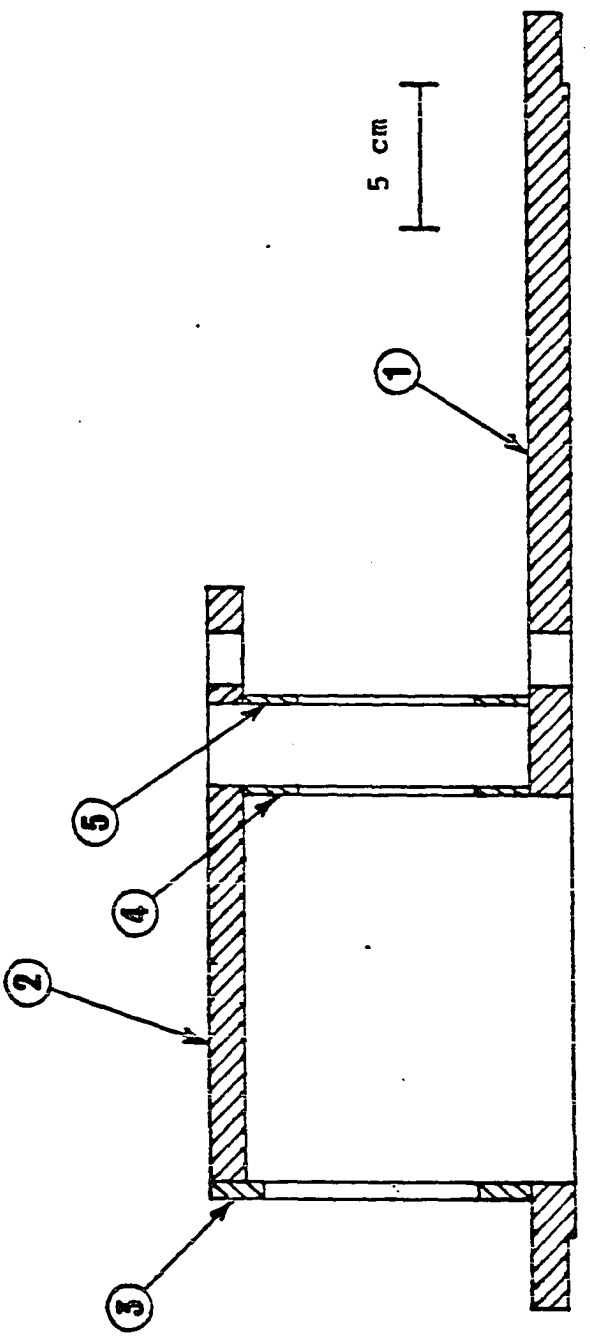
5 cm
1
2
3
4
5

Figure 4. Cross section view of beam source rotating seal.

1. beam source inner chamber.
2. inner bearing retainer.
3. outer bearing retainer.
4. top-inner bearing retainer.
5. beam source top head.
6. 16" I.D. Kaydon bearing.

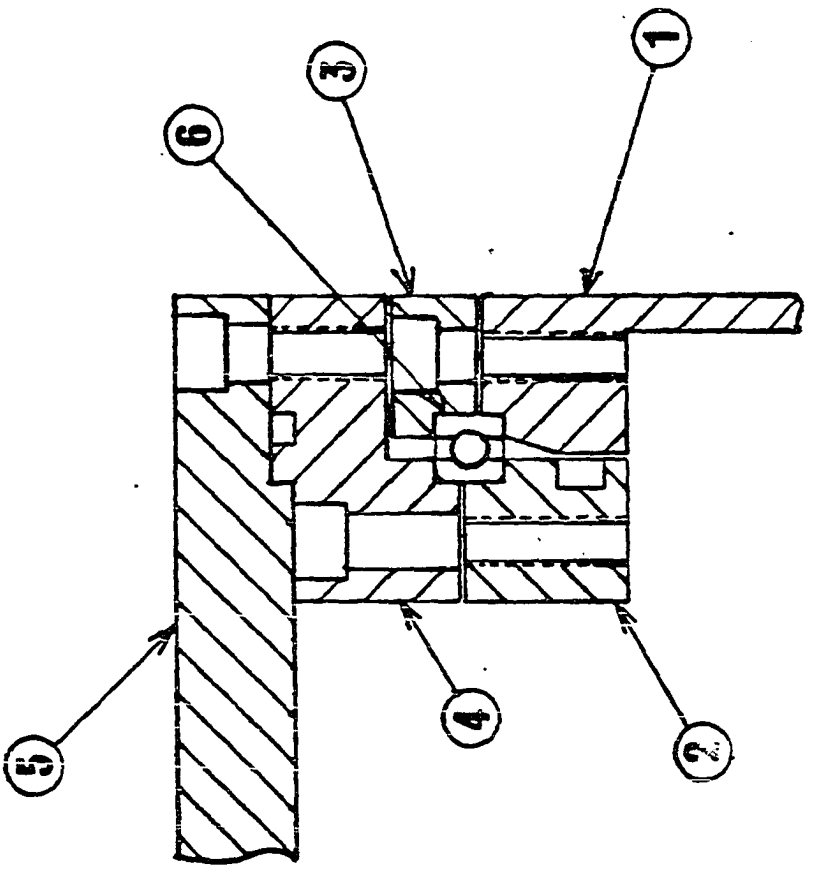
1
3
6
5
4
2

mounted on the section of this tubular shaft which is outside of vacuum chamber. This simple mechanical handle provides a means for manual operation of the beam source rotation. The drum dial angle indicator has been calibrated and shows the beam source angle with respect to the detector direction.

On the opposite side of nozzle discharge chamber, a 10" O.D. differential chamber can (LIFTOF-BSC-06) is mounted on the top of the beam source top head. This differential chamber can ensures a pressure difference between the collimation chamber and the scattering chamber and provides a reasonably large conductance for pumping. Owing to proper sealing and careful assembling this differential chamber can rotates with the beam source top head without creating any problems, such as pressure variation in vacuum chambers or increase in rotational friction.

A computer controlled rotation driving mechanism has been designed. The mechanism uses a stepping motor and a gear set. The following procedure has been applied to choose the proper gear set and found to be successful:

1. Estimate the torque needed to move the object. The torque for rotating the beam source top head is about 600 lb-in (9600 oz-in).
2. Select a stepping motor that can be interfaced to the existing computer and note how much torque it can supply. The chosen SLO/SYN synchronous/stepping motor[24] can supply a torque of 1125 oz-in.
3. Calculate the torque ratio. R = 9600 / 1125 = 8.5

4. Set a safety factor of at least four, and determine the gear ratio required (torque ratio times the safety factor).
5. Examine the mounting considerations and decide the gear type.

Since the SLO/SYN motor is interfaced to the Motorola 6809 microprocessor which is the LASER MCS system host computer, the beam source rotational motion can be done by invoking the MOVE master command in the main command menu of the LASER MCS system. (See Appendix A for detailed software description.) The range of the beam source rotational motion has been set internally in the programming code of the 6809 processor. According to the present calibration the central axis of the detector is set to be the reference axis and the angular range of the beam source rotation is between -90 and +90 degrees. In principle, the angle = 0 degree when the reference axis coincides with the molecular beam source axis. The angular resolution determined by both the SLO/SYN motor and the 6809 processor is 0.1 degree.

In addition, a mechanical device with a microswitch compensates for any accidental failure of the LASER MCS operation. In case that the beam source chamber mechanically goes beyond the preset range, the LASER MCS control unit will be turned off through the microswitch interlock. Consequently, the rotational motion is terminated immediately.

The procedure for determining the molecular beam source axis is as follows:

1. Set up a cathetometer and make sure it is leveled.
2. Set the beam source at approximately 0 degree (angle on drum

dial indicator = 0) and insert an alignment pin in the molecular beam nozzle holder so that it points to the cathetometer.

3. Adjust the angle setting on the cathetometer and focus on the tip of the alignment pin.
4. Rotate the beam source to 180 degrees and reverse the alignment pin so that it is still pointing to the cathetometer.
5. Focus on the tip of the alignment pin and note the position with respect to the reference cross hair on the cathetometer.
6. Move the base of the cathetometer in the proper direction (either left or right).
7. Check the leveling bubble on the cathetometer and adjust the base of the cathetometer if necessary.
8. Rotate the beam source back to 0 degree and reverse the alignment pin again to let it point to the cathetometer.
9. Repeat steps 3-8 until they agree. Thus, the vertical plane is defined but the horizontal height is yet to be defined.
10. Set the beam source at 0 degree and remove the alignment pin.
11. Adjust the vertical bubble on the cathetometer until 2 halves of the circle become one.
12. Insert a secondary alignment pin in the center hole of the beam source top head.
13. Focus on the tip of the secondary alignment pin and note the position of the pin with respect to the reference cross hair on the cathetometer.
14. Focus the cathetometer on the reference line defined previously

on the inner wall of the chamber port of the scattering chamber.

15. Repeat steps 11-14 until both agree. Then the horizontal reference is defined.
16. Use a fine tip diamond scriber to mark a thin line on the side of both beam source top head and the stationary base plate. This scribed line serves as a calibration reference for molecular beam source angle = 0 degree.
17. Set the drum dial indicator angle = 0 degree.

The true 0 degree has been precisely determined by a TOF chopper wheel experiment. The setup for the experiment is described in the section of the Initial Tests and Operations. The signal coming out of mass spectrometer has been recorded for each angle as the source beam has been changed from -2.0 to +2.0 degrees in 0.1 degree increments. As a result, the maximum signal has been found at +0.9 degree. Therefore, the true true 0 degree is +0.9 degree in the mechanical setting.

Gas inlet system

The gas inlet system has been assembled to provide a quick changeover from one gas to another through the use of a Wallace & Tiernan gauge[25] and proper control regulators.[26] A replacement element filter[27] and a stainless steel flexible hose have been installed to ensure a pure gas flow from the supply reservoir to the molecular beam nozzle without being damaged due to beam source rotational motion.

Molecular beam nozzle and skimmer

A high molecular beam intensity may be obtained by the use of contoured or slit-type nozzles as discussed by Hagena and Morton.[28] However, in such arrangements condensation occurs at large source Knudson numbers (related to nozzle stagnation pressure and nozzle diameter) due to a reduction of all flow field gradients. The source Knudson number is proportional to the nozzle diameter for a given mass flow through the nozzle. Therefore, one expects to obtain a higher speed ratio and intensity of a molecular beam when using a smaller diameter nozzle. The lower limit of the nozzle diameter is governed by the onset of condensation in the beam gas and the optimum nozzle size depends on the nature of the beam gas.[29,30]

In the present operation of a room temperature nozzle, the nozzle piece has been designed to take advantage of using commercially available aperture discs of many sizes and materials.[31] Since a Viton O-ring is used in the seals, the nozzle can be heated to 200 C to prevent clogging in the nozzle opening or to vary the beam conditions. A heater wire, wrapped with ceramic beads for good electrical insulation, and a chromo-alumo thermocouple wire are installed on the nozzle to permit temperature adjustments and measurements.

The skimmer, a very important element for successful performance of a supersonic beam generation system, is made of stainless steel and has a small external angle and a sharp edge. The object of the proper skimmer design[29,32] is: (1) to avoid shock waves formed in front of the skimmer, and (2) to minimize skimmer interaction with the flow upstream

and downstream from the skimmer entrance, which adversely affects both the intensity and the speed ratio of the resultant beam. Therefore, the skimmer external angle must be small in order to reduce the number of molecules reflected from the outer wall which can disturb the nozzle flow; whereas the skimmer internal angle has to be large to minimize collisions of beam molecules with the inner wall of the skimmer. With these considerations in mind, the skimmer has been made with internal and external cone angles of 70 and 80 degrees, respectively.

The optimum molecular beam intensity is a function of nozzle-skimmer distance for a given nozzle diameter.[33] To achieve this maximum beam intensity for a particular configuration, a nozzle-skimmer distance is normally set to be 50-100 times the nozzle diameter. In most experiments the nozzle-skimmer distance has been set to be 60 times the nozzle diameter. A typical nozzle-skimmer setup may be seen in Figure 1.

By varying the nozzle conditions, i.e., stagnation pressure, nozzle diameter and nozzle-skimmer distance, one can produce an intensive molecular beam for desired experiments. For example, for a room temperature argon beam at a stagnation pressure of 1 atm, a nozzle diameter of 0.005" and a nozzle-skimmer distance of 0.300", the molecular density in the scattering volume is about 2×10^{13} molecules/cm^3. (See Appendix B for detailed calculation.)

The Excimer Laser

Since they were discovered in 1975,[34-39] rare gas halide excimer lasers have proved to be a powerful ultraviolet light source for photochemistry studies and many other applications. A Questek[40] Model 2260 multigas excimer laser is used as the photofragmentation light source in the MB-LP-TOF mass spectrometer.

The detailed kinetics of energy transfer in excimer lasers are very complex and not yet fully understood. However, It has been found that ArF (193nm), KrF (249nm), XeCl(308nm), and XeF(351nm) exhibit intense laser output at a total pressure of the gas mixture of a few atmospheres.[41] The gas mixture contains: (1) halogen donor (e.g., molecular fluorine or hydrogen chloride) in concentration of 0.5% or less, (2) rare gas (e.g., argon, krypton, or xenon) that combines with the halogen to form excimer molecules in a concentration of 0.5% to 12%, and (3) buffer gas (e.g., helium or neon) which serves as the energy transfer medium in a concentration of 88% to 99% of the total pressure. In the present applications of the ArF excimer laser, the "fuel gas" components in the gas mixture are as follows: (1) 0.3% of molecular fluorine as halogen donor, (2) 9.6% of argon as rare gas, (3) 50.7% of helium as buffer-A gas, and (4) 35.4% of neon as buffer-B gas.

The Questek multigas excimer laser generates four intense laser lines of different frequency photons depending upon the fuel gases. These four output laser lines are ArF(193nm), KrF(248nm), XeCl(308nm) and XeF(351nm). Currently, the ArF laser is used as the light source in the laser photofragmentation experiments. The supply fuel gases for ArF

laser operations are 5% F_2/He (which is 5% molecular fluorine in helium for safety reasons) as halogen gas (170 mbar), argon as rare gas (260 mbar), helium as buffer-A gas (1305 mbar), and neon as buffer-B gas (955 mbar). Since the purity of each supply gas is essential to laser power, all supply fuel gases used are of high purity grades, e.g., research grade (99.9995% purity), or ultrahigh purity grade (99.999% purity).[42]

In general, there are two types of contaminations which shorten the fuel gas lifetimes. Particulate contaminants are significant in the operations of XeCl and KrF lasers. However, the particulates can be easily removed by installing a mechanical microfilter. A wafergard F In-line Filter[43] has been installed in the gas circulation line of the excimer laser. Gaseous contaminants can be removed only by cryogenic trapping or chemical processing. Of the two methods for treating the gaseous contaminants, one quickly finds that cryogenic processing is simpler and more economical. In the ArF and KrF applications, treatment of the gaseous contaminants is a "must". The Questek Inc. offers the Oxford GP 2000 temperature-controlled cryogenic gas processor as an option for their excimer lasers. However, a simple vacuum line trap accompanied by a liquid nitrogen chicken feeder has been built and installed in the gas circulation line of the excimer laser. It has been found that the home-made liquid nitrogen trap substantially extends the fuel gas lifetimes.

The most commonly used materials for excimer laser optics are VUV-grade MgF_2 and CaF_2, and high quality UV-grade fused silica, such as Suprasil[44] and Corning[45] 7940 D1 because of their high transmission in

the wavelength region below 200 nm. However, the excimer laser cavity coupling optics are normally made of MgF_2 to resist corrosion of halogen gases in the gas mixture chamber.

Since the atmosphere strongly absorbs the vacuum ultraviolet radiation (largely due to the formation of ozone), the laser beam intensity is attenuated as it travels through air. To solve this problem, one may set up a mechanical device to pump out the air in a well-sealed laser path section. However, this normally presents a difficulty in sealing the whole region, including the laser chassis and the coupling section, between the laser and the bulky vacuum chamber of the MB-LP-TOF machine. An alternative way is to flow dry nitrogen gas through the properly sealed laser path section to reduce the ozone formation. A 10% increase in pulse energy has been observed in our flowing nitrogen setup.

The ArF laser beam coming out of the laser cavity output coupler window has an oblong shape with a dimension of approximately 8mm x 20 mm and a divergence of 2mr x 3mr. A Suprasil planoconvex lens[46] of 1 meter focal length is used to focus the excimer laser beam to a size of 2 mm x 6mm in the scattering zone for the laser photofragmentation experiments. Since the center of the laser beam is aligned to coincide with the molecular beam source rotational axis, it always perpendicularly intersects the molecular beam in the scattering zone. The size of the laser beam in the scattering zone may be changed by using different focusing lenses of the proper focal lengths.

Movable Detection System

In order to meet the criteria described in the previous section, a bakable four-stage differentially pumped detection system has been constructed on a one-dimensional translational rail[47] stand which is securely coupled to the scattering chamber stand. This detection system consists of the ionization chamber and the ion detection chamber. The ionization chamber (LIFTOF-DET-01), fabricated by UHV Inc.,[48] houses the electron bombardment ionizer and the quadrupole mass filter; whereas the ion detection chamber (LIFTOF-DET-16) contains the dumbell ion target and photomultiplier of the Daly ion detection unit.

The detection system is mounted on a thick steel plate which is supported by four 3/4" diameter threaded rods secured on a pillow block.[49] The horizontal position of the detection system can be adjusted by carefully changing the relative position of the four threaded rods. In addition, by slowly turning the nuts on the threaded rods fine vertical height adjustments can be made. Although the alignment of this detection unit with the beam source generation unit is a tedious task, one can use a cathetometer and follow a procedure similar to that described previously to achieve it.

A 1-1/2" stainless steel high vacuum gate valve[50] has been installed in the front port of the detector chamber so that movement of the detector chamber can be done without venting the chamber. At present time, the range of flight path lengths for laser photofragmentation experiments is 48.9 - 97.2 cm, while that for TOF chopper wheel experiments is 33.7 - 82.0 cm. Due to the long flight

path length, only a very small fraction of the fragment molecules produced in the scattering zone reach the ionizer. In the case of laser photofragmentation of a CS_2 beam, it is estimated that the number of CS fragments arrived in the ionization zone is about 2×10^5 molecules for flight path length = 48.9 cm. All instrument parameters and assumptions for this calculation are found in Appendix C.

The ionizer chamber is a tall stainless steel liquid nitrogen cooled shroud whose lower portion is blazed with a OFHC (Oxygen Free High-conductivity Copper) copper block. The large liquid nitrogen cooled surface serves as a cryosorption panel to provide effective punmping for condensable matter (depending on the nature of the gases[51]), whereas the copper block provides a mounting base for the electron bombardment ionizer.

Because of the length of the stainless steel shroud in contact with liquid nitrogen, distinct shrinkage due to thermal contraction[52] is expected. As a consequence, the true position of ionizer changes about 1/8" after filling the liquid nitrogen reservoir. To solve this problem, a 5-1/2" I.D. stainless steel flexible coupling bellows[53] has been installed between the ionizer chamber mount flange and the detector chamber port flange as shown in Figure 2. This flexible coupling bellows provides a means for adjusting the position of the cold ionizer (77 K) in the crucial detection system alignment process.

The ionizer

One of the design goals for the detection system of the MB-LP-TOF machine is to detect all types of neutral fragment molecules. Therefore, an axial type electron bombardment ionizer of high ionization efficiency is used (Extranuclear[54] Model 041-1). All electrical wires in the ultra high vacuum environment are bare and made of 0.050" diameter electronic grade oxygen free solid copper (Copper 101).[55] Power for the ionizer is supplied by an ionizer control through a 10-wire high vacuum instrumentation feedthrough[56] (Extranuclear Model 020-2).

The electron bombardment ionizer is a molecular density detector. The number of ions "N" formed per second in the ionizer is given by[57]

$$N = inlA\sigma(E)$$

where "i" is the electron flux in the ionization region, "n" is the number density of the species being ionized, "l" is length of ionization region, "A" is the cross sectional area of the ionization region that the electron beam sweeps out, and "$\sigma(E)$" is the ionization cross section. One sees that "N" can be increased by increasing the electron flux to the ionization volume. Furthermore, the difference between the the total ion signal observed and the ion signal from the residual gases is due to the ionization of scattered fragment molecules and is the effective ionization signal. Thus, to achieve a better signal to noise condition, one may enlarge the beam entrance aperture in the ionizer. An increased signal to noise ratio is indeed observed when the diameter of ionizer entrance aperture is changed from 1/8" to 1/4".

The mass filter and exit lenses

A Paul type quadrupole mass filter[58-60] has been chosen to serve as a mass filtering unit due to its simplicity in design and construction. In addition, the transmission and resolution of this type of mass filter can be readily adjusted to optimize the two conflicting requirements of high detection sensitivity and resolution.

The quadrupole mass filter is simply a set of four stainless steel rods with proper insulation spacers. The stainless steel rods (LIFTOF-DET-05) are precisely machined and polished with micropolishing powders to a high surface finish.[61] Two insulation spacers (LIFTOF-DET-07) made from MACRO glass ceramic material[62] are used to hold these four stainless steel rods in a nearly perfect position. Since all pieces are precisely machined and the MACRO spacers are fragile, extreme care is required when inserting the whole unit into the Quadrupole Rod Can (LIFTOF-DET-12). The electrical wires in the vacuum chamber are attached by mechanically tightening 0.060" diameter bare wires (copper 101) to a modified two-connector electrical vacuum feedthrough.[63] The power supply for the mass filter is an Extranuclear Model 011-1 with an appropriate High Q Head.

The exit lens set consists of the Entrance Lens (LIFTOF-DET-02), the Middle Lens (LIFTOF-DET-03), and the Exit Lens (LIFTOF-DET-04) and is mounted on the Quadrupole Rod Can Backplate (LIFTOF-DET-14) through the use of 1/8" ceramic rods[64] and 0-80 stainless steel threaded rods.[65] This exit lens set has been constructed to improve the ion collection efficiency in the ion detection unit. All electrical connections inside

the vacuum chamber are accomplished by spot-welding short pieces of 0.020" diameter bare tantalum wires onto the nickel leads of a three-connector instrumentation feedthrough.[66] A EG&G ORTEC[67] Model 459 and a TENNELEC[68] Model TC950 0-5 kV DC power supply units are used for this exit lens set. In normal operation, the applied voltages are -150V, -1 kV, and -1 kV, respectively, for the Entrance Lens, the Middle Lens, and the Exit Lens.

The Daly ion detector and photon counting electronics

Although an electron multiplier may be used as an ion detector, a Daly scintillation type ion detector[69] has been constructed because of its effectiveness in detecting low ion currents. The Daly ion detector is composed of an aluminum coated, dumbbell-shaped stainless steel ion target, a scintillation window and a photomultiplier. In order to reduce the probability of field emission and increase secondary electron yields, all machined stainless steel pieces in this ion detection region are polished to a very high surface finish.

The ions coming out of the exit lens set of the mass filter are accelerated toward the dumbbell high voltage cathode surface, where they generate secondary electrons. Since aluminum has the highest secondary electron yield per bombarding ion among most common metals,[70] a 2500 Å thick layer of aluminum is coated[71] on the ion target surface of the stainless steel dumbbell. The secondary electrons emitted from the aluminum surface strike the scintillation window and generate fluorescence which is detected by a high gain photomultiplier.

The scintillation window is a quartz plate to which is cemented a 2.0 mm thick Pilot B plastic scintillator.[72] The scintillator surface is then coated with aluminum to a thickness of 1600 Å.[73] This thin aluminum layer does not prevent the high energy electrons from reaching the scintillation, but cuts down on the background light (mostly coming from the filaments of the ionizer) that can enter the photomultiplier, keeps the surface of the scintillation window at ground potential, and thus increases the photon detection efficiency from the scintillator.

The optical contact between the uncoated surface of the quartz plate and the surface of the EMI 9924S photomultiplier tube[74] is made by a thin layer of Dow Corning Q2-3067 Optical Couplant[75] in order to lower reflection losses of photons of small incident angle on the surfaces of the scintillator and the photomultiplier. In addition, the photomultiplier is wrapped with a thin sheet of MμShield[76] to reduce the magnetic interference from the nearby instruments and ion pumps.

In normal operation, the voltage applied to the dumbbell ion target is between -18,000 and -25,000 VDC, while that applied to the photomultiplier is between +1,050 and 1,250 VDC.

Owing to the use of the high gain photomultiplier, further signal amplification is not needed. However, the signal pulses from the photomultiplier pass through a EG&G ORTEC Model 436 discriminator, and are counted by a EG&G ORTEC Model 449/2 counter/ratemeter and also parallel counted and stored in the Motorola 6809 microprocessor of the LASER MCS unit. (See Appendix A.)

Data Acquisition and Manipulation

The heart of the data acquisition system of this MB-LP-TOF machine is a multichannel scaler (LASER MCS unit) which contains a Motorola 6809 microprocessor with 1024 memory locations for storing data directly from the photon counting electronics of the detection system. The data acquisition routine is initiated by a modulated pulse from a photodiode (chopper wheel experiment) or by a triggering pulse coming directly from the pulsed excimer laser (laser photofragmentation TOF experiment).

In the TOF chopper wheel experiment, a photon emitter and receiver set is used as the triggering source for the data acquisition task. The photon emitter is a Motorola MFOE106 photodiode which continuously emits infrared photons and the photon receiver is a Motorola MFOD photodiode. The trigger for obtaining the TOF spectrum is obtained by chopping the emitting infrared signal with the slotted chopper wheel which rotates at desired speeds.

The chopper wheel is made of aluminum alloy 2024-T3 (LIFTOF-MCH-18). It is 7.000" in diameter, 0.125" thick in the center portion, and 0.020" thick on the edge of its outer circumference. On opposite sides of the outer circumference of the chopper wheel are precisely machined two identical slots, 0.020" wide x 0.280" long. These two slots are used as a gated passways for molecules to fly through the chopper wheel to the detector system and for photons to trigger the photon receiver to send a pulse to the multichannel scaler for starting the data acquisition task.

The chopper wheel is powered by a TRW type FC hysteresis synchronous motor[77] which can rotate the wheel up to 500 revolutions per second. As the slot in the chopper wheel moves past the detector direction, it allows a segment of molecules to fly toward the detector. At the same time the molecules start to move into the detector a triggering pulse is initiated in the photon receiver which causes the time counter to reset to zero and begin the data acquisition routine. As the molecules travel through the detector they are ionized in the ionizer; the ions are mass-selected by the quadrupole mass filter and then detected by the Daly ion detector. Through the photon counting electronics, a series of fast voltage pulses coming out of the discriminator output terminal is fed into the LASER MCS unit where they are counted and accumulated in the various memory locations according to their time domains.

An oscilloscope is used as the X-Y display to show the present contents of all 1024 memory locations in the microprocessor of the LASER MCS unit. The new contents in the multichannel scaler are accumulated at six second intervals into the memory according to their particular locations in order that the X-Y display might provide a reliable indication of the data acquisition process. Therefore, the TOF spectrum is observed on the oscilloscope screen during the data aquisition period.

In the laser photofragmentation TOF experiment, a trigger pulse comes from the external trigger port of the excimer laser and corresponds to each firing of the laser pulse. The trigger pulse

initiates each data acquisition sweep. The TOF spectrum of the product fragments is shown on the X-Y display in exactly the same manner as that described above for the TOF chopper wheel experiment. The detailed operation of the multichannel scaler for the data acquisition is described in Appendix A.

The manipulation of the data from the MB-LP-TOF machine is accomplished by a Digital LSI-11/23 microcomputer. The computer system includes several auxiliary external hardware components (keyboard/screen terminals, an auto dial modem, a near letter quality matrix printer, and a multipen plotter) and many useful programs (FORTRAN-77, HGRAPH, VTCOM, etc. in the system software library). The LSI-11/23 computer is interfaced to the LASER MCS system through a common RS-232-C communication device.

When a TOF experiment is completed, the data stored in the 6809 microprocessor memory of the LASER MCS unit are transferred to the LSI-11/23 computer by the modem (MOdulator/DEModulator) and the VTCOM communication program. The data transferring rate is internally set in the 6809 microprocessor at 2048 bauds (2048 bits per second, or approximately 200 characters per second). The data transfer procedure is as follows:

1. Press "Ctrl-P" to invoke the VTCOM command mode.
2. Type "OP" and hit Return key to open a file in the LSI-11/23 computer to store the current time of flight data.
3. Type "NNNNNN" and hit the Return key. The file is then named "NNNNNN.LOG".

4. Hit Return key one more time to invoke the main command menu of LASER MCS system.
5. Type "PRIN" and hit Return key to start transferring data from the 6809 microprocessor memory to the LSI-11/23 computer. At this moment, one should see the contents of each memory location scrolling on the terminal screen until the process is complete.
6. Press "Ctrl-P" to invoke the VTCOM command mode again.
7. Type "CLO" and hit Return key to close the NNNNNN.LOG file in the LSI-11/23 computer. The whole data transfer process is then completed.

Once the TOF data are stored in the LSI-11/23 computer, the rest of the data manipulation tasks can be achieved by using various fortran programs. Two of the most useful programs written in FORTRAN-77 language can be found in Appendix F. The data plotting routines are done by including a graph plotting subroutine called HGRAPH in the main fortran program. The HGRAPH subroutine program can do most common data plotting tasks such as automatic scaling, axis labeling, multicurve plotting, legend writing, etc. The results of the data manipulation can be seen on the VISUAL 550 graphic terminal screen and, moreover, their hard copies or plots can be obtained from the Digital LA210 Letterprinter or the Houston DMP-29 multipen digital plotter.

Initial Tests and Operations

Mass spectrum of background gases in detector chamber

In the initial operation of the newly constructed detection system, a mass spectrum has been taken to identify the most abundant background gases in the detector chamber. The mass spectrum is shown in Figure 5. However, the gas component ratio shown in the mass spectrum will change with time due to the substantial pumping in the detector chamber under machine operation conditions. Therefore, another mass spectrum must be taken if one wants to know the partial pressure of a particular background gas inside the detector chamber at the time of the experiment.

Delay time in mass spectrometer

For all TOF measurements in the MB-LP-TOF machine, there is always a delay[78] between the time a neutral molecule reaches the ionizer and the time a pulse is counted by the detector. Most of this delay is caused by the time required for the ion to drift through the mass spectrometer. This ion drift time is approximately proportional to the square root of the ion mass. However, because of the extraction difficulties caused by the negative space charge of the electrons in the ionizer, a "memory effect"[79] is expected. As a result, the true experimentally measured delay times are normally greater by a few microseconds than those predicted theoretically from the corresponding m/e values and the ionizer conditions.[80] Therefore, measurements of the ion drift times are necessary to correct the flight times of the molecules in the TOF experiments.

Figure 5. Mass spectrum of background gases in dector chamber.

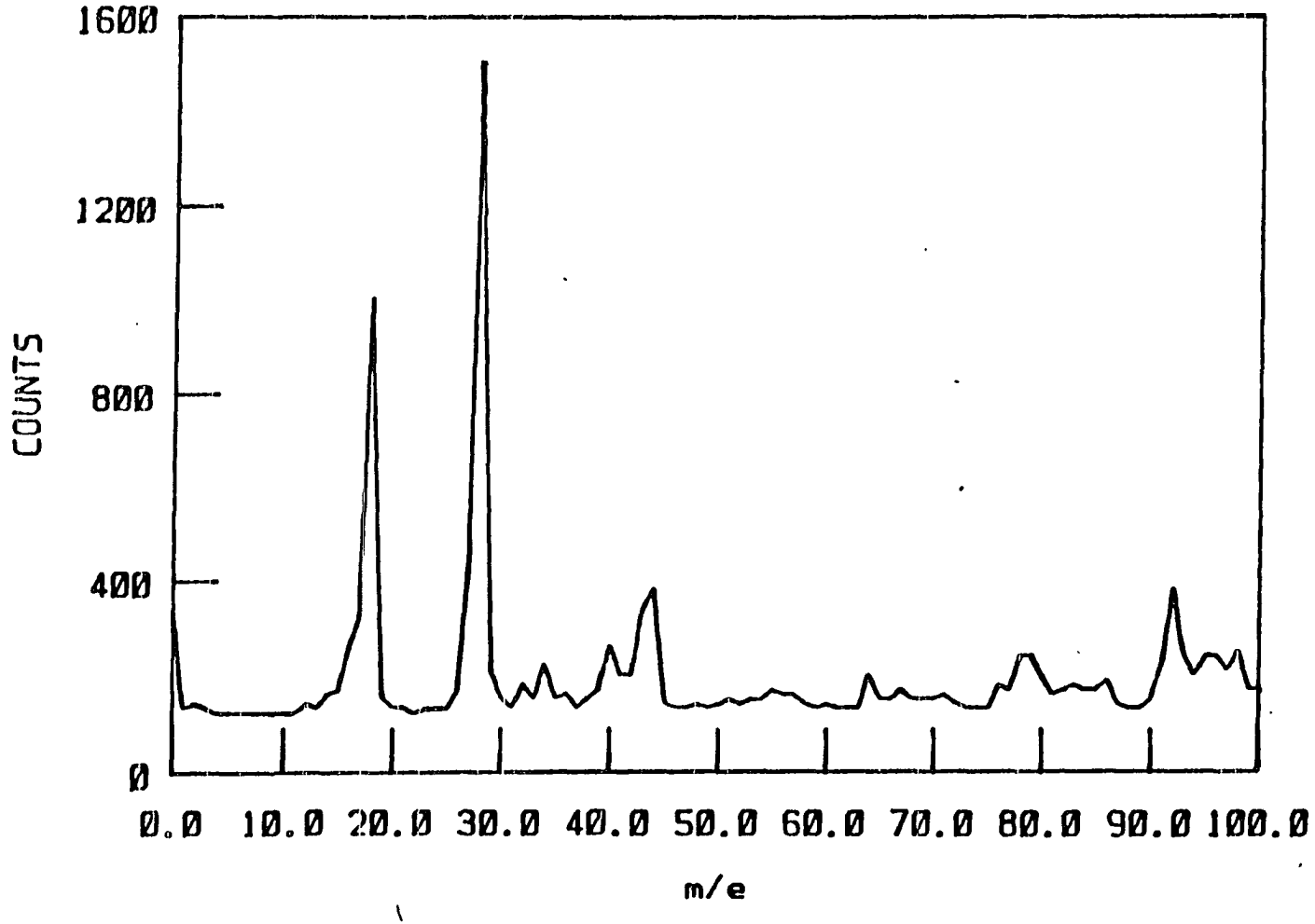
1600
1200
800
400
0
COUNTS
0.0 10.0 20.0 30.0 40.0 50.0 60.0 70.0 80.0 90.0 100.0
m/e

An experiment has been set up to measure the ion drift delay time in the mass spectrometer of the MB-LP-TOF apparatus. By using a function generator which provides ±10V square waves and a 18V battery, one can send a pulse of +18±10V to the extractor of the ionizer and observe the signal coming out of the discriminator and display on the oscilloscope. The ion drift times through the mass spectrometer are determined from the oscilloscope display screen, where the difference between the initial position of the pulses from the function generator (Input Channel A) and the starting position of the signal pulses from discriminator (Input Channel B) is the ion delay time. The results of these delay time measurements are plotted and shown in Figure 6.

TOF chopper wheel experiments

A brief schematic drawing of the time of flight experimental setup is shown in Figure 7. During the TOF chopper wheel experiment the molecular beam is pointing directly at the detector. When the chopper wheel rotates so that a slot on the wheel is in the direction of the detector, a segment of molecules will pass through the slot fly toward the ionizer. Thus, the slot acts like a shutter whose open time period is dependent upon the rotational speed of the chopper wheel. The rotation of the chopper wheel is controlled by the LASER MCS system control unit which sets the initial wheel rotational speed at 40 Hz (revolutions per second) in the counterclockwise direction (or "R" direction in the programmed computer language code). However, the desired wheel rotational direction and speed may be set by entering the

Figure 6. Ion drift time in mass spectrometer.

X — ion energy = 16 V.

□ — ion energy = 18 V.

O — ion energy = 20 V.

Δ — ion energy = 22 V.

⧓ — ion energy = 24 V.

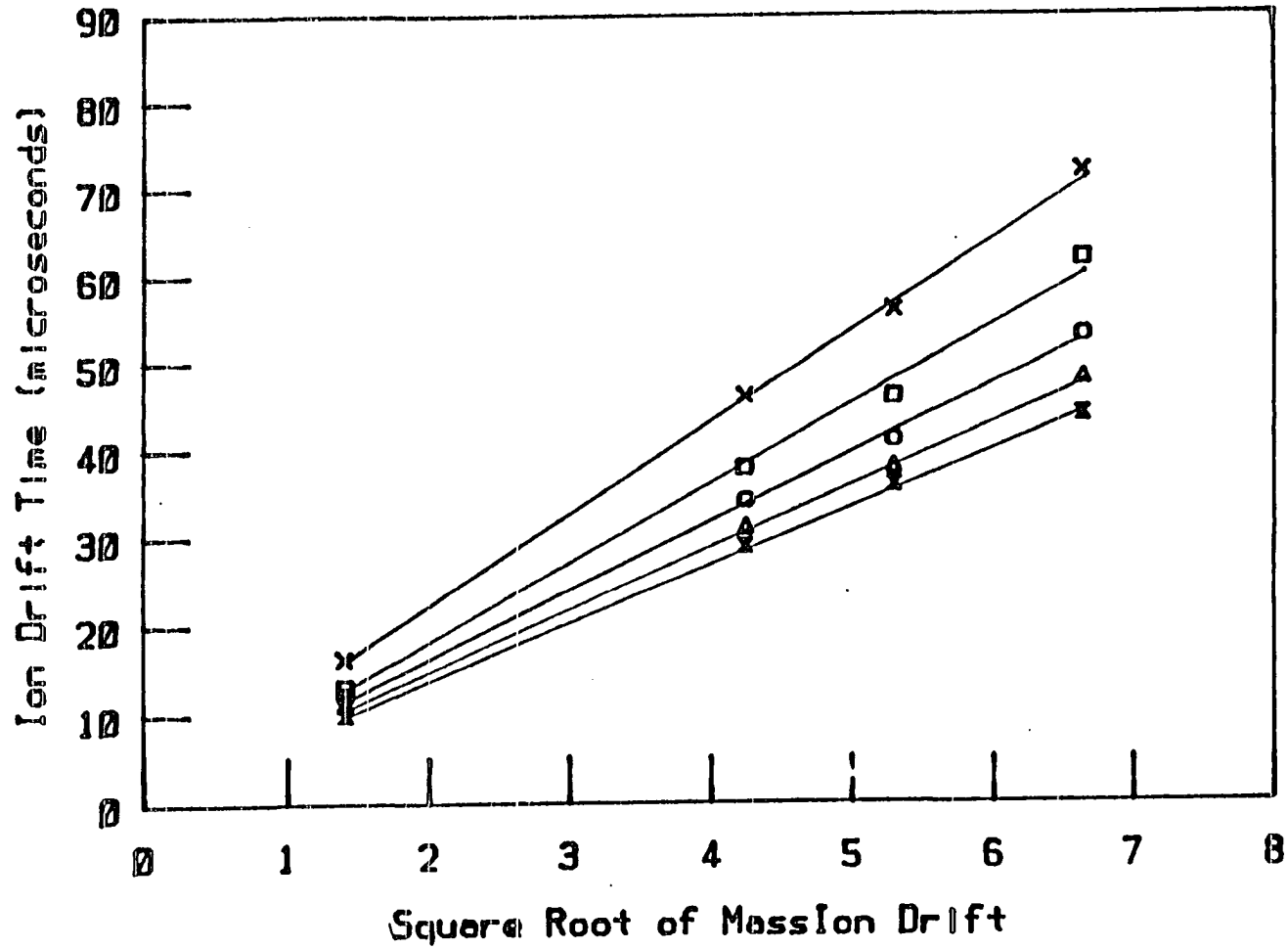
90
80
70
60
50
40
30
20
10
0
Ion Drift Time (microseconds)
0
1
2
3
4
5
6
7
8
Square Root of Mass Ion Drift

Figure 7. Schematic of time of flight experimental setup.

1. supersonic beam nozzle.
2. skimmer.
3. collimator.
4. scattering center.
5. time of flight chopper wheel.
6. photon emitter and receiver.
7. ionizer.
8. chopper wheel rotational center.
9. beam defining aperture.

X_{ns} -- nozzle / skimmer distance.
X_{nc} -- nozzle / collimator distance.
X_{nt} -- nozzle / scattering center distance.
X_{nw} -- nozzle / chopper wheel distance.
X_{ni} -- nozzle / ionizer distance.

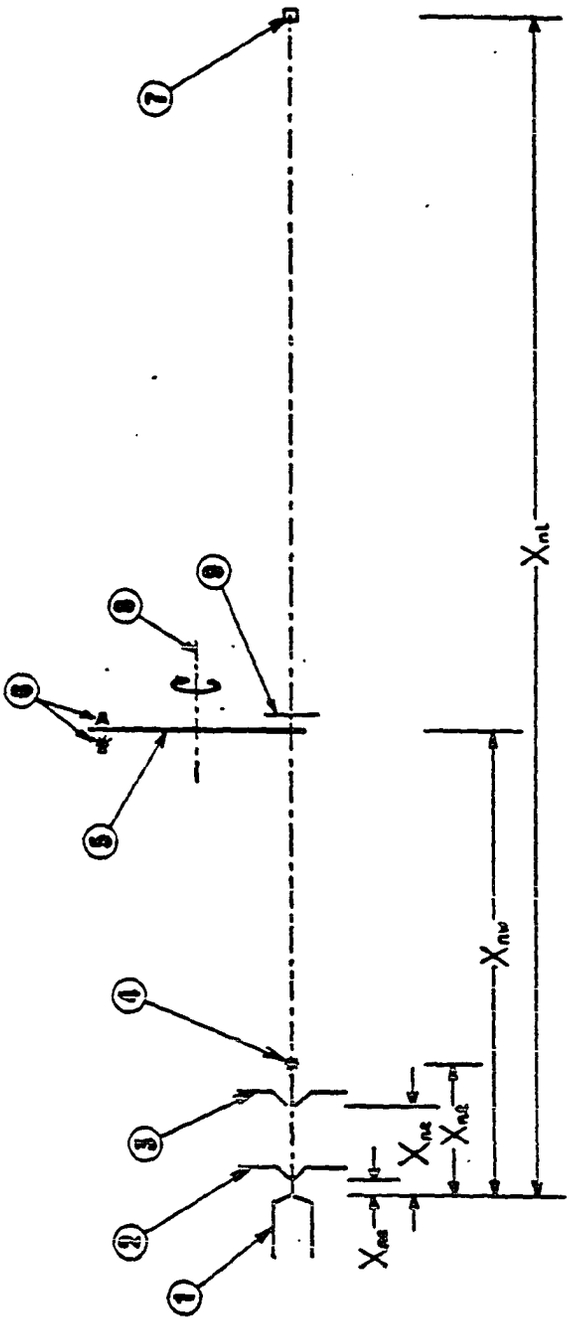
7
6
8
5
4
3
2
1
X_{n1}
X_{n3}
X_{n2}
X_{n2}
X_{n3}

appropriate input information in response to the chopper wheel direction and speed query modes during the operation of the LASER MCS system. (See Appendix A for detailed operational description.) The chopper wheel rotational speed is then related to the channel dwell time in the multichannel scaler for the TOF chopper wheel experiments.

In order that the data acquisition routines can be meaningful, the sweep time (the channel dwell time times the number of channels) in the multichannel scaler must be less than the time between pulses received from the triggering device. The multichannel scaler is designed so that its channel dwell time can be changed by setting an external thumbwheel dialing device. Since a 50 M Hz crystal oscillator is used as the time base, the channel dwell time = 20 nanoseconds x (thumbwheel number + 1). The number of channels in the multichannel scaler has been set to 1024 internally, therefore a "99" on the thumbwheel dialing device gives a sweep time of 2.048 milliseconds. For a 2-slot chopper wheel rotating at 100 Hz, the pulse interval is 5 milliseconds. Therefore, the upper limit for an allowable number on the thumbwheel dialing device is 243 (4.88 microseconds/channel).

Different wheel rotational directions in the chopper wheel experiments may yield different results for the TOF time measurements. This inevitable problem arises from: (1) uncertainty in the true location of the two machined slots on the chopper wheel, and (2) inaccuracy in mounting the tiny photon emitter and receiver set which triggers the timing circuitry in the data acquisition routine task of the LASER MCS system. To get around this problem, the measured time of

flight data has been calibrated by running the chopper wheel in opposite directions at the same rotational speeds. The result is shown in Figure 8. Thus, the true time of flight data set is taken to be the average values of the two data sets for "F" and "R" directions.

This has been achieved by placing a 0.005" diameter aperture behind the chopper wheel. The aperture provides better differential pumping in the detector chamber because it prevents many molecules passing through the chopper slot from entering the detector. It is important that the pressure in all three regions of the detector chamber be low in order that a good signal to noise ratio is observed for the time of flight chopper wheel experiments.

The velocity distribution of a molecular beam under particular operational condition can be determined by TOF chopper wheel experiments.[81-84] The velocity distribution function f(v) is defined by

$$dI = I_0 f(v)\, dv \qquad (1)$$

where I_0 is the beam intensity without interruption by the chopper wheel and V is the velocity of the molecules. The total number of molecules per unit area entering the ionizer is $N_0 = I_0 t_0$ for the shutter open time interval of t_0. (At the moment the center of the slot on the chopper wheel is in the direction of the detector.) The distribution of these molecules is then expressed as

$$dN = N_0 f(v)\, dv. \qquad (2)$$

In the ideal conditions where (1) the shutter open time interval is negligible in comparison with the flight time of molecules and (2) the ionization length of the detector is negligible in comparison with the

Figure 8. Time of flight spectrum of CS_2 for chopper wheel running in two opposite directions.

experimental conditions:

room temperature nozzle;
stagnation pressure = 150 Torr;
nozzle diameter = 0.005";
nozzle/skimmer distance = 0.300";
flight path length = 33.7 cm;
dwell time = 2 microseconds per channel.

1. "F" direction, peak at channel 390.
2. "R" direction, peak at channel 417.

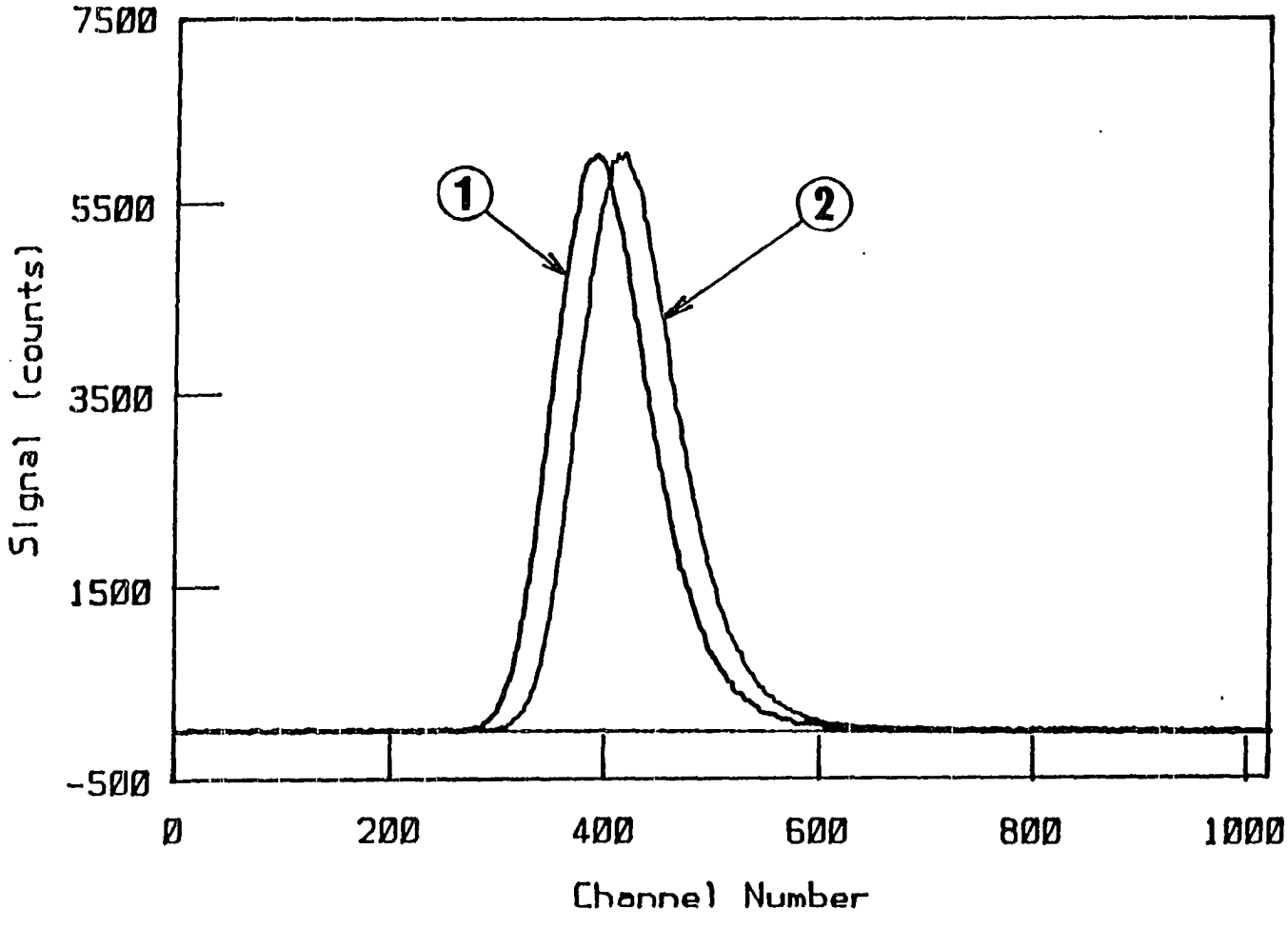
7500
5500
3500
1500
-500
Signal (counts)
1
2
0
200
400
600
800
1000
Channel Number

flight path length l, the flight time of molecules is given by

$$t = l / v. \tag{3}$$

From equations (2) and (3) one obtains

$$I = dN / dt = N_0 f(v) v^2 / l. \tag{4}$$

Since the electron bombardment ionizer is a molecular density detector, the detected signal S is proportional to the number density of the molecules in the ionizer. Therefore,

$$S \sim n = I/v = N_0 f(v) v / l \tag{5}$$

or, $$S \sim n = I/v = N_0 f(v) / t. \tag{6}$$

The theoretical velocity distribution of beam molecules on the axis is given by[82]

$$f(v) = c\left(\frac{v}{v_s}\right)\exp\left[-\frac{1}{2}\gamma M_s^2\left(\frac{v}{v_s} - 1\right)^2\right], \tag{7}$$

where c is a constant; v_s is the stream flow velocity at the skimmer entrance; γ is the specific heat ratio of the beam gas; M_s is the Mach number for the gas stream at the skimmer entrance. For a continuum isentropic flow from the nozzle to the skimmer entrance, and with no interference of the stream entering the skimmer,

$$v_s^2 = \frac{2kT_s}{m}\,\frac{\gamma M_s^2}{2}$$

$$= \frac{2kT_0}{m}\left(1 + \frac{\gamma-1}{2}M_s^2\right)^{-1}\frac{\gamma M_s^2}{2}, \tag{8}$$

where k is the Boltzmann gas constant; T_s is the gas stream temperature at the skimmer entrance; m is the mass of the gas molecules and T_0 is the nozzle stagnation pressure. From equations (6) and (7), one can derive

$$S \sim \frac{1}{t^4} \exp[-\frac{1}{2}\gamma M_s^2(\frac{1}{tv_s} - 1)^2]. \qquad (9)$$

Then, the normalizied expression of equation (9) is

$$\frac{S}{S_{max}} = \frac{1}{\tau^4} \exp\{-\frac{1}{2}\gamma M_s^2[(\frac{b}{\tau} - 1)^2 - (b - 1)^2]\}, \qquad (10)$$

where $$b = \frac{1}{2}[1 + (1 + \frac{16}{\gamma M_s^2})^{1/2}]$$

and τ is the ratio of flight time t to the flight time for which S is a maximum.

Using equation (10) one may plot out the calculated TOF data as shown in Figure 9. These calculated results are then used to fit the experimental data to obtain the corresponding beam gas speed ratio (Mach number), from which the velocity distribution of the beam molecules may be obtained by the use of equation (7). Figure 10 shows the TOF spectrum of CS_2 obtained with a nozzle stagnation pressure of 150 Torr. The observed velocity distribution of the beam molecules corresponds to a Mach number of 7.

In the photofragmentation experiment, the measured TOF distribution in the laboratory frame must be converted to energy distribution in the center of mass frame so that the data can be meaningful for the molecular photofragmentation dynamics studies.[85-87] The transformation procedure is discussed in Appendix D and a Fortran program for this routine task is included in Appendix F. However, in such a transformation one needs to consider the so-called Newton diagram (velocity vector representation) which requires information on the initial velocity of the parent molecules.

Figure 9. Calculated time of flight signal for a molecular beam at various speed ratios.

1. Mach number = 0 (effusive oven beam).
2. Mach number = 1.
3. Mach number = 5.
4. Mach number = 10.
5. Mach number = 20.
6. Mach number = 50.

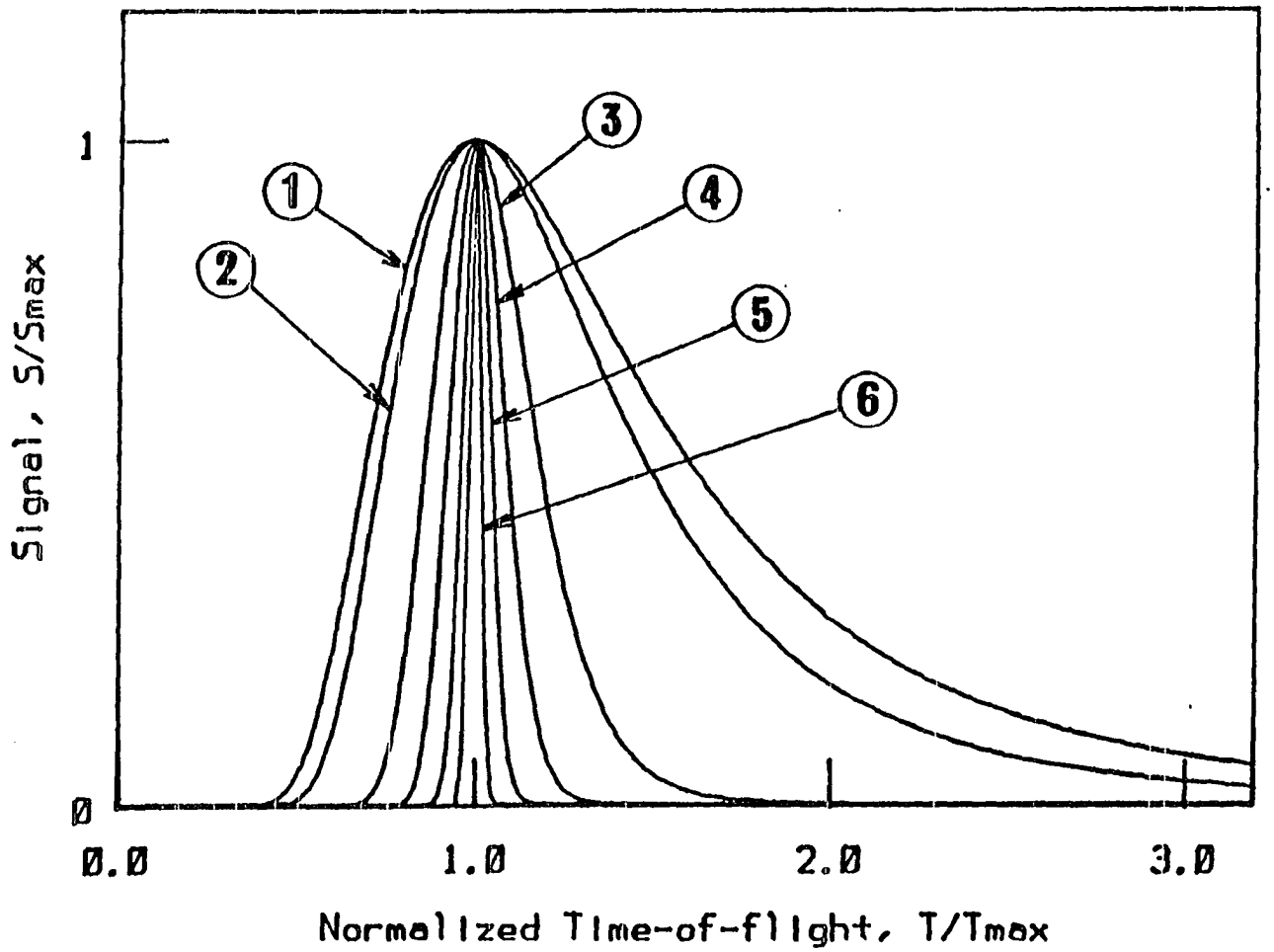
1
Ø
Signal, S/Smax
1
2
3
4
5
6
Ø.Ø
1.Ø
2.Ø
3.Ø
Normalized Time-of-flight, T/Tmax

Figure 10. Time of flight spectrum of CS_2 beam.
experimental conditions:
room temperature nozzle;
stagnation pressure = 150 Torr;
nozzle diameter = 0.005";
nozzle/skimmer distance = 0.300";
flight path length = 33.7 cm;
dwell time = 2 microseconds per channel.

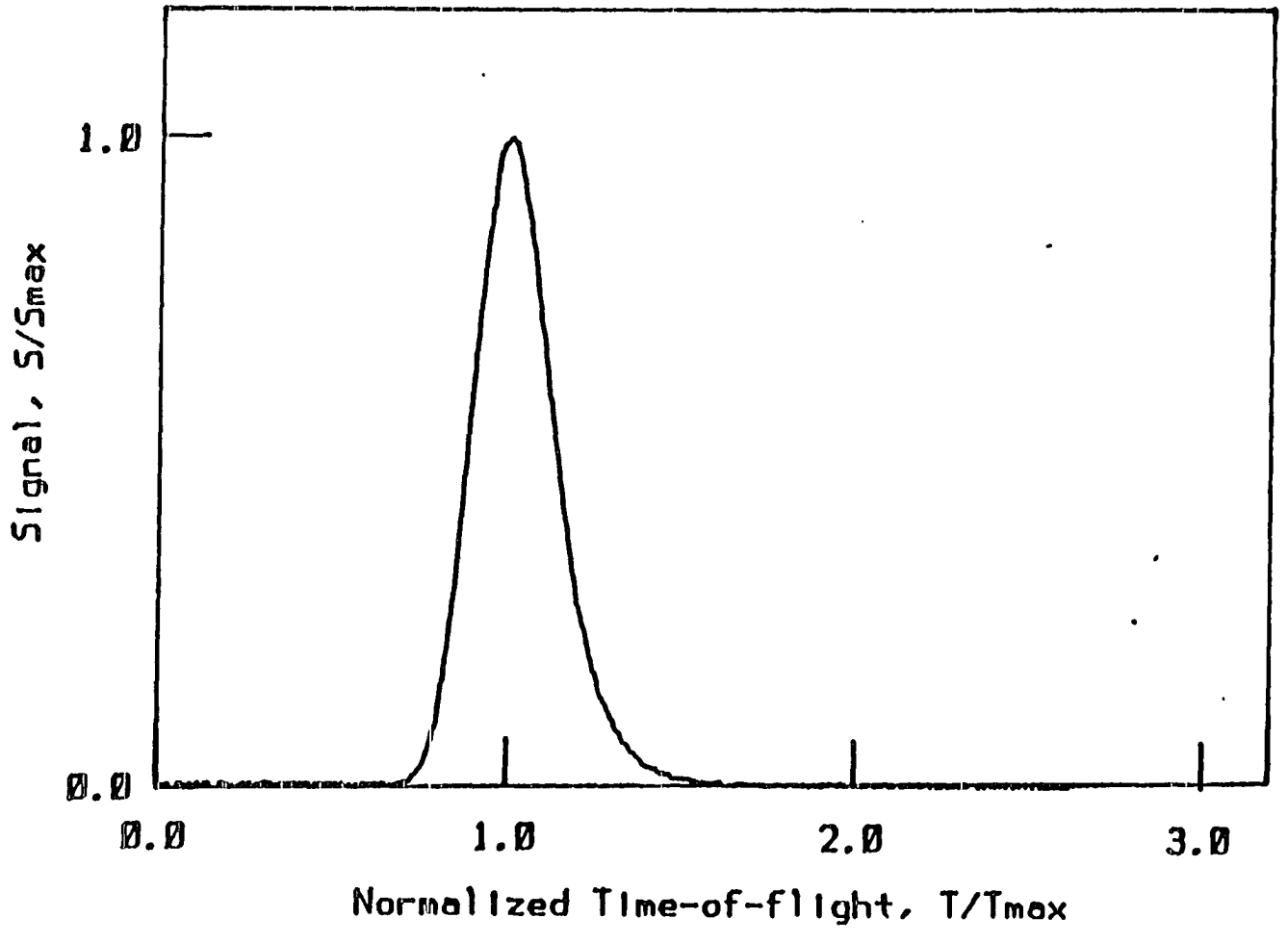
1.0
0.0
Signal, S/Smax
0.0
1.0
2.0
3.0
Normalized Time-of-flight, T/Tmax

Figure 11. Time of flight spectrum of CS_2 beam.
experimental conditions:
room temperature nozzle;
stagnation pressure = 150 Torr;
nozzle diameter = 0.005";
nozzle/skimmer distance = 0.300";
flight path length = 33.7 cm;
dwell time = 2 microseconds per channel.

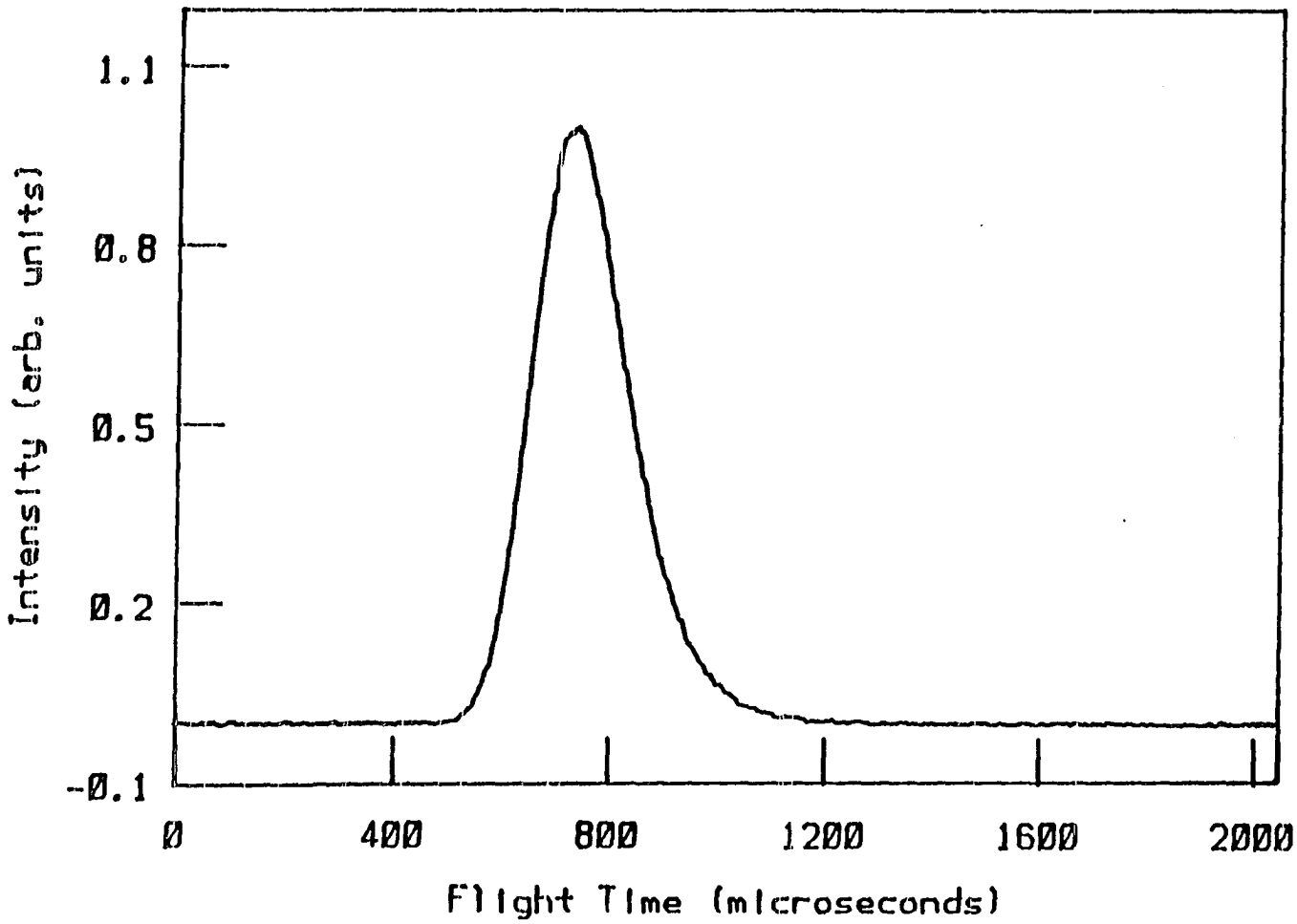
1.1
0.8
0.5
0.2
-0.1
Intensity (arb. units)
0
400
800
1200
1600
2000
Flight Time (microseconds)

In the CS_2 photofragmentation experiment, the initial velocity of the CS_2 molecules has been measured by the TOF chopper wheel experiment. Figure 11 shows the TOF spectrum of CS_2 molecules, in which the spectrum has been calibrated for the direction of the chopper wheel rotation and the delay time in the detection system as previously discussed. The most probable velocity observed for those experimental conditions is about 4.6×10^4 cm/sec.

The initial tests and experiments described above have verified the proper performance of the MB-LP-TOF machine.

References

1. E. H. Taylor and D. S. Datz, J. Chem. Phys. 23, 1711 (1955).
2. H. U. Hostettler and R. B. Bernstein, Phys. Rev. Lett. 5, 318 (1960).
3. F. A. Morse, Ph.D. Dissertation, University of Michigan, Ann Arbor, MI, 1962.
4. D. R. HerschBach, G. H. Kwei and J. A. Norris, J. Chem. Phys. 34, 1842 (1961).
5. K. R. Wilson, UCRL Rep. 11645, Lawrence Radiation Laboratory, Berkeley, CA 1964.
6. S. J. Riley, Ph.D. Dissertation, Harvard University, Cambridge, MA, 1970.
7. Y. T. Lee, J. D. McDonald, P. R. LeBreton and D. R. Herschbach, Rev. Sci. Instrum. 40, 1402 (1969).
8. R. W. Bickes, Jr. and R. B. Bernstein, Rev. Sci. Instrum. 41, 759 (1970).
9. D. L. McCullough, Jr., F. Kalos and J. Ross, J. Chem. Phys. 59, 121 (1973).
10. J. B. Anderson, R. P. Andres and J. B. Fenn in Advances in Chemical Physics, edited by J. Ross (John Wiley & Sons, New York, 1966), Vol. 10, p.308.

11. H. F. Prest, Ph.D. Dissertation, Iowa State University, Ames, IA, 1984.

12. Drawings are available through: Professor C. Y. Ng, 103 Wilhelm Hall, Ames Laboratory, Iowa State University, Ames, IA 50011.

13. 20" Halo baffle for Varian model HS-20 diffusion pump (Order No. 0322-K1855-320), Varian Associates, Vacuum Division, 708 Landwehr Rd., Northbrook, IL 60062.

14. Stokes Vacuum Products, 5500 Tabor Road, Philadelphia, PA 19120.

15. Leybold-Heraeus Vac. Prod. Inc., 1210 S. Garfield, Lombard, IL 60148.

16. This Varian model 330 low-profile water cooled baffle for VHS-10 diffusion pump (Order No. 0330-F8600-310) can be used with mechanical refrigeration to reduce equilibrium vapor pressure of re-evaporating pump fluid and thereby attain a partial trapping effect.

17. Balzers Corp., 8 Sagamore Park Road, Hudson NH, 03051.

18. Varian Cat. No. 951-5219, Varian Associates, Vacuum Division, 708 Landwehr Road, Northbrook, IL 60062.

19. Kaydon model no. KC160XPO, Keene Corp., Kaydon Bearing Division, Muskegon, WI 49443.

20. Tubular Case 60 Shaft, Class L, 2" O.D. x 1-1/4" I.D., Thomson Industries, Inc., Shore Road, Port Washington, NY 11050.

21. Parker No. A2-385, Parker Hannifin Corporation, O-Ring Division, 2360 Palumbo Drive, Lexington, KY 40509.

22. Boston Gear No. G1055, 12 D.P. Worm Gear Set, Boston Gear Division, 14 Hayward Street, Quincy, MA 02171.

23. Drum Dial Stock No. A1-4, Winfred M. Berg Inc., 509 Ocean Ave., E. Rockway, Long Island, NY 11518.

24. Superior Model M112-FD06 SLO-SYN Synchronous/Stepping Motor, Superior Electric Co., 799 Roosevelt road, Glen Ellyn, IL 60137.

25. Wallace & Tiernan Model 62A-4A-0150 Differential Pressure Gauge, Pennwalt Corporation, Wallace & Tiernan Division, 25 Main Street, Belleville, NJ 07109.

26. For example, VICTOR rare gas regulator with CGA-580 adapter for 0-100 psig positive pressure coarse control and Matheson Model 3491

for 0-760 mm Hg fine pressure regulation.

27. Matheson Model 6184-P4FF Replaceable Element Filter, Matheson Gas Products, P. O. Box 96, Joliet, IL 60434.

28. O. F. Hagena and H. S. Morton Jr., "Analysis of Intensity and Speed Distribution of a Molecular Beam from a Nozzle Source", Rarefied Gas Dynamics, Vol. 2 (Academic Press, New York, 1967), p. 1369.

29. K. Bier and O. F. Hagena "Optimum Condition for Generating Supersonic Molecular Beams", Rarefied Gas Dynamics, Vol. 2 (Academic Press, New York, 1966), p. 260.

30. J. E. Scott, Jr. and J. E. Drewry, "Characteristics of Aerodynamic Molecular Beams", Rarefied Gas Dynamics, Vol. 1 (Academic Press, New York, 1963), p. 516.

31. Ernest F. Fullam, Inc., P. O. Box 444, Schenectady, NY 12301.

32. R. N. Zapata, Ph.D. Dissertation, University of Virginia, Charlottesville, VA, 1960.

33. R. Behrens Jr., Ph.D. Dissertation, University of California, Berkeley, CA, 1975.

34. S. K. Searles and G. A. Hart, Appl. Phys. Lett. 27, 243 (1975).

35. C. A. Brau and J. J. Ewing, Appl. Phys. Lett. 27, 435 (1975).

36. E. R. Ault, R. S. Bradford, Jr. and M. L. Bhaumik, Appl. Phys. Lett. 27, 413 (1975).

37. J. J. Ewing and C. A. Brau, Appl. Phys. Lett. 27, 350 (1975).

38. J. A. Mangano and J. H. Jacob, Appl. Phys. Lett. 27, 495 (1975).

39. G. C. Tisone, A. K. Hays and J. M. Hoffman, Opt. Commun. 15, 188 (1975).

40. Questek Inc., 44 Manning Road, Billerica, MA 01821.

41. "Excimer Lasers", ed. by Ch. K. Rhodes (Springer-Verlag, New York, 1984).

42. The high purity gases are purchased from Spectra Gases, 320 Mt. Pleasant Ave., Newark, NJ 07104 or MG Industries, 175 Meister Ave., P. O. Box 5328, North Branch, NJ 08876.

43. Millipore Cat. No. WGFG 06W B1 Wafergard F In-line Filter, Millipore Corporation, Ashby Road, Bedford, MA 01730.

44. Suprasil is a trade mark of Amersil Inc.

45. Corning Glass Works, Advanced Products Department, Corning, NY 14831.

46. Acton Part No. 1.5D-.5MX, Acton Research Corporation, P. O. Box 215, 525 Main Street, Action, MA 10720.

47. Thomson Cat. No. SR-10 shaft support and 5/8" nominal diameter 60 case, class L solid shaft, Thomson Industries, Inc., Shore Road, Port Washington, NY 11050.

48. Ultra High Vacuum Instruments, Inc., 901 Fuhrmann Blvd., Buffalo, NY 14203.

49. Thomson Cat. No. SPB-10-OPN open type pillow block ball bushing, Thomson Industries, Inc., Shore Road, Port Washington, NY 11050.

50. MDC Model GVA-1500-V, MDC Vacuum Products Corporation, 23842 Cabot Blvd., Haywood, CA 94545.

51. S. A. Stern, R. A. Hemstreet and D. M. Ruttenbur, J. Vac. Sci. Technol. 3, 99 (1965).

52. Y. T. Lee, J. D. McDonald, P. R. LeBreton and D. R. Herschbach, Rev. Sci. Inst. 40, 1402 (1969).

53. Huntington Cat. No. VF605, Huntington Laboratories, 1040 L'Avenida, Mountain View, CA 94043.

54. Extranuclear Laboratories Inc., Box 11512, Pittsburgh, PA 15238.

55. Utility Brass & Copper Corp., 5 Caesar Place, Moonachie, NJ 07074.

56. Varian Model No. 954-5165, Varian Associates, Vacuum Division, 708 Landwehr Road, Northbrook, IL 60062.

57. R. Weiss, Rev. Sci. Instrum. 32, 397 (1961).

58. W. Paul and H. Streinwedel, Z. Naturforsch. 8a, 448 (1953).

59. W. Paul and M. Raether, Z. Physik 140, 262 (1955).

60. W. Paul, H. P. Reinhard and U. von Zahn, Z. Physik 152, 143 (1958).

61. Such as Linde A, a micropolish aluminum oxide powder of particle size of 0.3 micron. They are available from LECO Corporation, 300 Lakeview Ave., St. Joseph, WI 49085.

62. MACRO is a Corning machinable glass ceramic; it may be purchased from Wesley Tool & Die Corp., Technical Products Division, 5030

North 124th St., Milwaukee, WI 53225.

63. MDC Model Model MC-152, MDC Vacuum Products Corporation, 23842 Cabot Blvd., Haywood, CA 94545.

64. The high precision ceramic rods are available from Kimball Physics, Inc., Wilton, NH 03086.

65. J. I. Morris Co., 394 Elm Street, Southbridge, MA 01550.

66. MDC Model MHV-275-3, MDC Vacuum Products Corporation, 23842 Cabot Blvd., Haywood, CA 94545.

67. EG&G ORTEC Inc., 100 Midland Road, Oak Ridge, TN 37830.

68. TENNELEC Inc. P. O. Box D, Oak Ridge, TN 37830.

69. N. R. Daly, Rev. Sci. Instrum. 31, 264 (1960).

70. H. C. Bourne Jr., R. W. Cloud and J. G. Trump, J. Appl. Phys. 26, 596 (1955).

71. Acton Research Corporation, P. O. Box 215, 525 Main Street, Action, MA 10720.

72. The mixing ratio of optical cement NE-581 is resin: hardener = 4 : 1. Both cement and Pilot B scintillator are available from Nuclear Enterprises, Inc., 931 Terminal Way, San Carlos, CA 94063.

73. J. L. Young, J. Appl. Phys. 27, 1 (1956).

74. THRON EMI Inc., 80 Express Street, Plainview, NY 11803.

75. The Dow Corning Q2-3067 Optical Couplant is grease-like compound with good low temperature adhesion, high clarity, good resolution properties and excellent mechanical shear stability. Its refractive index is close to that of quartz glass and many plastics. The Optical Couplant is available from Dow Corning Corporation, Midland, MI 48640.

76. MμShield Company, Division of Bomco, Inc., 121 Madison Street, Malden, MA 02148.

77. TRW Globe Part Number 75A1003-2 type FC Single Phase A.C. Hysteresis Synchronous Motor, it is available from Arrow Electronics, 375 Collins Road, N.E., Cedar Rapids, IA 52402.

78. J. H. Ling and K. R. Wilson, J. Chem. Phys. 63, 101 (1975).

79. H. C. H. Beijerinck, R. G. J. M. Moore and N. F. Vester, J. Phys. E. 7, 31 (1974).

80. H. Shinohara and N. Nishi, J. Chem. Phys. 77, 234 (1982).

81. O. F. Hagena and W. Henkes, Z. Naturforsch. 15a, 851 (1960).

82. J. B. Anderson and J. B. Fenn, Phys. Fluids, 8, 780 (1965).

83. O. F. Hagena and A. K. Varma, Rev. Sci. Instrum. 39, 47 (1968).

84. H. Haberland, U. Buck and M. Tolle, Rev. Sci. Instrum. 56, 1712 (1985).

85. G. E. Busch and K. R. Wilson, J. Chem. Phys. 56, 3626 (1972).

86. G. E. Busch and K. R. Wilson, J. Chem. Phys. 56, 3638 (1972).

87. R. K. Sparks, Ph.D. Dissertation, University of California, Berkeley, CA, 1979.

SECTION III A LASER PHOTOFRAGMENTATION STUDY OF CARBON DISULFIDE AT 193 NM

Introduction

Studies of kinetic and dynamic mechanisms of photodissociation processes in the VUV region lead to a better understanding of plasms physics, free radical chemistry, laser-assisted chemistry, and atmospheric chemistry.[1] These studies have been greatly improved due to the rapid development in the techniques of molecular and cluster beams and pulsed VUV lasers.[2]

It is well known that supersonic nozzle sources can produce high intensity, cooled molecules in a collisionless condition.[3-8] Busch et al.[9] first adopted this technique and developed a time-of-flight (TOF) technique by crossing a molecular beam with a laser beam and measuring the flight times and angular distributions of the product fragments with a mass spectrometer. This TOF technique has been used successfully for studying molecular photodissociation dynamics such as lifetimes and symmetry properties of dissociative excited states,[10] and energy partitioning[11] and vibrational distributions of fragments.[12]

Photochemistry of carbon disulfide (CS_2) has been studied by flash photolysis,[13-16] resonance fluorescence,[17-18] direct UV absorption,[19] electron impact excitation,[20] KrF laser two photon dissociation,[21] and ArF laser photolysis.[22-25]

The ground state electronic configuration of the linear CS_2 can be written as $....(3\sigma_g)^2(1\pi_u)^4(4\sigma_g)^2(2\pi_g)^4$, $^1\Sigma_g^+$ state. Upon absorption of

a photon in the wavelength range of 185–230 nm, the ground state CS_2 molecule is excited to a bent predissociative state with the electronic configuration of $....(3\sigma_g)^2(1\pi_u)^4(4\sigma_g)^2(2\pi_g)^3(3\pi_u^*)^1$, $^1B_2(^1\Sigma_u^+)$ state, following a mixed intravalency/Rydberg transition. By analyzing a partial rotational spectrum, Douglas and Zanon[26] has shown that upon this photoexcitation, the C-S bonds lengthen from 1.55 to 1.66 Å and S-C-S angle decreases from 180 to 153 degrees.

The energetics of CS_2 photodissociation at 193 nm are as follows:

$$CS_2 + h\nu \longrightarrow CS(X\ ^1\Sigma) + S(^3P) \quad \Delta H = 45.0 \text{ Kcal/mol} \qquad (1)$$

$$CS_2 + h\nu \longrightarrow CS(X\ ^1\Sigma) + S(^1D) \quad \Delta H = 18.6 \text{ Kcal/mol} \qquad (2)$$

In the past few years, controversy has been arisen in determining the branching ratio of these two photodissociation channels. McCrary et al.[24] have pointed out the experimental problems encountered and have performed a coaxial TOF accompanied with a laser induced fluorescence experiment. They have determined that $S(^3P)/S(^1D) = 0.5$. However, in another publication,[2] Jackson reported that the branching ration $S(^3P)/S(^1D) = 2$. It is felt that reinvestigation of this photodissciation system is needed.

We have carried out a study of the photodissociation dynamics of CS_2 at 193 nm using a new high resolution molecular beam laser photofragment TOF mass spectrometer with rotatable beam source and movable detector.

Experimental

The experimental apparatus used in this study consists of the following major parts: (1) a rotatable nozzle beam generation system, (2) an excimer laser, and (3) a movable detection system. The detailed design considerations and constructions are described in the previous section.

A continuous supersonic molecular beam is produced by applying CS_2 at a pressure of 150 torr through a 0.127 mm diameter stainless steel nozzle. The nozzle discharge chamber is pumped by a 20" oil diffusion pump (Varian Model HS-20) and maintains at a pressure of $< 1 \times 10^{-4}$ Torr during normal operation. The collimation chamber, which has a reasonably large flow conductance and a pressure about an order of magnitude lower than that of nozzle discharge chamber, is pumped by a liquid nitrogen trapped 6" oil diffusion pump (Varian Model VHS-6). The scattering chamber, where the molecular beam is perpendicularly crossed with the laser beam and where the photofragmentation reaction takes place, is pumped by a 10" oil diffusion pump. A pressure of 10^{-8} Torr is maintained in this chamber during the photofragmentation experiment. The angle of the rotatable molecular beam source ranges from -90 to +90 degrees with respect to the detector axis and is set by a computer controlled stepping moter.

A multigas excimer laser (Questek Model 2260) is used as the photofragmentation light source. The ArF laser beam is coincident with the rotational axis of the molecular beam source system, therefore it always perpendicularly intersects the molecular beam in the scattering

zone. A Suprasil planoconvex lens of 1 meter focal length is used to focus the laser beam to a size of 2 mm x 6 mm in the scattering zone for the laser photofragmentation experiments. In a typical experiment, the ArF laser is operated at a repetition rate of 100 Hz with pulse energy of 40 - 60 mJ/pulse.

The fragment detection system is a bakable differentially pumped ultrahigh vacuum chamber mounted on a one-dimensional translational rail stand. The translational motion of the detection system is achieved by simply moving the chamber on the rail. This allows one to change the flight path length between 48.9 and 97.2 cm. The first differentially pumped section in the detection system is pumped by a turbomolecular pump (Balzers TPU 330) with a pumping speed of 330 l/s. The base pressure in this region is normally maintained at 10^{-8} Torr. The second region, housing a quadrupole mass filter and a Daly ion detector, is pumped by a Cryo-Boostivac D-I combination pump (Ultek Model 224-0620) with a pumping speed of 150 l/s and a turbomolecular pump (Balzers Model TPU 050) with a pumping speed of 50 l/s. The pressure in this section is maintained at 10^{-9} Torr during normal operation. The innermost region of the detector chamber houses an electron bombardment ionizer (Extranuclear 041-1) and is pumped by a Veeco 100 l/s noble gas ion pump (Veeco Model PN-201). The base pressure in this innermost region is maintained at $\leq 1 \times 10^{-10}$ Torr during normal operation.

The data acquisition routine is initiated by a modulated pulse from a photodiode (TOF chopper wheel experiment) or by a triggering pulse coming directly from the pulsed excimer laser (laser photofragmentation

TOF experiment). In the laser photofragmentation experiment only a very small fraction of the fragment molecules produced in the scattering zone can reach the ionizer. The ions formed in the ionizer are then selected by the mass filter and detected by the ion detector. The signal pulses from the photomultiplier are displayed by a ratemeter (EG&G ORTEC 449/2) and also parallel counted and stored in a 1024-channel multichannel scaler (MCS) which contains a Motorola 6809 microprocessor with 1024 memory locations. When a TOF experiment is completed the data stored in the MCS are then transferred to a Digital LSI-11/23 computer for manipulations. The data manipulation tasks are achieved by using various Fortran programs including a HGRAPH subroutine for data plotting.

For all TOF measurements there is always a delay between the time a neutral molecule reaches the ionizer and the time a pulse is counted by the detector.[27] The delay is caused mostly by the time required for the ion to drift through the mass spectrometer. This ion drift time is approximately proportional to the square root of the ion mass. However, because of the extraction difficulties caused by the negative space charge of the electrons in the ionizer, a "memory effect" is expected.[28] As a result, the true experimentally measured delay times are normally greater by a few microseconds than those predicted theoretically from the corresponding m/e values and the ionizer conditions.[29] Therefore, measurements of the ion drift times are necessary to correct the flight times of the molecules in the TOF experiments. A measurement of the ion drift delay time in the mass spectrometer has been done by pulsing the

extractor of the ionizer and observing the display on the oscilloscope of the signal coming from the discriminator.

In order that the interpretation of experimental data is meaningful, the laboratory TOF distribution must be converted into the c.m. translational energy distribution. The transformation involves considering a Newton diagram (velocity vector representation) which requires information on the initial velocity of the parent molecules. Assume that the detector axis is the x axis, then for each TOF datum point,

$$v_{LAB} = l / t$$

$$v_y = v_{LAB} \cdot \text{Sin}\ (\Theta_{LAB})$$

$$v_x = v_{LAB} \cdot \text{Cos}\ (\Theta_{LAB}) - u_{LAB}$$

$$v = (v_x^2 + v_y^2)^{1/2}$$

where, v_{LAB} is the fragment laboratory velocity; l is the length of the flight path; t is the fragment flight time; Θ_{LAB} is the laboratory angle; v_x is the x component of the fragment c.m. velocity; v_y is the y component of the fragment c.m. velocity; and u_{LAB} is the initial velocity of the parent molecules; and v is the fragment c.m. velocity.

The c.m. translational energy distribution of the fragments, $P(E_t)$, can be expressed as

$$P(E_t) \sim I_{cm}(E_{cm}, \Theta_{cm}) = t^3 \cdot f(v) \cdot n_{LAB}$$

where, $I_{cm}(E_{cm}, \theta_{cm})$ is the c.m. flux distribution of the fragments; f(v) is the c.m. velocity distribution of the fragments and n_{LAB} is the signal counts measured in the laboratory.

Results and Discussion

In the CS_2 photofragmentation experiment, Fischer Scientific analytical grade CS_2 was used without further purification. The initial velocity of the CS_2 molecules has been measured to be 4.6×10^4 cm/sec by the TOF chopper wheel experiment.

Figure 1 shows the TOF spectrum of CS fragments resulting from CS_2 photofragmentation by a pulsed ArF laser. The spectrum was obtained by accumulating TOF signals for about 1,000,000 laser shots at a molecular beam source angle of 10 degrees with respect to the detector axis and a fragment flight path length of 48.9 cm. It represents a signal to noise ratio greater than 10. The delay time of m/e = 44 ions in the detection system for the same operating conditions has been measured to be 53 microseconds. This value is used for calibrating the fragment flight times in the TOF spectrum.

The laboratory TOF distribution is transformed into c.m. recoil translational energy of the photofragments as shown in Figure 2. The curve clearly shows that a sharp rise at c.m. energy of 45.0 kcal/mol which corresponds to the formation of CS (v = 0) according to dissociation channel (1). The thermochemical limit of the vibrational excitation of this dissociation channel is v = 13. At c.m. translational energy lower than 18.6 kcal/mol, mixings occur in excited

Figure 1. Time-of-flight spectrum of CS fragments from photodissociation of CS_2 at 193 nm.

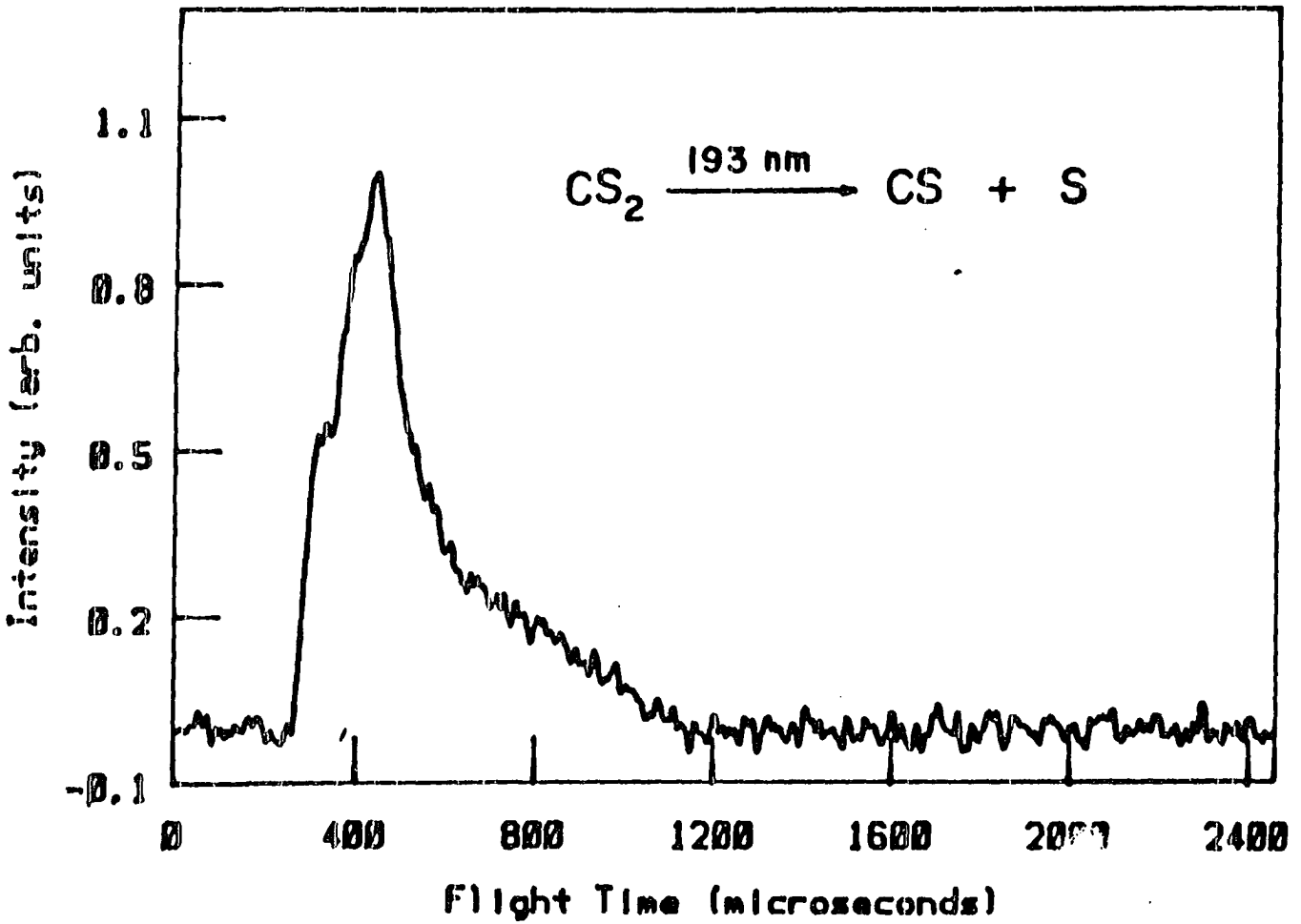
$CS_2 \xrightarrow{193\ nm} CS + S$
Intensity (arb. units)
1.1
0.8
0.5
0.2
-0.1
0
400
800
1200
1600
2000
2400
Flight Time (microseconds)

Figure 2. Translational energy distribution of fragments. The two assignment trains show the fragment translational energies for the photodissociation channels CS_2 ---> $C(^3P)$ + CS ($X\ ^1\Sigma$, v) and CS_2 ---> $S(^1D)$ + CS ($X\ ^1\Sigma$, v).

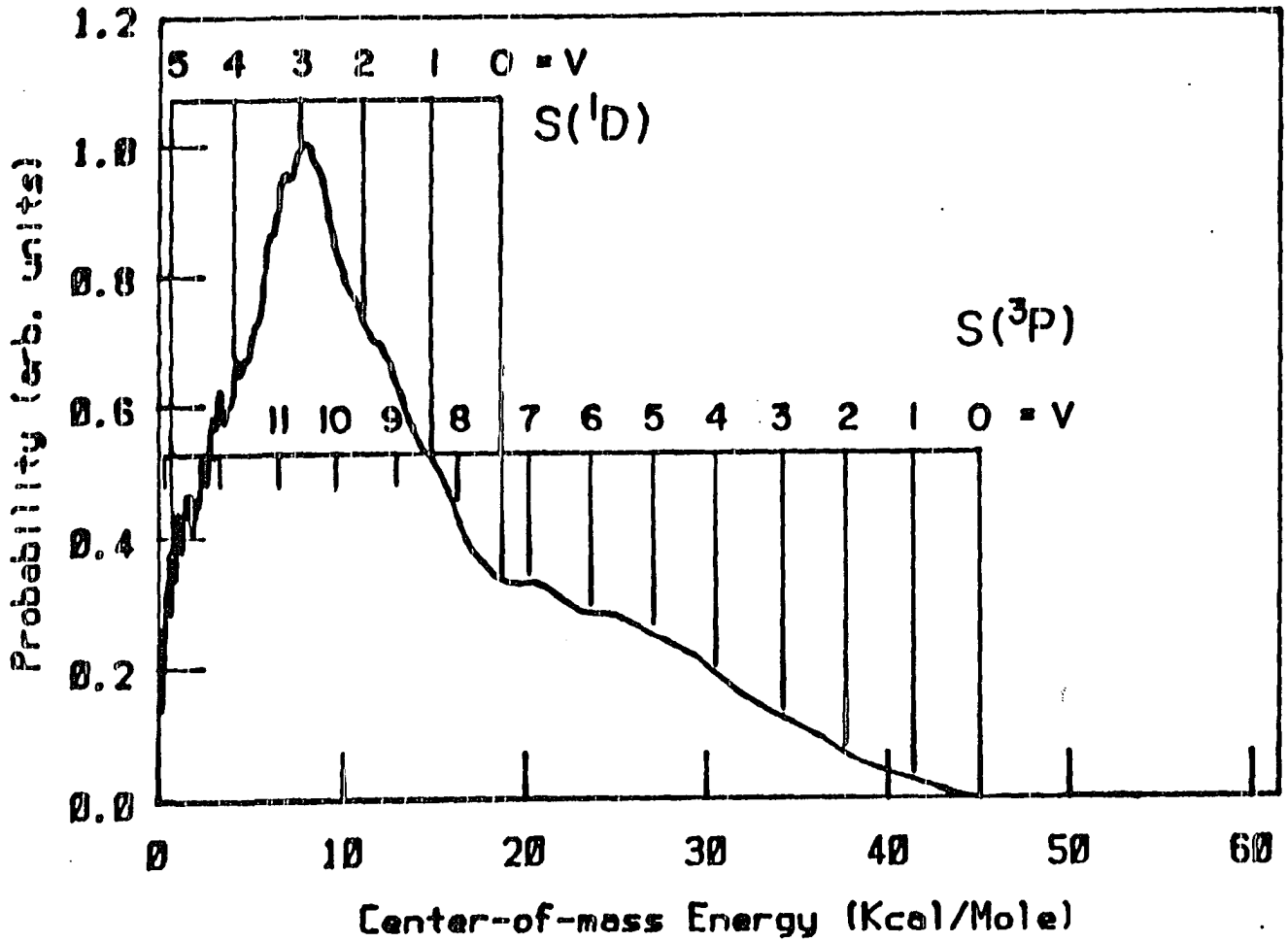
1.2
1.0
0.8
0.6
0.4
0.2
0.0
Probability (arb. units)
5 4 3 2 1 0 = V
S(¹D)
S(³P)
11 10 9 8 7 6 5 4 3 2 1 0 = V
0
10
20
30
40
50
60
Center-of-mass Energy (Kcal/Mole)

states between $CS_2 \longrightarrow CS(v = 0\text{-}5) + S(^1D)$ and $CS_2 \longrightarrow CS(v = 8\text{-}12) + S(^3P)$. Therefore, a single TOF spectrum can only produce a lower bound of the channel branching ratio for $S(^3P)/S(^1D)$. This is found by dividing the area between 18.6 and 45.0 kcal/mol by the area between 0 and 19.6 kcal/mol. In this analysis, a lower bound of the $S(^3P)/S(^1D)$ ratio of 0.38 is obtained.

For a complete study of the branching ratio $S(^3P)/S(^1D)$, information on the vibrational energy distribution and rotational energy distribution of the nascent CS fragment is needed. Dornhofer et al.[22] have shown that an intense ArF laser can distort the observed vibrational energy distribution due to a subsequent photon absorption by the CS fragments. in addition, a fraction of $CS(X\ ^1\Sigma^+, v>5)$ can photodissociate into $C(^3P)$ and $S(^3P)$. This results in an underestimation of the branching ratio in the direct detection method[18] and an ovrestimation of the branching ratio in the laser-induced fluorescence method.[23,25] A more elegant experimental method must be developed in the future in order to precisely determine the $S(^3P)/S(^1D)$ in CS_2 photodissociation at 193 nm.

References

1. M. N. R. Ashfold, M. T. Macpherson and J. P. Simons, Top. Current Chem. 86, 1 (1979).
2. W. M. Jackson, Adv. Photochem. 13, 1 (1986).
3. A. Kantrowitz and J. Grey, Sci. Rev. Instrum. 22, 328, 333 (1951).
4. J. B. Anderson and J. B. Fenn, Phys. Fluids 8, 780 (1965).
5. J. E. Scott Jr. and J. A. Phipps, Rarefied Gas Dynamics, Vol. 2, edited by J. H. de Leeuw (Academic Press, New York, 1967), p. 1337.

6. O. F. Hagena and H. S. Morton Jr., Rarefied Gas Dynamics, Vol. 2, edited by J. H. de Leeuw (Academic Press, New York, 1967), p. 1369.

7. Molecular Beam and Low Density Gasdynamics, edited by P. P. Wegener (Marcel Dekker, Inc., New York, 1974).

8. R. E. Smalley, L. Wharton and D. H. Levy, Acct. Chem. Res. 10, 139 (1977).

9. G. E. Busch, J. F. Cornelius, R.T. Mahoney, R. I. Morse, D. W. Schosser and K. R. Wilson, Rev. Sci. Instrum. 41, 1066 (1970).

10. K. R. Wilson, "Photofragment Spectroscopy of Dissociative Excited States", in Excited State Chemistry, edited by J. N. Pitts, (Gordon and Breach Science Publishers, New York, 1970).

11. S. R. Riley and K. R. Wilson, Faraday Discuss. Chem. Soc. 53, 132 (1972).

12. R. K. Sparks, K. Shobatake, L. R. Carlson and Y. T. Lee, J. Chem. Phys. 75, 3838 (1981).

13. R. G. W. Norrish and G. Porter, Proc. R. Soc. London Ser. A 200, 284 (1950).

14. A. B. Callear, Proc. R. Soc. London Ser. A 276, 401 (1963).

15. F. J. Wright, J. Phys. Chem. 64, 1648 (1960).

16. M. DeSorgo, A. J. Yarwood, O. P. Strausz and H. E. Gunning, Can. J. Chem. 43, 1886 (1965).

17. L. C. Lee and D. L. Judge, J. Chem. Phys. 63, 2782 (1975).

18. M. C. Addison, R. J. Donovan and C. Fotakis, Chem. Phys. Lett. 74, 1 (1980).

19. R. J. Hemley, D. G. Leopold, J. L. Roebber and V. Vaida, J. Chem. Phys. 79, 5219 (1983).

20. J. M. Ajello and S. K. Srivastava, J. Chem. Phys. 75, 4454 (1981).

21. M. Martin and R. J. Donovan, J. Photochem. 18, 245 (1982).

22. G. Dornhofer, W. Hack and W. Langel, J. Phys. Chem. 88, 3060 (1984).

23. S. Yang, A. Freedman, M. Kawasaki and R. Bersohn, J. Chem. Phys. 72, 4048 (1980).

24. V. R. McCrary, R. Lu, D. Zakheim, J. A. Russell, J. B. Halpern and W. M. Jackson, J. Chem. Phys. 83, 3481 (1985).

25. J. E. Butler, W. S. Drozdoski and J. R. McDonald, Chem. Phys. 50, 413 (1980).

26. A. Douglas, and I. Zanon, J. Chem. Phys. 42, 627 (1964).

27. R. T. Mahoney, Ph.D. Dissertation, University of California, San Diego, La Jolla, CA, 1971.

28. H. C. W. Beijerinck, R. G. J. M. Moonen and N. F. Verster, J. Phys. E 7, 31 (1974).

29. H. Shinohara and N. Nishi, J. Chem. Phys. 77, 234 (1982).

APPENDIX A. LASER MCS SYSTEM DESCRIPTION

The LASER MCS (multichannel scaler) was designed by Mr. Harold Skank of Ames Laboratory Instrumentation Services Group to provide control and data acquisition capabilities for the molecular beam laser photofragment mass spectrometer. The system consists of a Motorola 6809 microprocessor, functioning as the system central processor unit (CPU), the usual random access memory (RAM), sixteen kilobytes of control read-only memory (ROM), a teleprinter serial channel, and a number of special input-output (I/O) ports dedicated to the hardware required to control the experiment. The CPU runs a menu driven system, operating under a ROM based tasking system specifically designed for experiment support.

LASER MCS Hardware

The hardware of the LASER MCS consists of two separate chassis: (1) LASER MCS CONTROL and (2) LASER MCS MOTOR DRIVE. Since the implementation was developed about a local bus convention to simplify system extensions, the system hardware is modular with only the CPU requiring a specific bus slot dedicated to its use. The first chassis houses the LASER MCS CONTROL which contains the central decision making 6809 microprocessor (the CPU), a number of bus slots, and many specific I/O ports.

The specific I/O facilities in the LASER MCS system are described below:

I. Three triple sixteen-bit timer/counter boards used for:
   1. Phase-lock control of the chopper system (4 sixteen-bit sections).
   2. Variable modulo clock for angle motor step control (1 sixteen-bit section).
   3. Dual data counters for the Molecular Beam Timer and Gate system (2 sixteen-bit sections).
   4. Monitor timer for MCS operations (2 sixteen-bit sections).

II. Five twenty-bit parallel interface boards used for:
   1. MCS data transfers (1 board).
   2. MCS control transfers (1 board).
   3. X-Y display of stored spectrum data (1 board).
   4. Beam source chamber motor control (1 board).
   5. Molecular Beam Timer and Gate control (2 bits of 1 board).

III. One dual D/A (digital to analog converter) channel provides two channels of 12-bit resolution digital to analog conversion.

IV. A two-board multi-channel scaler provides up to 4096 channels of 16-bit data acquisition. In the present LASER MCS system the MCS uses only 1024 channels, and the advance from channel to channel is driven from the MCS time base. Special synchronization circuitry, driven by an optical sensor or the laser, depending upon the mode selection, ensures that individual sweeps are started at the proper time. Control commands (accessible from software) permit transfer of stored data from the MCS to the host processor. This transfer is done in a destructive-read fashion, thereby providing the means of clearing the MCS data memory area. Stop commands are executed

only at the end of complete traces, so that only entire traces are recorded. In addition other special circuitry monitors the most significant data bit and provides a flag to the host processor when data has reached half-scale, permitting transfer to the host processor before data loss occurs.

In the LASER MCS system the high speed data latches reduce the scaler dead time to approximately 17 nanoseconds per channel, while memory cycle timing considerations limit the channel dwell time to an approximate minimum of 300 nanoseconds. Fully synchronous counters are used to reduce the state transition time after a count pulse. These counters, along with their channel synchronization circuitry limit the maximum count-rate within a channel to approximately 25,000,000 counts per second.

A second separate chassis houses the power supply for the motors and their sequencers and power amplifiers. The motor power supply is simply a 36 volt transformer driving a bridge rectifier and choke-input filter and provides approximately 30 volts at 25 amps.

Each of the motors is driven by an interpolated step sequencer that provides two orthogonal phases with 16 steps per cycle. The phases are designed to approximate sine and cosine drive signals to the motor drive amplifiers. While this technique increases the power requirements, it provides enhanced resolution on the angle drive motor and reduce the vibration inherent to stepping motor drive systems. For the TOF wheel chopper motor (a hysteresis synchronous motor) this drive scheme

provides the means by which the extremely broad drive range is achieved. In both cases the sequencer circuit drives a 4-phase power amplifier which provides a controlled current drive to the following motor. For the stepping motor driving the beam source chamber this serves to flatten the torque-speed characteristics and permits the motors to be driven at higher speeds.

LASER MCS Software

The software of the LASER MCS system is essentially a menu driven program called MENU09. MENU09 is written in PL/W which is a block structured computer language developed by WINTEK CORPORATION, Lafayette, Indiana. The MENU09 permits the user to invoke calls to the various system tasks and also provides the serial I/O system utilities to facilitate operator communication with the system.

The system is automatically initiated on power-on with MENU09 being the only active task. As a result, the available prompts from the master menu (MOVE LASE CHOP MBGT STOP PRIN) are typed out to the user. At each level in the menu system a menu entry may be selected by responding with one of the four letter commands listed by the current level menu. Upon the entry of the carriage return, the system progresses to the next deeper level of menu selections until the most recent entry corresponds to an executable task. Then control passes to the task, and the parameter entry and task execution starts. Should an incorrect keyboard sequence be entered, the current level menu will be printed again. A carriage return with no corresponding keyboard entry

will move back up the menu tree one level and permit selection of a different branch of responses. At the completion of any task, the current level menu is repeated for possible selection of another task.

The menu elements in the LASER MCS system are as follows:

I. MOVE — Master command to select movement of the molecular beam source chamber. Typing this command will summon a second level menu with the following available commands.

   1. SETA — Set angle registers. This executable task permits the operator to provide the proper initial angular information for a system cold start. Under normal operation, all further angle record keeping is automatic.
   2. READ — Read and print the contents of angle registers. This command permits operator query of present position of the molecular beam source chamber.
   3. SOUR — Move the molecular beam source chamber to an operator selected angle. Typing this command leads to a query "ANGLE?", to be followed by an angle entry by the operator. A carriage return with no numeric entry provides an escape from the task, while a numeric entry will start motion of the beam source chamber to the designated target angle. A "MOTION COMPLETE" message is issued at the end of angle motion and an "OUT OF RANGE" message is issued if the numeric input string is too long, or if it contains non-numeric characters. The current executable angular range has been set to be from -90 to +90 degrees. While the beam source chamber is actually in motion

the system is disabled to other keyboard commands to prevent interference with the motor drive routines.

II. LASE — An executable master menu command to permit entry to the LASER MCS data acquisition mode. In response to this command the system clears the data storage area for the MCS data in the laser photofragmentation experiment, then returns a request to select and enter the dwell time multiplier. (The dwell time per MCS channel is the product, 20 nanoseconds/channel times the multiplier.) Following entry of the dwell time multiplier, the operator is asked to enter the time limit desired for the MCS run, then the experiment is started. In order that the X-Y display might provide a reliable indication of the data acquisition process, the contents of the MCS are added to the contents of the 6809 memory at 6 second intervals. If the contents of the MCS memory should reach half-scale in a shorter period, then the transfer is done at that time. In either case the transfer time is not included in the total data acquisition time, so that the operator specified experiment time entered above is the actual data collection time.

III. CHOP — An executable master command to permit entry of control parameters to the time of flight (TOF) chopper wheel system. In response to this command the system clears the data storage area for the data in TOF chopper wheel experiment, then returns a chopper wheel speed query, permitting selection of chopper wheel rotational speed in increments of tenths of Hz. When the chopper wheel speed has been set, the system enters a wait state until the chopper phase-locked oscillator has stabilized at the specified

speed. Following the stabilization wait state, the operator is asked to enter the time limit desired for the chopper wheel run, and the TOF chopper wheel experiment is started. In order that the X-Y display might provide a reliable indication of the data acquisition process, the contents of the MCS are added to the contents of the 6809 memory at 6 second intervals. If the contents of the MCS memory should reach half-scale in a shorter period, then the transfer is done at that time, and in either case the transfer time is not included in the total data acquisition time, so that the operator specified experiment time entered above is the actual data collection time.

IV. MGBT — Executable master menu command to enter the data acquisition mode for the molecular beam gate and timer experiment. Upon receipt of this command, after first checking for another experiment already in progress, the system clears the display area of memory, and responds with a query for the initial beam source angle. Further queries request a step angle for the incrementing the source position and the number of steps desired for the experiment. Since the data collection time for each point is determined by the hardware setup on the MBG&T (Molecular Beam Gate and Timer) module, the system prompts the operator to provide the necessary settings. As a matter of record keeping, the system further requests entry of the time setting, after which the experiment is started. The system provides for appropriate angle motions, control of the MBG&T module, and displays both counter channels of MBG&T data versus angle increment until the experiment

is completed, or until it is terminated by a STOP command. At the present time this command is not needed for either the TOF chopper wheel experiment or the laser photofragmentation experiment.

V. STOP — Executable master menu command to terminate a currently running experiment. This command is different from the other menu commands in that while it may be called from the keyboard like other commands, it is also routinely called from the operating system as the normal completion of an experiment. In either event it shuts down the currently operating experiment and provides closing status information concerning which experiment had been running and the elapsed experiment time in minutes. Then for the TOF chopper wheel experiment it returns the chopper wheel rotational speed to 40 Hz.

VI. PRIN — Executable master menu command to provide print out of the MCS experiment data. Upon recognition of this menu command the system responds with a query for the first channel number desired in the print out range. The operator response to the first channel query is followed by another query requesting the last MCS channel number in the range. Following the operator response to the second query, the channel output operation begins. The format for each line provides for print out of each decimal channel number ending in zero, followed by ten channels of data. This line format is continued until the range specified is satisfied.

APPENDIX B. CALCULATION ON MOLECULAR BEAM GENERATION SYSTEM

The molecular beam generation system consists of three vacuum chambers: (1) nozzle discharge chamber, (2) collimation chamber, and (3) scattering chamber. The estimated pumping speed of the 20" diffusion pump and the Halo baffle in the nozzle source chamber is about 10,500 l/s. The collimation chamber is evacuated by a 6" diffusion pump with an estimated effective pumping speed of 950 l/s. The 10" diffusion pump employed to pump the scattering chamber has an pumping speed of about 1,830 l/s.

For a nozzle diameter of 0.005", Argon gas at a stagnation pressure of 760 Torr, and a nozzle temperature of 300 K, the mass flow (G) through the nozzle is

$$G = 14.3\ D^2\ P\ [\frac{\text{Torr liter}}{\text{second}}]$$

where, D = diameter of nozzle opening in centimeter = 0.0127 cm

P = nozzle stagnation pressure in Torr = 760 Torr.

Thus, $G = 14.3 \times (0.0127)^2 \times 760$

$$= 1.75\ [\frac{\text{Torr liter}}{\text{second}}].$$

The normal pressure in the nozzle discharge chamber is, therefore,

$$P_1 = \frac{G}{S_1}$$

$$= \frac{1.75}{10{,}500} \quad \frac{[\text{Torr liter/second}]}{[\text{liter/second}]}$$

$$= 1.67 \times 10^{-4}\ [\text{Torr}].$$

The solid angle subtended by the 0.040" (0.102 cm) diameter skimmer is

$$\delta\Omega = \frac{(\frac{\Pi}{4})\ (0.102)^2}{0.762^2}$$

$$= 1.41 \times 10^{-2}\ \text{[sterad]}.$$

For an isentropic expansion, the number density on the beam axis at the skimmer entrance is approximated by

$$n_{sk} = 1.13 \times 10^{-5}\ \frac{G}{X^2}\ \ [\frac{\text{molecules}}{\text{cm}^3}]$$

$$= 0.161\ n\ (\frac{X}{D})^{-2}$$

where, n = molecular density in the nozzle,

in "molecules/cm^3",

X = distance from nozzle to skimmer, in "cm".

At one atm and 300 K, the molecular density is

$$n = 2.4 \times 10^{19}\ \text{[molecules/cm}^3\text{]}.$$

So that,

$$n_{sk} = 0.161 \times (2.4 \times 10^{19}) \times (\frac{0.762}{0.0127})^{-2}$$

$$= 1.1 \times 10^{15}\ \text{[molecules/cm}^3\text{]}.$$

The root-mean-square velocity of argon at 300 K is

$$v_{Ar} = \text{SQRT}\ (\frac{8RT}{\Pi M})$$

$$= \text{SQRT}\ (\frac{8 \times 8.314 \times 10^7 \times 300}{\Pi \times 40})$$

$$= 4.0 \times 10^4\ \text{[cm/sec]}.$$

After the argon gas comes out of the nozzle, its velocity will reach a terminal speed which is about 1.29 times that of the initial root-mean-square velocity, depending upon the expansion conditions.

Then,

$$v_{Ar} = (4.0 \times 10^4) \times 1.29$$
$$= 5.2 \times 10^4 \text{ [cm/sec]}.$$

Thus, the beam flux (I) at skimmer entrance is

$$I_{sk} = n_{sk} \times v_{Ar}$$
$$= (1.10 \times 10^{15}) \times (5.2 \times 10^4)$$
$$= 5.7 \times 10^{19} \text{ [molecules/cm}^2 \text{ sec]}.$$

The number of atoms entering the collimation chamber is

$$N_{co} = (5.7 \times 10^{19}) \times (\frac{\pi}{4} \times (0.102)^2)$$
$$= 4.7 \times 10^{17} \text{ [molecules/sec]}$$
$$= 1.4 \times 10^{-2} \text{ [Torr liter/sec]}.$$

Since the collimation chamber is evacuated at a pumping speed of 950 liter/sec, the pressure in this region is maintained at

$$P_2 = \frac{1.4 \times 10^{-2}}{950}$$
$$= 1.5 \times 10^{-5} \text{ [liter/sec]}.$$

The solid angle subtended by the 0.060" (0.152 cm) diameter collimator is

$$\delta\Omega = \frac{(\frac{\pi}{4})(0.152)^2}{3.937^2}$$
$$= 1.2 \times 10^{-3} \text{ [sterad]}.$$

Then, the number density on the beam axis at collimator tip is approximated by

$$n_{co} = 0.161 \times (2.4 \times 10^{19}) \times \frac{0.0127}{3.937^2}$$

$$= 4.1 \times 10^{13} \text{ [molecules/cm}^3\text{]}.$$

Thus, the beam flux at the tip of collimator is

$$I_{co} = n_{co} \times v_{Ar}$$

$$= (4.1 \times 10^{13}) \times (5.2 \times 10^{4})$$

$$= 2.1 \times 10^{18} \text{ [molecules/cm}^2 \text{ sec]}.$$

The number of atoms entering the scattering chamber is

$$N_{mc} = (2.1 \times 10^{18}) \times (\frac{\pi}{4} \times 0.152^2)$$

$$= 3.8 \times 10^{16} \text{ [molecules/sec]}$$

$$= 1.2 \times 10^{-3} \text{ [Torr l/sec]}.$$

The pumping speed in the scattering chamber is 1830 l/sec, therefore, the pressure in the scattering chamber is

$$P_3 = (1.2 \times 10^{-3}) / 1830$$

$$= 6.6 \times 10^{-7} \text{ [Torr]}.$$

Finally, the number density on the beam axis at scattering center is approximated by

$$n_{sc} = 0.161 \times (2.4 \times 10^{19}) \times (\frac{0.0127}{5.334})^2$$

$$= 2.2 \times 10^{13} \text{ [molecules/cm}^3\text{]}.$$

APPENDIX C. CALCULATION ON NUMBER OF FRAGMENTS ARRIVING IN IONIZATION REGION

A carbon disulfide (CS_2) beam with a pressure of 150 Torr is used as the example for this calculation. Following a calculation procedure similar to that in Appendix B, one obtains a number of density of CS_2 in the scattering zone of about 4.3×10^{12} molecules/cm^3.

Assume that the laser beam is focused to 2mm x 6mm to match the molecular beam which has a cone-shaped spread with a diameter of 2 mm in the scattering center. Then, the scattering volume is approximately 0.020 cm^3 and

n_{sc} = the number of CS_2 molecules in the scattering zone

$= (4.3 \times 10^{12}) \times (0.020)$

$= 8.6 \times 10^{10}$.

Assume that (1) the laser beam is perfectly intersected with the molecular beam, (2) all CS_2 molecules arrived in the scattering zone are photodissociated, and (3) all product fragments are spherically distributed. Then, for the following instrumental parameters:

A = acceptable area of ionizer (diameter = 0.125")

$= 0.076\ cm^2$,

l = distance from scattering center to ionizer

= 48.9 cm,

the fraction of product fragments arriving in the ionizer, F, can be calculated.

$$F = \frac{0.076}{4\pi \times 48.9^2}$$

$$= 2.6 \times 10^{-6}.$$

Finally, one obtains number of product fragments arriving in the ionizer:

$$N_{fg} = (8.6 \times 10^{10}) \times (2.6 \times 10^{-6})$$

$$= 2.2 \times 10^{5}.$$

APPENDIX D. LAB TO C.M. TRANSFORMATION

The results of photofragmentation time-of-flight experiments are normally reported in terms of relative differential cross sections $I_{LAB}(v,\Theta_{LAB})$ for a given range of laboratory velocity v and solid angle Θ_{LAB}. Experimental or laboratory cross-sections and angles are usually transformed into center-of-mass coordinates. The transformation is

$$I_{LAB}(v,\Theta_{LAB}) = (\frac{v^2}{u^2})I_{cm}(u,\Theta_{cm}) \tag{1}$$

where $I_{cm}(u,\Theta_{cm})$ is the center-of-mass cross section, v is the laboratory velocity and u is the center-of-mass velocity. Since an electron impact ionizer is sensitive to number density and not flux, the lab signal is given by

Flux = (Number density of molecules in beam)
x (Velocity of molecules in beam)

$$I_{LAB}(v,\Theta_{LAB}) = n_{LAB}(v,\Theta_{LAB}) \times v$$

Thus,

$$n_{LAL}(v,\Theta_{LAL}) \sim (\frac{v}{u^2})I_{cm}(u,\Theta_{cm}). \tag{2}$$

However, we measure this distribution as a function of time, not velocity, and since $t = l/v$ (l is the flight path length), we have

$$n_{LAB}(t,\Theta_{LAB}) \times (\frac{dt}{dv}) \sim (\frac{v}{u^2})I_{cm}(u,\theta_{cm})$$

$$n_{LAL}(t,\Theta_{LAL}) \sim (\frac{v^2}{l}) \times (\frac{v}{u^2})I_{cm}(u,\theta_{cm})$$

$$n_{LAB}(t,\Theta_{LAB}) \sim (\frac{v^3}{u_2 l})I_{cm}(u,\theta_{cm}). \tag{3}$$

Furthermore, it is more convenient to discuss the center-of-mass distribution in terms of energy rather than velocity, and since $E \sim u^2$,

$$\frac{dE}{du} = mu.$$

Thus, $I_{cm}(u,\theta_{cm}) = (mu)I_{cm}(E,\theta_{cm})$

and $(\frac{v^3}{u^2 l})I_{cm}(u,\theta_{cm}) = (\frac{mv^3}{ul})I_{cm}(E,\theta_{cm})$.

Also, $n_{LAB}(t,\Theta_{LAB}) \sim (\frac{v^3}{ul})I_{cm}(E_{cm},\theta_{cm})$ (4)

and

$$n_{LAB}(t,\Theta_{LAB}) \sim (\frac{l^2}{t^3 u})I_{cm}(E_{cm},\Theta_{cm}). \tag{5}$$

Since the flight path, l, is constant, equation (5) becomes

$$n_{LAB}(t,\Theta_{LAB}) \sim (\frac{1}{ut^3})I_{cm}(E_{cm},\Theta_{cm}) \tag{6}$$

The equation (6) may be expressed as

$$I_{cm}(E_{cm},\theta_{cm}) \sim (t^3 u) n_{LAB}(t,\theta_{LAB}), \qquad (7)$$

where, t is the flight time.

APPENDIX E. OPERATIONS OF EXCIMER LASER

The Questek model 2260 excimer laser is a multigas ultraviolet laser which puts out four intense single frequency laser lines, depending upon the fuel gas mixture. Since the laser is equipped with a microprocessor controlled unit, the operation is fairly simple. However, the company has not supplied a complete operational manual although they have a "800" toll free number for answering questions and providing technical support. The purpose of this appendix section is to describe procedures for some essential operations and tests which are not completed or not included in the current operational manual.

A. Procedure for normal operation:

1. Set the GAS SELECT switch for the excimer emission line to be used.
2. Set the INT/EXT TRIGGER switch to INT for internal trigger mode.
3. Set the COMMAND CHARGE ON/OFF switch to ON.
4. Set the POWERLOK ON/OFF switch to ON.
5. Open cooling water valve and verify its flow.
6. Close the beamstop at the laser output port.
7. Turn on the main circuit breaker and key switch on the line power panel.
8. Wait for 15 minutes until the countdown clock on the numerical display reads zero.
9. Press and release the EVACUATE key to evacuate the chamber.
10. Open all valves in supply fuel gas lines.

11. Press and release the PURGE key. (May repeat this action).
12. Press and release the AUTOFILL key to initiate the automatic gas filling sequence.
13. Set pulse energy and repetition rate by pressing and releasing the PULSE ENERGY and REP RATE key.
14. Press the green LASER ON switch to start the laser.

B. Procedure for cleaning the laser cavity optics (output MgF_2 coupler window and rear reflection MgF_2/Al mirror):

1. Evacuate the gas chamber and purge two times with helium (Buffer A) gas.
2. Fill the gas chamber with Buffer A gas to 1000 mbar.
3. Press and release the CODE key.
4. Press and release the ENTER key.
5. Type "30" on the numerical keypad.
6. Carefully loosen the three holding screws on the front output window holder and remove the holder from the gas chamber wall.
7. Remove the MgF_2 window from the holder.
8. Lay the window on the lens cleaning paper.
9. Use optics polishing slush (mixture of Tin Oxide lens polishing powder and methanol) to polish the window.
10. Remove the polishing material with small amount of methanol.
11. Examine the window surface.
12. Repeat steps 9-11 if necessary.
13. Put the window back to its holder.
14. Mount the window holder on the gas chamber wall.

15. Follow steps 7-14 for the rear mirror.

C. Procedure for aligning the output laser beam:

1. Place a piece of thermal paper on the output coupler mirror holder mount.
2. Slightly press the thermal paper against the three mounting screws to define the reference triangle.
3. Fire the laser for one shot and inspect the burnt spot on the reference triangle.
4. Turn the appropriate adjustment screws on the front and back of the gas chamber wall.
5. Repeat steps 1-4 if necessary.

D. Procedure for checking the control voltage from the high voltage DC power supply:

1. Remove the front chassis panel.
2. Remove the plastic cover on the driver board.
3. Use an oscilloscope to measure the voltage level on TP1 (Test Point 1) on the driver board. A value of 10 volts is equivalent to 32 kV of control voltage.

E. Procedure for bypassing Error 90 (zero output) for some component tests:

1. Press and release the CODE key.
2. Type "7" on the numerical keypad and hit the ENTER key.
3. Type "1284" on the numerical keypad and hit the ENTER key.

4. Type "0" on the numerical keypad and hit the ENTER key.

F. Procedure for replacing vacuum pump bypass solenoid valve and the connection hose to the halogen charcoal filter:

1. Make sure the cooling water valve is closed and the main line power is off.
2. Remove the top and back chassis panels of the laser.
3. Short out the high voltage capacitor banks and the capacitors on the high voltage trigger circuit board by using a long screwdriver to make a contact with the laser chassis.
4. Disconnect the electrical connectors to the high voltage trigger circuit board.
5. Remove the high voltage trigger circuit board.
6. Remove the Thyratron HV trigger cover panel.
7. Remove the Mylar insulation sheet.
8. Remove the two HV capacitor banks.
9. Remove the Thyratron HV trigger unit.
10. Loosen the hose clamps and remove the flexible hoses.
11. Replace the solenoid valve.
12. Reverse the sequence for reinstalling the components.

G. Procedure for inspecting the failure of the secondary capacitors in the high voltage discharge assembly in the gas chamber:

1. Evacuate the gas chamber and purge two times with helium.
2. Fill the gas chamber with helium to 1700 mbar.
3. Set repetition rate at 10 Hz.

4. Bypass the Error 90 using the Procedure E described above.
5. Start the laser.
6. Use a business card to check if any lasing occurs. (One should not see lasing phenomenon.)
7. Use a 1/2" thick plexiglas plate and carefully look through the output window to inspect the homogenity and the colors in the preionization units of the discharge region. (A purple color indicates normal operation whereas a yellowish color indicates a failure in the secondary capacitor.)

H. Procedure for replacing the secondary capacitors in the high voltage discharge assembly and/or the set of nickel electrodes:

1. Evacuate the gas chamber and purge two times with helium.
2. Fill the gas chamber with helium to 1300 mbar.
3. Follow steps 1-9 in Procedure F.
4. Carefully remove the G-10 assembly unit.
5. Inspect and replace the damaged capacitor and/or the nickel electrodes.
6. Reverse the sequence for reinstalling the components.
7. Follow the procedure for passivating the gas chamber.

I. Procedure for passivating the gas chamber:

1. Close cooling water valve.
2. Evacuate the gas chamber and purge two times with helium.
3. Fill the gas chamber with halogen gas (F_2/He) to 700 mbar then with helium gas to a total pressure of 1700 mbar.

4. Set repetition rate at 1 Hz.
5. Bypass the Error 90 using the Procedure E described above.
6. Start the laser and observe the red light coming out of the output window of the laser cavity. (The red light is caused by the fluorescence of excited fluorine molecules.)
7. Graduately increase up the repetition rate.
8. Let this passivation proceed for at least one hour. (A complete passivation procedure will take at least 24 hours.)
9. When the passivation is completed, evacuate the chamber and purge 2 times with helium.

APPENDIX F. COMPUTER PROGRAMS

Many Fortran programs have been written in FORTRAN-77 language for manipulating TOF data and general computational purposes, but only two of the most useful ones are included in this appendix section. A useful graphics plotting program called HGRAPH has been installed in the LSI-11/23 computer system library. Moreover, a command file which has the same filename with a filename extension of "com" has been created for linking the HGRAPH subroutine program to the fortran compiler. Therefore, the data plotting tasks can be done by invoking the HGRAPH instructional commands with proper desired parameters in the main fortran program.

All data stored in another file called A.DAT can be invoked by the OPEN instructional command and transferred to be stored in an array for later computations. However, a CLOSE instructional command must be included at the end of the data transferring task. Some important experimental variables are requested on the computer terminal as the input data, so that the operator must enter the corresponding values according to the questions. All constant and variable names and meanings are explained in the comment statement "C" in the program, thus one can quickly understand the whole computation procedure. The results of computations can be output on the graphic terminal screen, the line printer or plotter as desired.

FLIGHT.FOR is used to plot the time of flight spectra as seen on the oscilloscope during the data acquisition periods. However, a slight

modification in the program is needed to correct the flight time of molecules due to the delay time that the ions spend in the mass spectrometer in both laser photofragmentation and chopper wheel TOF experiments. In addition, another calibration which relates to the wheel rotational direction in the chopper wheel experiment (described in the main text) must be taken into consideration.

ENERGY.FOR is used to convert the laboratory TOF data to c.m. flux as a function of c.m. energy for the laser photofragmentation TOF experiments. When running this program, input onformation is requested concerning the channel dwell time, the ion drift time in the mass spectrometer, the fragment flight path, the laboratory angle between beam source and detection system axis, the parent beam initial velocity and the masses of the two product fragments. The results of this transformation are then presented as a plot of probability versus c.m. energy.

```
C*********************************************************************
C     Filename:FLIGHT.FOR
C     FLIGHT.FOR is fortran program for plotting time of flight
C     spectra either for the time of flight chopper wheel experiments
C     or for the laser photofragmentation experiments.
C*********************************************************************
C
C     BAKAVG = average number of background channels for
C              background subtraction.
C     BAKSUM = sum of counts of some background channels.
C     BIG    = maximum counts after subtracting average background counts.
C     DWELL  = dwell time per channel in time-of-flight data,
C              in "microsecond per channel".
C     IPEAK  = channel number at maximum counts.
C     Y(I)   = intensity array.
C     T(I)   = flight time from scattering center to detector (array).
C
C     ---------------------------------------------------------------
      REAL Y(1024), T(1024)
      BYTE DATE(11)
C
C     Open an input data file called "A.DAT" and store in an array.
      OPEN(UNIT=22, NAME='A.DAT', TYPE='OLD')
      READ(22,*,END=3100) (Y(I), I=1,1024)
C
C     Smooth the curve
C
3100  DO 3500 I = 2 , 1023
      Y(I) = (Y(I-1) + 2. * Y(I) + Y(I+1)) / 4.
3500  CONTINUE
      DO 3700 I = 2 , 1023
      Y(I) = (Y(I-1) + 2. * Y(I) + Y(I+1)) / 4.
3700  CONTINUE
C
C     Enter today's date on the terminal.
      TYPE 400
      ACCEPT 100, DATE
C     Enter dwell time per channel (channel width) on the terminal.
      TYPE 410
      ACCEPT 110, DWELL
C
C     Find the maximum signal
C
      DO 6000 I = 1 , 1024
      IF(I .GE. 1023) GO TO 6000
      IF(Y(I) .LE. BIG) GO TO 6000
      BIG = Y(I)
      IPEAK = I
6000  CONTINUE
C
C     Calculate average background counts
C
      BAKSUM = 0.
      DO 6500 I = 600 , 899
      BAKSUM = BAKSUM + Y(I)
6500  CONTINUE
      BAKAVG = BAKSUM / (899. - 600. + 1.)
C
C     Subtract background counts
C
```

```
      DO 7000 I = 1 , 1024
      IF(I .GT. 1023) GO TO 6800
      Y(I) = Y(I) - BAKAVG
      GO TO 7000
6800  Y(I) = 0.
7000  CONTINUE
      BIG = BIG - BAKAVG
C
C     Normalize the spectrum
C
      DO 7500 I = 1 , 1024
      T(I) = I * DWELL
      Y(I) = Y(I) / BIG
7500  CONTINUE
C
C     Output to terminal (logic device = 7) or line printer
C     (logic device = 6)
      WRITE(7,30) BIG, IPEAK
      WRITE(7,40) BAKAVG
C
30    FORMAT(F8.0, 10X, I7)
40    FORMAT(F9.0)
100   FORMAT(11A1)
110   FORMAT(F5.1)
400   FORMAT(X, 'Enter today''s DATE in dd-mmm-yy format')
410   FORMAT(X, 'Enter channelwidth (DWELL) in microseconds in F5.1 form
     *at')
700   FORMAT(X, 'Date: ',11A1)
710   FORMAT(X, 'The dwell time per MCS channel in TOF data is ',F5.1,
     *' microseconds')
780   FORMAT(X, 'The peak is at channel number ', I5, '.')
790   FORMAT(X, 'The averaged counts for background subtraction is '
     *, F9.0,  ' counts.')
C
C     This section is to use HGRAPH subroutine program to plot out
C     Intensity (Y-axis) vs Flight time (X-axis).
C     Subroutine INIPLT sets up maximum size of the plot (10.25" x 7.25")
      CALL CHOICE(IUNIT)
      CALL INIPLT(IUNIT, 10.25, 7.25)
      CALL SCALE(0., 2062., -.1, 1.2)
      CALL AXIS(400., .3, 'Flight Time (microseconds)',
     F26, 2, 0, 'Intensity', 9 , 2, 1)
      CALL DASHLN(T, Y, 1024, 1, 0, 0, 0, 0)
      CALL INILGN(5.5, 7.5, 4., 5.5)
      CALL WRILGN('CS2, 0 C ', 9, 0, 0, 0, 1)
      CALL WRILGN('Laser 193nm', 11, 0, 0, 0, 1)
      CALL ENDLGN
      CALL ENDPLT
      CLOSE(UNIT=22)
      STOP
      END
```

```
C*****************************************************************
C       Filename: ENERGY.FOR
C       ENERGY.FOR is a FORTRAN program for converting laboratory
C       time-of-flight data into center-of-mass flux as a function
C       of center-of-mass energy for laser photofragmentation
C       time-of-flight experiments.
C*****************************************************************
C
C       ANGcm  = angle between fragment beam and detector axis in c.m.
C                frame, in "degree".
C       ANGlab = angle between nozzle beam axis and detector axis,
C                in "degree".
C       BAKAVG = averaged number of bachground channels for
C                background subtraction.
C       DRIFT  = ion drift time at that particular mass in "microseconds".
C       DWELL  = dwell time per channel in time-of-flight data,
C                in "microsecond per channel".
C       ENGYcm = kinetic energy of fragments in c.m. frame in "Kcal/mol".
C       FLUXcm = fragment flux in c.m. frame in "(counts)(cm)
C                (microsecond**2)".
C       PATH   = product flight path, in "centimeter". (48.9cm)
C       RDMASS = reduced mass of system, in "a.m.u.".
C       VELbm  = parent beam velocity obtained from time of flight
C                measurements, in "centimeter/second".
C       VELlab = fragment beam velocity in "cm/s".
C
C---------------------------------------------------------------------
C
        REAL*4 MASSfa, MASSfb
        REAL*4 Y(1024), ENGYcm(1024), INTENS(1024)
        BYTE DATE(11)
C       Define constants for calculations and unit conversions.
C       Constant C1 is the Avogadro's number.
C       Constant C2 is a anglular conversion factor from radian to degree.
C       Constant C3 is a energy conversion factor from erg to Kcal/mol.
        C1 = 6.022045E+23
        C2 = 57.29578
        C3 = 1.439956E-13
C
C       Open an input data file called "A.DAT" and store in an array.
        OPEN(UNIT=22, NAME='A.DAT', TYPE='OLD')
        READ(22,*,END=3100) (Y(I), I=1,1024)
C
C       Smooth the curve
C
3100    DO 3500 I = 2 , 1023
        Y(I) = (Y(I-1) + 2. * Y(I) + Y(I+1)) / 4.
3500    CONTINUE
        DO 3700 I = 2 , 1023
        Y(I) = (Y(I-1) + 2. * Y(I) + Y(I+1)) / 4.
3700    CONTINUE
C
C       Enter today's date on the terminal.
        TYPE 400
        ACCEPT 100, DATE
C       Enter dwell time per channel (channel width) on the terminal.
        TYPE 410
        ACCEPT 110, DWELL
C       Enter ion drift time in microseconds.
        TYPE 420
```

```
      ACCEPT 120, DRIFT
C     Enter fragment flight path length on the terminal.
      TYPE 430
      ACCEPT 130, PATH
C     Enter lab angle (parent beam vs. detector axis) on the terminal.
      TYPE 440
      ACCEPT 140, ANGlab
C     Enter parent initial beam velocity in "cm/s" on the teminal.
      TYPE 450
      ACCEPT 150, VELbm
C     Enter masses of fragments A and B in a.m.u.(atomic mass unit)
C     on the terminal; fragment A = detected fragment.
      TYPE 460
      ACCEPT 160, MASSfa, MASSfb
C
C     Calculate reduced mass of fragments
      RDMASS = MASSfa * MASSfb / (MASSfa + MASSfb)
C
C     This section is to substract background counts from detected
C     signal counts
C     Make sure the this range has not contained signal counts.
C
      BAKSUM = 0.
      DO 4000 I = 600 , 899
      BAKSUM = BAKSUM + Y(I)
4000  CONTINUE
      BAKAVG = BAKSUM / (899. - 600. + 1.)
      DO 4500 I = 1 , 1023
      LIMIT = I
      DATA = Y(I) - BAKAVG
      TIME = I * DWELL - DRIFT
      IF (TIME .GT. 0.) THEN
          VELlab = (PATH / TIME) * 1.0E+6
          VELcmY = VELlab * SIN(ANGlab/C2)
          VELcmX = VELlab * COS(ANGlab/C2) - VELbm
          ANGcm = ATAN2(VELcmY,VELcmX) * C2
          VELcm = SQRT(VELcmX**2 + VELcmY**2)
          FLUXcm = (TIME**3) * VELcm * DATA * 1.0E+6
          IF(ANGcm .GT. 90.) GO TO 4501
          IF(FLUXcm .GT. BIG) THEN
              BIG = FLUXcm
              IPEAK = I - 1
              ENDIF
          ENDIF
4500  CONTINUE
4501  WRITE(6,*)
C
C     Output to terminal (logic device = 7) or line printer
C     (logic device = 6)
      WRITE(6,700) DATE
      WRITE(6,710) DWELL
      WRITE(6,720) DRIFT
      WRITE(6,730) PATH
      WRITE(6,740) ANGlab
      WRITE(6,750) VELbm
      WRITE(6,760) RDMASS
      WRITE(6,770) VELcm
      WRITE(6,780) IPEAK
      WRITE(6,790) BAKAVG
      WRITE(6,800) LIMIT
```

```
      WRITE(6,900)
      WRITE(6,910)
C
C     This section is to calculate center-of-mass angle,
C     energy, and flux.
C
      DO 5000 I = 1 , 1024
      IF (I .LT. 1023) DATA = Y(I) - BAKAVG
      TIME = I * DWELL - DRIFT
      IF (TIME .GT. 0.) THEN
          VELlab = (PATH / TIME) * 1.0E+6
          VELcmY = VELlab * SIN(ANGlab/C2)
          VELcmX = VELlab * COS(ANGlab/C2) - VELbm
          ANGcm = ATAN2(VELcmY,VELcmX) * C2
          VELcm = SQRT(VELcmX**2 + VELcmY**2)
          VEL = VELcm * (MASSfa + MASSfb) / MASSfb
          ENGYcm(I) = .5 * C3 * (RDMASS/C1) * VEL**2
          FLUXcm = (TIME**3) * VELcm * DATA * 1.0E+6
      ELSE
          TIME = 0.
          ANGcm = 0.
          ENGYcm(I) = 0.
          FLUXcm = 0.
      ENDIF
      INTENS(I) = FLUXcm / BIG
      IF(I .GE. 90 .AND. I .LE. 120) WRITE(6,920) I-1, Y(I),
     * DATA, TIME, ANGcm, ENGYcm(I), FLUXcm, INTENS(I)
5000  CONTINUE
C
100   FORMAT(11A1)
110   FORMAT(F4.1)
120   FORMAT(F5.1)
130   FORMAT(F6.2)
140   FORMAT(F6.2)
150   FORMAT(F9.2)
160   FORMAT(2F6.2)
C
400   FORMAT(X, 'Enter today''s DATE in dd-mmm-yy format')
410   FORMAT(X, 'Enter channelwidth (DWELL) in microseconds in F4.1 form
     * at')
420   FORMAT(X, 'Enter ion drift time in microseconds in F5.1 format')
430   FORMAT(X, 'Enter flight PATH in cm using F6.2 format')
440   FORMAT(X, 'Enter lab angle (ANGlab) in degrees using F6.2 format')
450   FORMAT(X, 'Enter parent beam velocity in cm/s using F9.2 format')
460   FORMAT(X, 'Enter masses of fragments A and B in a.m.u. using 2F6.2
     * format')
C
700   FORMAT(X, 'Date: ',11A1)
710   FORMAT(X, 'The dwell time per MCS channel in TOF data is ',F4.1,
     *  ' microseconds')
720   FORMAT(X, 'The ion drift time is ', F5.1, ' microseconds.')
730   FORMAT(X, 'The product flight path is ', F6.2, ' cm. ')
740   FORMAT(X, 'The lab angle is ', F6.2, ' degrees.')
750   FORMAT(X, 'The parent beam velocity is ', E9.3, ' cm/s.')
760   FORMAT(X, 'The reduced mass of fragments is ', F6.2, ' a.m.u.')
770   FORMAT(X, 'The fragment c.m. velocity is ' , E9.3, ' cm/s.')
780   FORMAT(X, 'The peak is at channel number ', I5, '.')
790   FORMAT(X, 'The averaged counts for background subtraction is '
     *  , F9.0,  ' counts.')
800   FORMAT(X, 'The c.m. angle is >90 degrees after channel number'
```

```
     *  , I5, '.')
900     FORMAT(X, 'Channel', T10, 'Signal', T20, 'Data', T30
     *  , 'Flight Time', T45, 'c.m.Angle', T60, 'c.m.Energy'
     *  , T75, 'c.m.Flux', T90, 'Intensity')
910     FORMAT(X, 'Number', T10, '(counts)', T20, '(counts)', T30
     *  , '(usecs)', T45, '(degrees)', T60, '(Kcal/mol)'
     *  , T75, '(ct.cm.usec2)', T90, '(arb. unit)')
920     FORMAT(X, I5, T10, F7.0, T20, F7.0, T30, F9.2, T44, E13.6, T59
     *  ,E13.6, T74, E13.6, T89, E13.6)
C
C       This section is to use HGRAPH subroutine program to plot out
C       c.m. flux (Y-axis) as a function of c.m. energy (X-axis).
C       Subroutine INIPLT sets up maximum size of the plot (10.25" x 7.25")
        CALL CHOICE(IUNIT)
        CALL INIPLT(IUNIT,10.25,7.25)
        CALL SCALE(0., 62., 0., 1.2)
        CALL AXIS(10., .2, 'Center-of-mass Energy (Kcal/Mole)'
     *  , 33, 2, 0, 'Probability', 11, 2, 1)
        CALL DASHLN(ENGYcm, INTENS, 247, 1, 0, 0, 0, 0)
        CALL INILGN(5.5, 7.5, 4., 5.5)
        CALL WRILGN('CS2, 0 C ', 9, 0, 0, 0, 1)
        CALL WRILGN('Laser 193nm', 11, 0, 0, 0, 1)
        CALL ENDLGN
        CALL ENDPLT
        CLOSE(UNIT=22)
        STOP
        END
```

GENERAL SUMMARY

The energetics and dissociation dynamics of the $(C_2H_4)_2^+$, $(C_3H_6)_2^+$ and $(c\text{-}C_3H_6)_2^+$ complexes have been studied by photoionization of their corresponding neutral van der Waals clusters. The AE's for $C_3H_5^+$ and $C_4H_7^+$ from $(C_2H_4)_2$ measured in an ethylene beam, which mainly consists of C_2H_4 and $(C_2H_4)_2$, are 10.21±0.04 eV (1214±5 Å) and 10.05±0.04 eV (1234±5 Å), respectively. This suggests that the barriers for the reverse reactions of the ion-molecule reactions $C_2H_4^+ + C_2H_4$ are negligible. From the observed IE's of $(C_2H_4)_2$ (9.84±0.04 eV) and C_2H_4 (10.505±0.004 eV) and the estimated binding energy of $(C_2H_4)_2$ (0.02 eV), the bond dissociation energy for $C_2H_4^+ \cdot C_2H_4$ is calculated to be 15.8±1 kcal/mol.

The IE's of $(C_2H_4)_3$ and $(C_2H_4)_4$ are determined to be 9.465±0.036 eV (1310±5Å) and 9.287±0.034 eV (1335±5 Å), respectively. Using the known IE's of $(C_2H_4)_n$, n = 2, 3, and 4, and the estimated binding energies of $(C_2H_4)_2 \cdot C_2H_4$ and $(C_2H_4)_3 \cdot C_2H_4$, the bond dissociation energies for $(C_2H_4)_2^+ \cdot C_2H_4$ and $(C_2H_4)_3^+ \cdot C_2H_4$ are calculated to be 9.2±1 and 4.6±1 kcal/mol, respectively.

The measured IE of C_3H_6 is 9.738±0.003 eV and that of $c\text{-}C_3H_6$ is 9.721±0.011 eV. Using the ionization energies (IE) of $(C_3H_6)_2$ (9.33±0.04 eV) and $(c\text{-}C_3H_6)_2$ (9.61±0.04 eV) determined in this study, the calculation of the bond dissociation energies for $C_3H_6^+ \cdot C_3H_6$ and $c\text{-}C_3H_6^+ \cdot c\text{-}C_3H_6$ gives 0.43 and 0.14 eV, respectively.

By comparing the observed product channels in the unimolecular decompositions of $(C_2H_4)_3^+$, $(C_3H_6)_2^+$ and $(c\text{-}C_3H_6)_2^+$, one can conclude that the $(C_2H_4)_3^+$, $(C_3H_6)_2^+$, and $(c\text{-}C_3H_6)_2^+$ loose complexes rearrange to similar stable $C_6H_{12}^+$ ions prior to fragmenting.

In the laser photofragmentation study of CS_2 at 193nm, the TOF data of the CS fragments gives a result that the lower bound of the branching ratio of the two photodissociation channels, $S(^3P)/S(^1D)$, is 0.38. The new MB-LP-TOF machine can be readily modified to combine the TOF technique with other techniques such as laser-induced fluorescence, multiphoton ionization, and VUV photoionization for more advanced molecular photodissociation dynamics studies. This machine shows promises for outstanding molecular kinetics and dynamics research in Professor Ng's group at Iowa State University in the near future.

REFERENCES

1. Photophysics and Photochemistry above 6 eV, edited by F. Lahmani (Elsevier Science Publishing Company Inc., New York, 1985).

2. M. N. R. Ashfold, M. T. Macpherson and J. P. Simons, Top. Curr. Chem. 86, 1 (1979).

3. J. W. Taylor, "Synchrotron Radiation as a Light Source" in Chemical Spectroscopy and Photochemistry in the Vacuum-Ultraviolet, edited by C. Sandorfy, P. J. Ausloos and M. B. Robin (D. Reidel Publishing Company, Boston, MA, 1974).

4. J. A. R. Samson, Techniques of Vacuum Ultraviolet Spectroscopy (John Wiley & Sons, New York, 1967).

5. Molecular Beams and Low Density Gasdynamics, edited by P. P. Wegener (Marcel Dekker, Inc., New York, 1974).

6. G. V. Marr, Photoionization Processes in Gases (Academic Press, New York, 1967).

7. W. A. Chupka, "Ion-Molecule Reactions by Photoionization Techniques", in Ion-Molecule Reactions, edited by J. L. Franklin (Plenum Press, New York, 1972).

8. J. Berkowitz, Photoabsorption, Photoionization and Photoelectron Spectroscopy (Academic Press, New York, 1979).

9. W. Forst, Theory of Unimolecular Reactions (Academic Press, New York, 1973).

10. A. B. F. Duncan, Rydberg Series in Atoms and Molecules (Academic Press, NY, 1971).

11. Electron-Molecule Collisions and Photoionization Processes, edited by V. Mckoy, H. Suzuki, K. Takayanagi and S. Trajmar (Verlag Chemie International, Inc., Deerfield Beach, FL, 1983).

12. C. Y. Ng, Ph.D. Dissertation, University of California, Berkeley, CA, 1976).

13. Y. Ono, Ph.D. Dissertation, Iowa State University, Ames, IA, 1982.

14. S. H. Linn, Ph.D. Dissertation, Iowa State University, Ames, IA, 1982.

15. C. Y. Ng, Adv. Chem. Phys. 52, 263 (1983).

16. K. R. Wilson, "Photofragment Spectroscopy of Dissociative Excited States", in Excited State Chemistry, edited by J. N. Pitts (Gordon

and Breach, Science Publishers, New York, 1970).

17. S. J. Riley and K. R. Wilson, Faraday Discuss., Chem. Soc. 53, 132 (1972).

18. R. K. Sparks, K. Shobatake, L. R. Carlson and Y. T. Lee, J. Chem. Phys. 75, 3838 (1981).

19. H. Shinohara and N. Nishi, J. Chem. Phys. 77, 234 (1982).

20. H. Okabe, Photochemistry of Small Molecules (John Wiley & Sons, New York, 1978).

21. S. R. Leone, "Photofragment Dynamics", in Dynamics of the Excited State, edited by K. P. Lawley (John Wiley & Sons, New York, 1982).

22. G. G. Balint-Kurti and M. Shapiro, "Quantum Theory of Molecular Photodissociation", in Photodissociation and Photoionization, edited by K. P. Lawley (John Wiley & Sons, New York, 1985).